# Fault-tolerant multi-sensor fusion methods : collaborative localization and characterization of a multi-robot system

Nawal Alsaleh

UNIVERSITÉ DE LILLE

ÉCOLE DOCTORALE MADIS

UNITÉ DE RECHERCHE CRIStAL UMR 9189 – IEMN UMR 8520

THÈSE

par

**Nawal ALSALEH**

En vue de l'obtention du grade de docteur de l'Université de Lille
Spécialité : **« Automatique et informatique industrielle »**

---

# Méthodes de fusion multi-capteurs tolérantes aux défauts – Localisation et caractérisation collaboratives d'un système multi-robots

---

Thèse soutenue le **12/ 04/2024** devant le jury composé de :

| | | |
|---|---|---|
| Tan-Phu Vuong | Professeur à l'Université de Grenoble INP | *Rapporteur* |
| Bernard Kamsu Foguem | Professeur à l'Université de Toulouse INP | *Rapporteur* |
| Virginie Dégardin | Professeure à l'Université de Lille | *Examinatrice Présidente* |
| Serge Reboul | Professeur à l'Université du Littoral Côte d'Opale | *Examinateur* |
| Kamel Haddadi | Professeur à l'Université de Lille | *Directeur de thèse* |
| Denis Pomorski | Professeur à l'Université de Lille | *Directeur de thèse* |

UNIVERSITY OF LILLE

DOCTORAL SCHOOL MADIS

RESEARCH UNIT CRIStAL UMR 9189 - IEMN UMR 8520

THESIS

by

**Nawal ALSALEH**

To obtain the degree of Doctor of the University of Lille
Discipline: "**Automatic control and industrial informatics**"

---

# Fault-tolerant multi-sensors fusion methods - Collaborative localization and characterization of a multi-robots system

---

Defended on **12/04/2024** to a jury composed of:

| | | |
|---|---|---|
| Tan-Phu Vuong | Professor at university of Grenoble INP | *Reviewer* |
| Bernard Kamsu Foguem | Professor at university of Toulouse INP | *Reviewer* |
| Virginie Dégardin | Professor at university of Lille | *Examiner President* |
| Serge Reboul | Professor at university of Littoral Côte d'Opale | *Examiner* |
| Kamel Haddadi | Professor at university of Lille | *Thesis director* |
| Denis Pomorski | Professor at university of Lille | *Thesis director* |

*This work was supported by the University of Lille and the Hauts-de-France Region. It is the result of collaboration between the two laboratories:*

## CRIStAL

**C**entre de **R**echerche en **I**nformatique, **S**ignal et **A**utomatique de **L**ille

UMR CNRS 9189


## IEMN

**I**nstitut d'**E**lectronique, de **M**icroélectronique et de **N**anotechnologie

UMR CNRS 8520

*« God elevates those among you who believe, and those given knowledge, many steps. And God is Aware of what you do »*

---

*Quran: Surat Al-Mujadilah, Ayah 11.*

*To the children of Gaza*

*To the children of Sudan*

*To all the children who deserve to live a better life but are prevented by the actions of bad people*

*I dedicate this thesis*

# Acknowledgment

First of all, I would like to thank my thesis supervisors, Kamel Haddadi, Professor at the University of Lille, and Denis Pomorski, Professor at the University of Lille, for their time, kindness, support, and invaluable advice throughout this research project.

I would also like to express my appreciation to Mr. Tan-Phu Vuong and Mr. Bernard Kamsu Foguem for the honor of reviewing my work. I would also like to thank Mr. Serge Reboul and Mrs. Virginie Dégardin for agreeing to serve as examiners for this thesis. The final version of this thesis benefited from their careful reading and valuable comments.

My gratitude extends to all the members of the CRIStAL and IEMN laboratories. The collaboration between these two laboratories provided me with the opportunity to work with two research teams, which proved to be an enriching experience.

I would also like to thank my teachers at the Lebanese University for all the knowledge they have passed on to me throughout the process. This work is the fruit of their efforts.

I would also like to thank my friends and colleagues who have given me their moral and intellectual support during these three unforgettable years, in particular, Israa, Ghina, Rajaa, Hanane, Mohamed, Rim, Mehdi, Mohan, Lydia, Cerine, Fatima, and Clement.

My sincere thanks go to my family: my dearest parents, Mohamad and Hanane, who have always been there for me, sacrificing everything, sparing neither health nor effort. I would also like to thank my brothers Mostafa, Abdalla, Abdelkarim, Abdelhay for their unconditional support and encouragement.

Finally, I would like to express my heartfelt thanks to my dear husband, **Bilal Daass**. We have shared together the best moments and stood by me through the most challenging times of my life. Without your endless support, I could not have completed this thesis or become who I am today. No words can fully express my gratitude, and love for you. May Allah keep our little angel, **Lyne**, who inspired many sleepless nights spent writing this report.

# Résumé

Cette thèse vise à développer des méthodologies dédiées à améliorer la fonctionnalité de robots mobiles pour accomplir une mission, en particulier la caractérisation électromagnétique micro-onde de matériaux dans leur environnement. Le succès de cette mission dépend de la navigation précise et de la perception exacte de l'environnement par les robots, un challenge qui est souvent perturbé par les défaillances et les incertitudes des capteurs. À cet égard, la thèse se concentre principalement sur deux points fondamentaux. Dans le premier, nous développons une méthode de localisation robuste pour assurer une navigation autonome précise et tolérante aux défauts pour les robots mobiles. Cette méthode repose sur une approche statistique informationnelle, incorporant un seuil adaptatif qui facilite la détection rapide et précise des défauts de capteurs. L'efficacité de cette méthode est validée par une étude comparative avec des approches existantes de la littérature.

Le deuxième point consiste à développer des techniques de contrôle et d'évaluation non destructives par micro-ondes (Microwave Non Destructive Testing & Evaluation - MNDT&E) pour la caractérisation des matériaux. Initialement, nous considérons des techniques conventionnelles de MNDT&E, associées à une modélisation analytique. Reconnaissant les limites de la modélisation analytique, nous présentons trois nouvelles techniques « intelligentes » de MNDT&E qui intègrent des modèles d'apprentissage automatique (Machine Learning - ML) et d'apprentissage profond (Deep Learning - DL). Ces techniques reposent sur deux approches micro-ondes : la propagation en espace libre pour la caractérisation sans contact en utilisant un radar mono-statique et la propagation guidée pour la caractérisation en contact en utilisant un guide d'ondes rectangulaire (Open-Ended Rectangular Waveguide - OERW). Les capteurs développés intègrent des contraintes de faible encombrement et faible coût, compatibles avec un contexte hors laboratoire. Dans une première phase, les techniques proposées sont utilisées pour mesurer les coefficients de réflexion $S_{11}$ des matériaux, générant trois bases de données distinctes. La deuxième phase consiste à utiliser les modèles ML et DL afin de relier les réponses électromagnétiques mesurées et les types de matériaux identifiés ou la présence de défauts. De plus, différentes configurations et topologies de mesure sont introduites et mises en œuvre. La performance de chaque configuration est évaluée et analysée en fonction de métriques sélectionnées dans des conditions de laboratoire et des conditions réalistes.

Enfin, nous présentons une étude de faisabilité basée sur un réflectomètre six ports à guide d'ondes métallique. Ce dispositif présente des avantages particulièrement bien adaptés à des contingences hors laboratoire tels que sa consommation électrique réduite, sa précision de mesure électrique et sa capacité à opérer en environnement difficile. De plus, le système développé pour un fonctionnement en bande de fréquences V (55-75 GHz) facilite le passage de la caractérisation des micro-ondes à celle des ondes millimétriques, jetant les bases d'une analyse précise et efficace. La montée en fréquences élargit le spectre des informations capturées, améliorant les capacités, la précision et la versatilité des techniques de contrôle et d'évaluation non destructifs.

**Mots clés : filtre de Kalman, tolérance aux défauts, théorie de l'information, localisation, average run length, contrôle non-destructif, micro-ondes, analyseur de réseau**

**vectoriel, permittivité, caractérisation de matériaux, détection de défauts, apprentissage automatique, apprentissage profond, six-port.**

# Abstract

This thesis aims to develop methodologies dedicated to improve the functionality of mobile robots to accomplish a mission, in particular the microwave electromagnetic characterization of materials in their environment. The success of this mission depends on precise navigation and accurate perception of the environment by the robots, a challenge that is often affected by sensor failures and uncertainties. In this regard, the thesis primarily focuses on two fundamental points. In the first, we develop a robust localization method to ensure precise and fault-tolerant autonomous navigation for mobile robots. This method relies on an informational statistical approach, incorporating an adaptive threshold that facilitates fast and accurate detection of sensor faults. The effectiveness of this method is validated through a comparative study against existing approaches from the literature.

The second point is to develop nondestructive testing and evaluation techniques using microwaves (microwave Non Destructive Testing & Evaluation MNDT&E) for material characterization. Initially, we consider conventional MNDT&E techniques, coupled with an analytical modeling. Recognizing the limitations of analytical modeling, we present three novel « intelligent » MNDT&E techniques that integrate machine learning (ML) and deep learning (DL) models. These techniques are based on two microwave approaches: free-space propagation for non-contact characterization using a monostatic radar and guided propagation for contact characterization using an open-ended rectangular waveguide (OERW). The sensors developed integrate the constraints of compactness and low cost, compatible with a non-laboratory context. In a first phase, the proposed techniques are employed to measure the reflection coefficients of materials $S_{11}$, generating three distinct databases. The second phase involves using ML and DL models to relate the measured electromagnetic responses and the identified material types or the presence of damage. Additionally, various measurement setups and topologies are introduced and implemented alongside the proposed methods. The performance of each setup combination is assessed and analyzed based on selected metrics under both laboratory and realistic conditions.

Finally, we present a feasibility study based on a metallic waveguide six-port reflectometer. This device offers advantages particularly well suited to non-laboratory requirements, such as low power consumption, electrical measurement accuracy and the ability to operate in harsh environments. Furthermore, the system developed for operation in V-band frequencies (55-75 GHz) facilitates a shift from microwave to millimeter-wave characterization, establishing a foundation for accurate and efficient analysis. Increasing frequencies expand the spectrum of information captured, enhancing the capabilities, accuracies, and versatility of nondestructive testing and evaluation techniques.

**Keywords: Kalman filter, fault tolerance, information theory, localization, average run length, non-destructive evaluation, microwaves, vector network analyzer, permittivity, material characterization, defects detection, machine learning, deep learning, six-port.**

# Contents

# List of figures

# List of tables

# List of abbreviations

ARL: **A**verage **R**un **L**ength

SPC: **S**tatistical **P**rocess **C**ontrol

CUSUM: **CU**mulative **SUM**

EWMA: **E**xponentially **W**eighted **M**oving **A**verage

KF: **K**alman **F**ilter

MNDT&E: **M**icrowave **N**on-**D**estructive **T**esting and **E**valuation

ML: **M**achine **L**earning

DL: **D**eep **L**earning

IFBW: **I**ntermediate **F**requency **B**and**W**idth

MUT: **M**aterial **U**nder **T**est

OERW: **O**pen-Ended **R**ectangular **W**aveguide

VNA: **V**ector **N**etwork **A**nalyzer

SVM: **S**upport **V**ector **M**achine

DCT: **D**ecision **T**ree

RF: **R**andom **F**orest

CNN: **O**ne **D**imensional **C**onvolutional **N**eural **N**etwork

1D-CNN: **O**ne **D**imensional **C**onvolutional **N**eural **N**etwork

# Chapter 1. General context

## Chapter outlines

# 1. 1 Introduction

Mobile robots have emerged as an innovative technology, providing solutions in environments where human intervention proves challenging or dangerous. Their autonomous navigation capabilities have transformed various applications, leading to a significant enhancement in efficiency across diverse domains. In this research work, a primary focus involves achieving significant advances through the integration of microwave techniques on mobile robots. The mission of these techniques is to characterize materials within the surrounding environments of the robots. In particular, microwave characterization techniques and tools have been widely described in the literature to address nondestructive testing applications in a variety of fields. They present advantages such as contactless operation, non-ionizing sensing, and penetration into dielectric materials. Consequently, our objective is to equip mobile robots with free-space sensing radars to address ultimately scanning / imaging of large areas. Indeed, radar techniques are mostly thought as single measurement method with poor scanning capabilities. This integration aims to provide scanning capabilities while minimizing the requirement for extensive human intervention, consequently reducing the exposure of humans to potential dangers in diverse working environments.

This research represents a continuation of a prior thesis conducted in collaboration between the CRIStAL and IEMN laboratories. In the earlier study, a proof-of-concept method for nondestructive testing and evaluation of materials in the immediate proximity of robot environments was developed. Specifically, microwave instruments were integrated into a multi-robot system to characterize materials under test, as illustrated in figure 1.1. Adapting this approach to collaborative mobile robots posed a significant challenge, particularly in harsh environments. The earlier study placed considerable focus on the localization of robots, as well as communication and collaboration within the multi-robot system.

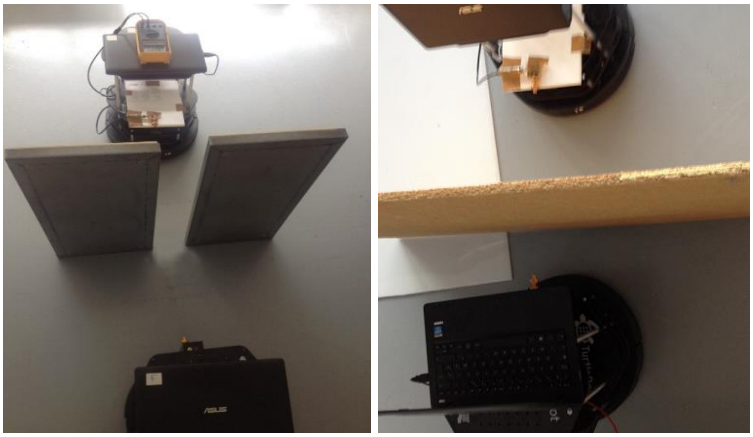

Figure 1.1 Microwave on-destructive testing platform.

In this thesis, we work on two pivotal aspects critical for the successful implementation of the MNDT&E techniques on a mobile robot. The first aspect is focused on the development of a robust localization approach, acknowledging that precise localization is tolerant to the defects of sensors embedded on a system. A robot is equipped with several sensors to determine its precise

position (i.e. its location and orientation). In such a system, a large amount of data is transmitted simultaneously. At any given time, each sensor may fail and/or lose its performance, resulting in loss of information or erroneous data. To achieve real-time, accurate, and robust localization, the research introduces multi-sensors data fusion approach using the extended Kalman filter. Simultaneously, a complementary diagnostic approach based on the **Entropy criterion** is presented to efficiently identify and isolate malfunctioning sensors. This dual-approach enhances system efficiency by accurately detecting sensor anomalies, allowing for effective navigation. The effectiveness of this approach is evaluated and compared with other methods in the literature using the key performance metric, average run length (ARL). This metric provides insights into the delay in defect detection and estimates the false alarm detection. Consequently, this solution establishes an automated system that ensures accurate navigation during manufacturing or service operations.

The second aspect of this thesis involves the development of MNDT&E techniques for planar material characterization. NDT&E for material characterization is a concept and set of techniques used to inspect, analyze, and assess the properties and quality of materials without causing any damage to the material being examined. In particular, a key aspect of this process involves studying and evaluating the types of materials and determining the presence of defects within them.

First, we introduce conventional MNDT&E techniques along with an appropriate analytical modeling and calibration technique to characterize planar dielectric materials. However, it remains challenging to characterize the materials using analytical modelling. The unknown material thickness and the position, shape, and size of defects have an impact on the measured reflected electromagnetic wave which make this task challenging. Moreover, random noise can significantly influence the properties of the signals, which highly affects the detecting and characterizing sensitivity. In this regard, we develop three intelligent MNDT&E techniques for planar material characterization and surface/subsurface defects detection. This strategy involves integrating microwave techniques with ML and DL models to analyze the microwave response. Introducing these methods create the opportunity to address a wide range of scenarios and to adapt precision levels according to distinct application needs. Moreover, this advancement presents advantages such as reducing the dependency on the operators skills and experience, reducing the dependency on complex conversion methods, and potentially enhancing the sensitivity of material characterization and defects detection [1-2].

The first ‘intelligent’ MNDT&E technique is developed by using a free-space propagation through a monostatic radar, with the reflection waves analyzed through five ML models including decision tree, random forest and support vector machine with three different kernels. In contrast, the second technique is based on guided propagation through an OERW in contact with the planar material under test. The reflected waves are analyzed through the same five ML models for material characterization. The third technique is based on using the OERW, with a 1D-convolutional neural network (CNN) algorithm to perform the analysis of the measured reflection coefficients and detect defects within the materials.

Furthermore, in the field on NDT&E, a feasibility study has been conducted using a six-port reflectometer operating in millimeter wave range, around 60 GHz. The aim of this study is to increase the frequency of operation, with the goal of enhancing the accuracy and the sensitivity of

material characterization, while maintaining relatively low-cost. Additionally, the adoption of the six-port system contributes to increase immunity to surrounding noise, further improving the reliability of the testing and evaluation process.

## 1. 2 Thesis contributions

This research presents original contributions in several significant areas. The thesis objectives are centered around two main parts. The first objective is to propose a novel method for ensuring accurate robot localization, even in the presence of sensor faults. The second objective is to introduce three innovative intelligent MNDT&E techniques, combined with ML and DL models, to develop new, fully functional material characterization and defects detection techniques. Based on these objectives, the major contributions of this work can be described as follows:

- Proposing a multi-sensors fault tolerant fusion approach for accurate robot localization. Based on adaptive Entropy-based threshold control chart (AET-Control chart), this approach monitors the mean of a residual that follows a normal distribution. A performance comparison study in terms of Average Run Length (ARL), with five other methods in the literature is presented.
- Implementing a monostatic free space measurement setup, with a horn antenna operating as a radar pointing toward a MUT at a certain distance away from the antenna.
- Implementing an OERW to provide accurate and reliable measurements, enabling the identification and characterization of defects within the MUT with high accuracy and resolution.
- Ensuring measurement precision through specific techniques, which in turn enhance the reliability of the measurements.
- In free-space measurement setup, collecting a database comprising the magnitude and phase-shift of the reflection coefficient $S_{11}$for different types of materials with different thicknesses, providing a diverse range of samples for analysis and classification.
- Employing classification methods based on ML algorithms. Five algorithms are used and compared: random forest (RF), decision tree (DCT) and support vector machine (SVM) with three kernels. The performance of these classifiers is evaluated using different evaluation metrics: accuracy, precision, sensitivity and F1_score.
- Evaluating the classifier accuracy for different stand-off distances, providing insights into their performance in varying scenarios.
- Using the OERW, collecting two databases comprising the magnitude and phase shift of $S_{11}$ for: (1) different types of materials, (2) different configurations of defects in several materials. We apply the same set of five machine learning models to classify materials using the data from database (1). Furthermore, a convolutional neural network model is implemented for the purpose of detecting defects based on the information from database (2). The performance of these models is evaluated using different evaluation metrics: accuracy, precision, sensitivity and F1_score.

## 1. 3 Thesis outlines

In summary, the thesis introduces a robust localization method for mobile robots. It then presents conventional MNDT&E techniques along with an analytical calibration method for material characterization. Subsequent sections cover the generation of three databases, derived from microwave measurements on various materials, and present the results of applying ML and DL models to these databases. The thesis concludes by presenting a six-port based feasibility study aimed at enhancing material characterization.

This first chapter is focused on the motivations, objectives and contributions of this thesis, the remainder of this thesis is organized as follows:

Chapter 2 focuses to establish an advanced localization approach that maintains a robust tolerance to sensor faults. To achieve this goal, a combination of positioning sensors is integrated on the robot, and a strategy for data fusion is then developed. Additionally, a technique based on the concept of the entropy criterion is introduced to effectively identify and isolate malfunctioning sensors. This approach allows the system to navigate with efficiency, effectively identifying sensor anomalies in a precise manner. This leads to the establishment of a high degree of accuracy and robustness. This method is applied to a real-life application and subsequently compared with existing literature, based on the key metric ARL.

Chapter 3 provides an overview of the theoretical foundations of wave/material interactions, microwave characterization techniques and associated measurement instrumentations. Following the theoretical overview, the chapter details the design and implementation of conventional microwave techniques used for material characterization. In initial setup, a corrugated horn associated to a Vector Network Analyzer (VNA) measure the reflection coefficient $S_{11}$of the material under test (MUT). Following the measurements, a calibration method is employed to extract the material permittivity, allowing for the identification of its type. In the second setup, the corrugated antenna is substituted with a more compact horn antenna, and the same steps are repeated. To validate the efficiency of these methodologies, practical experiments are conducted using two wooden MUT samples. Subsequently, the findings are compared with results documented in the literature. The chapter concludes by highlighting the advantages and limitations associated with these techniques.

Chapter 4 outlines the integration of MNDT&E techniques with ML and DL models for material characterization. The first part covers the basics of the ML and DL models used in this thesis. Following that, a literature review is presented, highlighting various microwave techniques and their integration with ML and DL models, along with a comparative analysis of these methods. In the second part, the design and implementation of three intelligent MNDT&E techniques for material characterization are presented. The first technique is based on using a monostatic free space radar designed for material characterization. The configuration consists of a horn antenna combined with a VNA to measure both the magnitude and phase of $S_{11}$, primarily for materials with three distinct types: wood, Plexiglas, and glass. The measured data are then analyzed and classified using five distinct ML algorithms: DCT, RF, SVM with three kernels. The measurements are conducted at various distances, aiming to verify effectiveness across different ranges The second technique is based on using an OERW with a VNA to measure the

$S_{11}$ for the same group of materials, for contact material characterization. The measured data are then analyzed and classified using the same five ML algorithms. A comprehensive performance analysis is conducted for these two techniques under two distinct environmental conditions: laboratory settings and more realistic settings. The third technique incorporates the use of an OERW with a one dimensional convolutional neural network (1D-CNN) model for defect detection within materials. The measured data are a set of various types and sizes of intentionally generated material defects. Finally, a comparative study between free space and contact characterization is proposed.

Chapter 5 discusses a feasibility study centered around a six-port reflectometer operating within the millimeter frequency range (i.e. around 60 GHz). The chapter presents the application of the six-port reflectometer in two scenarios: sub-millimeter distance measurements and IQ demodulation. This approach is highlighted for its potential to offer enhanced accuracy for material characterization.

## 1. 4 Scientific production

### International conferences:

1. N. Alsaleh, B. Daass, D. Pomorski and K. Haddadi, "Fast and Real-Time Sensor-Fault Detection using Shannon's Entropy," *2021 5th International Conference on Control and Fault-Tolerant Systems (SysTol)*, Saint-Raphael, France, pp. 273-278, 2021.
2. N. Alsaleh, D. Pomorski, M. Sebbache, C. Lenoir and K. Haddadi, "Nano-Positioning Test platform for Free-Space Six-Port Interferometric Distance Measurements," *2021 IEEE Conference on Antenna Measurements & Applications (CAMA)*, Antibes Juan-les-Pins, France, pp. 562-564, 2021.
3. N. Alsaleh, D. Pomorski, M. Sebbache, C. Lenoir and K. Haddadi, "WR15 Six-Port Interferometric Set-up for Millimeter-Wave Characterization for Harsh Environments," *2022 Photonics & Electromagnetics Research Symposium (PIERS)*, Hangzhou, China, pp. 414-419, 2022.
4. N. Alsaleh, D. Pomorski, M. Sebbache and K. Haddadi, "Machine Learning-Based Monostatic Microwave Radar for Building Material Classification," *2023 IEEE International Instrumentation and Measurement Technology Conference (I2MTC)*, Kuala Lumpur, Malaysia, pp. 1-5, 2023.

### Journals:

1. N. Alsaleh, B. Daass, D. Pomorski and K. Haddadi. "A New Control Charts with Adaptive Entropy-Based Threshold – Average Run Length (ARL) Performance Evaluation".
2. N. Alsaleh, D. Pomorski, M. Sebbache and K. Haddadi. "Machine Learning-Based Microwave Material Characterization".

# Chapter 2. Robust multi-sensors fusion for precise localization of mobile robots

## Chapter outlines

## 2.1. Introduction

In mobile robot systems, localization is a fundamental task that has been of increasing interest in recent years given its importance in a wide range of applications, such as surveillance [3], environment perception, trajectory planning and control [4-5]. Localization techniques can be divided into two categories [6-7]: relative localization, relying on internal sensors like encoders, accelerometers, and gyrometers; and absolute localization, utilizing external sensors whose measurements determine the robot's position in a reference frame linked to the environment, such as GNSS receivers, laser rangefinders, and cameras.

Numerous solutions are proposed in the literature which differ in terms of the types of used sensors and technologies, and localization algorithms. However, a number of challenges are considered, for example:

- Sensors exhibit limitations based on the employed technology, resulting in measurements that may be prone to noise.
- Sensors are vulnerable to external disturbances across different scenarios, especially in challenging environments. These difficulties encompass exposure to strong magnetic fields, variations in land humidity leading to drift (affecting wheel encoders), multipath interference, and tunnel conditions (affecting GNSS receivers), along with other potential sources of disruption or security threats.
- Internal defects in sensors may manifest as mechanical issues or algorithmic bugs.
- Robot modeling errors: difference in wheel diameter compared to its nominal value, different left/right wheel diameters, approximate resolution of a wheel encoder, etc.

For accurate robot localization, multi-sensors data fusion techniques [8-10] have experienced significant growth in robotic fields. These techniques involve combining data from multiple potentially noisy sensors to obtain an estimation of unknown state variables, such as position in the field of robotics. These methods allow for a more accurate estimation of this position than using a single sensor alone [11-12] . The challenge lies in managing the imperfections of the integrated sensors by using redundancy and/or complementarity of information. The commonly used approach is to implement a probabilistic sequential filter such as the Kalman filter [13], information filter [14], particle filter [15], or others. The choice of a filter among others is crucial, especially for a mobile robot system with numerous sensors and when real-time estimation is required.

Given the potential disturbances and defects mentioned earlier, the necessity for a more robust robot localization becomes evident. Sensor diagnostic step is mandatory to detect and locate sensors failures as quickly as possible. A failure in any sensor can limit performance and lead to lower localization performance. In this context, the development of statistical methods is capable of detecting and locating these failures as quickly as possible. By statistically formulating the phenomenon, when a system operates in normal mode (or abnormal mode), its variables are characterized by probability distributions corresponding to faultless (or faulty) operation. In general, methods for detecting changes in signals require the use of control charts, implementing an online-tested statistic. Among the most commonly used control charts: CUSUM (Cumulative sum) and EWMA (Exponentially Weighted Moving Average) control charts [16]. These methods

involve comparing a generalized likelihood ratio to a commonly fixed threshold, the value of which determines the performance of the detection system. In this work, we present an entropy-based criterion to enhance the performance of these methods by calculating a more appropriate adaptive threshold. Consequently, our approach involves a fault-tolerant multi-sensors data fusion.

In this chapter, we present a fault-tolerant multi-sensors fusion in order to ensure accurate and robust localization of the mobile robot. A previous thesis study primarily focused on the development of the robot platform, with a particular focus on fault-tolerant localization [17]. The contribution of our research lies in the performance evaluation study, which is compared with existing literature, using the Average Run Length (ARL) as a key metric.

The remainder of this chapter is structured as follows: the first section introduces the employed robot platform. The next section focuses on presenting the proposed fault-tolerant multi-sensors fusion approach, along with the corresponding experimental results. In the subsequent section, we conduct a performance comparative study, based on the ARL metric. We end this chapter with a conclusion.

## 2.2. Robotic platform description

The platform used in this work is based on the second version of the TurtleBot™ mobile robot. This robot was initially designed in 2010 and released for sale in 2011 as a minimalist platform for educational purposes and mobile robotics prototyping. In 2012, the second version, known as TurtleBot 2, was developed by the Korean company 'Yujin Robot', based on the research robot 'iClebo Kobuki' (figure 2.1). It consists of a small mobile base called 'Kobuki', equipped with an internal battery, power controllers, and charging contacts. At the top of this base, there is a stack of trays allowing the placement of a laptop computer (a notebook or an electronic board), providing ample open space for prototyping.

The TurtleBot 2 is of the unicycle type, meaning it is powered by two independently controlled drive wheels and has a free wheel for stability. Its center of rotation is located on the axis connecting the two drive wheels. In 2017, a new version (TurtleBot 3) with additional features was developed. Nonetheless, our decision to utilize the second version (TurtleBot 2) was driven by the limitations of TurtleBot 3, which, due to its extremely compact design, lacked the capability to accommodate the onboard sensors and antenna essential for our experiments.

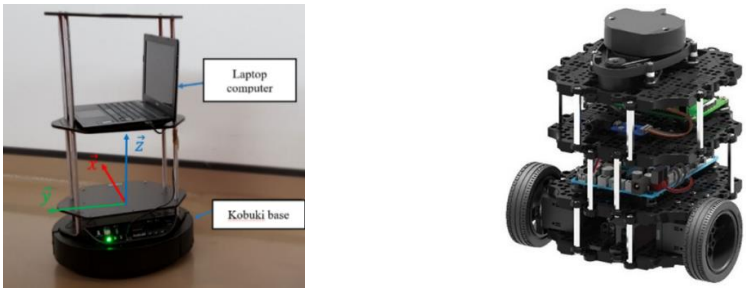


(a) (b)

Figure 2.1 Robot TurtleBot – (a) version 2; (b) version 3.

For the localization purpose, various positioning sensors are installed on the robot, we provide a brief description of these sensors in the following. The Kobuki base is equipped with the following proprioceptive sensors:

1. **Encoder on each wheel**

   It provides the basic wheel rotation information and calculates the distance traveled. These encoders are characterized by 11.7 ticks per millimeter. A calculation can be performed to estimate the robot's position and orientation relative to its starting point. The data is provided at a frequency of 50 Hz.

2. **Electronic gyroscope (3 axes factory-calibrated)**

   It allows for determining the robot's orientation. The data is provided at a frequency of 100 Hz.

In order to enhance the pose estimation, measurements from proprioceptive sensors (i.e., encoders, gyroscope) can be fused with data from exteroceptive sensors onboard the robot. For this purpose, we have chosen to use a 2D LIDAR and an indoor navigation system:

3. **2D LIDAR (RPLIDAR$^{TM}$)**

   In this work, a 2D LIDAR of the RPLIDAR type is used (figure 2.2). It is a low-cost laser scanner that performs a 2D, 360-degree scan using a rotating head, with a maximum range of 6 meters. The rotation speed of this LIDAR ranges from 5.5 to 10 Hz, with a sampling frequency of 2000 Hz.

Figure 2.2 2D LIDAR - RPLIDAR.

The LIDAR provides the position of the robot on which it is mounted by matching two consecutive laser scan measurements. The estimation of its pose is performed using a point cloud alignment technique based on the Iterative Closest Point (ICP) algorithm [18]. This algorithm compares the two consecutive point clouds at each moment and yields translation and rotation matrices as results. These two matrices are then used by the kinematic model of the differential mobile robot to deduce the new robot pose measurement.
This technique is robust, even though it accumulates errors as the robot moves [19]. However, it is worth noting that this technique yields less reliable results when nearby elements are moving within the LIDAR's field of view. During our experiments, the

immediate environment of the robot is assumed to contain a small number of dynamic elements.

**4. Indoor Navigation System: Marvelmind™ System**

The Marvelmind Indoor Navigation System, also known as 'indoor GPS' (figure 2.3), provides location data with an accuracy of ±2 cm. This system consists of three essential components communicating through a radio interface. The main features of these elements are summarized below:

- Fixed beacons: Fixed to walls or ceilings, with a distance between neighboring beacons of less than 30 meters.
- Mobile beacons: Installed on the robot and interact with it via one of the onboard computer's USB ports. These beacons incorporate an Inertial Measurement Unit (IMU) and they are similar to fixed beacons.
- Modem: Serving as the central controller of the system, the modem allows access to measurements from the central workstation and can support up to 250 beacons.

The position of a mobile beacon installed on a robot is determined through triangulation based on the time delay of an ultrasonic signal sent to all fixed ultrasonic beacons.

Figure 2.3 Modem and Beacons of the Marvelmind Indoor Navigation System.

For 3D positioning, an unobstructed line of sight between the mobile beacon and three or more fixed beacons must be ensured. The data frequency provided by this navigation system is 45 Hz.

In the following section, we introduce a sensor fault-tolerant fusion approach designed to enhance the accuracy of robot localization using the specified platform.

## 2.3. Towards a fault tolerant fusion system: A more robust robot localization

### 2.3.1. Introduction

Achieving precise localization is a fundamental requirement for an effective and successful navigation of the robot. Localization refers to the robot's ability to determine its exact position

within its environment. Relying only on a single sensor can be risky, as each sensor has its limitations, such as susceptibility to environmental factors or inaccuracies due to noise. To enhance localization accuracy, it is common practice to employ a combination of complementary sensors and employ data fusion techniques.

Over the past two decades, multi-sensors data fusion techniques have experienced significant growth in various fields [8]-[10]. These techniques involve combining data from multiple potentially noisy sensors to obtain estimates of unknown state variables, such as position, velocity, and attitude, particularly in the field of robotics. These methods enable a more precise estimation of these states compared to relying on a single sensor. The challenge lies in managing imperfections in the integrated resources by leveraging redundancy and/or complementarity of information. The commonly employed approach is to implement probabilistic sequential filters such as the Kalman filter, the information filter, the particle filter, or others. In this study, we opt for the extended Kalman filter, renowned for its extensive application in the field of robotics, to address this particular challenge. In addition, we plan in this work to enhance our research by incorporating a diagnostic aspect into the extended Kalman filter. This addition will enable potential sensor malfunctions to be detected and dealt with, further enhancing the robustness and reliability of our robotic system.

The reminder of this section is organized as follows. In the sub-section 2.3.2, we provide an overview of the extended Kalman filter's use in sensor fusion. Following that, we detail the fault detection strategy, starting with the introduction of the residual generation in the sub-section 2.3.3 and then delving into a state-of-the-art discussion on Statistical Process Control (SPC) in the sub-section 2.3.4. Subsequently, we present in the sub-section 2.3.5 a proposed criterion aimed at enhancing sensor fault detection performance. We end this section with the presentation of experimental results and a summarizing conclusion.

### 2.3.2. Precise robot localization: Extended Kalman filter

In order to effectively control a dynamic system, an accurate estimation of its state must be provided. The following discrete state-space equations are conventionally used:

$$X_k = F_k X_{k-1} + \alpha_k \tag{2.1}$$

$$Z_k = H_k X_k + v_k \tag{2.2}$$

where:

- $k$ represents the discrete time index.
- $X$ represents the state of the system.
- $Z$ represents the observation vector of the system.
- $F$ represents the transition matrix.
- $H$ represents the measurement matrix.
- $\alpha$ is the process noise due to disturbances and modeling errors.
- $v$ is the measurement noise.

Both $\alpha$ and $v$are Gaussian white noises with zero mean and covariance $Q$and $R$, respectively.

The covariance of the two noise models is given by:

$$Q_k = E[\alpha_k(\alpha_k)^T] \quad (2.3)$$

$$R_k = E[v_k(v_k)^T] \quad (2.4)$$

Where $E$ denotes the mathematical expectation.

**Extended Kalman filter**

In the context of multi-sensors fusion, the Kalman filter is among the most widely used due to its optimality, tractability, recursivity, and robustness. Its role is to estimate the state of a system from a series of incomplete or noisy measurements. Initially designed for linear systems, it has been extended to handle nonlinear systems.

The main problem in filtering is to achieve optimal estimation $X_{k/k}$ of the state vector at time $k$, given the observations $Z_k$ up to time $k$. The Kalman filter operates in two distinct steps: prediction and update. The prediction step is based on the evolution model, which uses the estimated state at the previous time to produce an estimate of the current state. Complementarily, the update step is based on the observation vector to correct the predicted state and obtain a more precise estimate of the state vector.

However, due to the nonlinear nature of the evolution model, the Kalman filter cannot be applied directly. One solution is to use an extended version. This solution, widely used in scientific literature, is well-suited to our context of mobile robot navigation [20]. Due to this linearization, the extended Kalman filter is suboptimal. Below we present the equations for each step.

**a. The prediction step**

A comprehensive modeling that accurately describes the behavior of wheeled mobile robot is a challenging task. Consequently, the following assumptions are formulated:

- The mobile robot is assumed to be a rigid block without any suspension.
- The wheels are considered non-deformable, and slip and aerodynamic forces are neglected.
- The surface is assumed to be horizontal, hard, homogeneous, and perfectly flat.
- The contact between the wheels and the ground is considered to be point-like.
- The travel velocities are assumed to be very low.

Based on these assumptions, a model for the motion of the robot can be developed. We have chosen to use an odometric model based on measurements obtained from the robot's wheel encoders.

At each instant $k$, the state vector is defined as the pose (i.e., position and orientation) of the robot in a fixed global coordinate frame.

$$X_k = [x \quad y \quad \theta]^T \quad (2.5)$$

Where $x \wedge y$represent the position of the robot, and$\theta$ represents its orientation.

The odometric evolution model describes the evolution of its state between instants $(k-1)$ and $k$ as follows:

$$X_k = X_{k/k-1} + A_k U_k + \alpha_k \tag{2.6}$$

Where:

- $U_k = [\Delta_k \quad \omega_k]^T$ is the input vector, with:
  - $\Delta_k$ and $\omega_k$ representing respectively the elementary translation and rotation of the robot, obtained from measurements of their right and left wheel encoders at instant $k$.

$$\Delta_k = \left[\frac{r_r \Delta_{qr} + r_l \Delta_{ql}}{2}\right]_k \tag{2.7}$$

$$\omega_k = \left[\frac{r_r \Delta_{qr} - r_l \Delta_{ql}}{2e}\right]_k \tag{2.8}$$

  - $\Delta_{qr}$ and $\Delta_{ql}$ correspond to the elementary rotations of the right and left wheels between instants $(k-1)$ and $k$.
  - $2e$ represents the width of the robot.
  - $r_r$ and $r_l$correspond to the radii of the right and left wheels, respectively.
  - $A_k = \begin{pmatrix} cos\left(\theta_{k-1} + \frac{\omega_k}{2}\right) & 0 \\ sin\left(\theta_{k-1} + \frac{\omega_k}{2}\right) & 0 \\ 0 & 1 \end{pmatrix}$

- $\alpha_k$represents the noise associated with the state model, considered as white Gaussian noise with zero mean and a covariance matrix $Q_k$.

Based on this, the prediction equations can be written as follows:

$$X_{k/k-1} = X_{k-1} + A_k U_k = f(X_{k-1}, U_k) \tag{2.9}$$

$$P_{k/k-1} = F_k P_{k-1/k-1} (F_k)^T + G_k (Q_u)_k (G_k)^T + Q_k \tag{2.10}$$

Where:

- $P_{k/k-1}$ is the predicted (i.e., prior) covariance matrix. It measures the predicted accuracy of the predicted state $X_{k/k-1}$.
- $F_k = \frac{\partial f}{\partial X}|_{X_{k-1/k-1}}$ and $G_k = \frac{\partial f}{\partial X}|_{U_k}$ are Jacobian matrices calculated by propagating the state covariance while taking into account the covariance of the elementary translation and rotation of the robot:

$$F_k = \begin{pmatrix} 1 & 0 & -\Delta_k sin\left(\theta_{k-1} + \frac{\omega_k}{2}\right) \\ 0 & 1 & \Delta_k cos\left(\theta_{k-1} + \frac{\omega_k}{2}\right) \\ 0 & 0 & 1 \end{pmatrix} \tag{2.11}$$

$$G_k = \begin{pmatrix} cos\left(\theta_{k-1} + \frac{\omega_k}{2}\right) & \frac{-1}{2} sin\left(\theta_{k-1} + \frac{\omega_k}{2}\right) \\ sin\left(\theta_{k-1} + \frac{\omega_k}{2}\right) & \frac{1}{2} cos\left(\theta_{k-1} + \frac{\omega_k}{2}\right) \\ 0 & 1 \end{pmatrix} \quad (2.12)$$

- $Q_k$ is the covariance matrix associated with the process noise, primarily used to describe noises related to slip and other process-related uncertainties.

**b. The update Step**

The update step is based on the use of observations from sensors mounted on the robot. This step reduces the uncertainty of the odometric motion model.

The robot's pose is obtained from two sources:

- The indoor navigation system (Marvelmind), providing the observation $Z_{1,k} = [x_1 \quad y_1 \quad \theta_1]_k^T$ at time $k$.
- The laser sensor (RPLIDAR) using the ICP algorithm, providing the observation $Z_{2,k} = [x_2 \quad y_2 \quad \theta_2]_k^T$at time $k$.

By combining these two observation vectors, the global observation vector for the robot is defined as follows:

$$Z_k = [x_1 \quad y_1 \quad \theta_1 x_2 \quad y_2 \quad \theta_2]_k^T = [Z_{1,k} \quad Z_{2,k}]^T \quad (2.13)$$

Consequently, the equations for the update step can be expressed as follows:

$$K_k = P_{k/k-1}(H_k)^T \left[H_k P_{k/k-1}(H_k)^T + R_k\right]^{-1} \quad (2.14)$$

$$X_{k/k} = (I - K_k H_k) X_{k/k-1} + K_k Z_k \quad (2.15)$$

$$P_{k/k} = (I - K_k H_k) P_{k/k-1} \quad (2.16)$$

Where is the Kalman gain and $H_k = \frac{\partial h}{\partial X}|_{X_{k/k-1}}$ is defined as the Jacobian matrix of h with respect to $X_{k/k-1}$:

$$H = \begin{bmatrix} 1 & 0 & 0 \\ 0 & 1 & 0 \\ 0 & 0 & 1 \end{bmatrix} \quad (2.17)$$

Through the application of the extended Kalman filter, a precise estimation of the robot's pose is obtained. Detailed experimental results, highlighting the effectiveness of the filter, are provided in [17]. In this study, our attention will be directed towards generating residuals and

subsequently detecting sensor faults that may have an adverse impact on the robot's localization performance.

### 2.3.3. Residual generation

In the context of the considered application, we have applied data fusion and estimation strategy to precisely determine the state (i.e., position and orientation) of the mobile wheeled robot. However, the information provided by any sensor can be disrupted at any moment (due to factors such as intense magnetic fields, data loss, drift, etc.). In this part, we aim to introduce a phase of sensor fault tolerance. This phase involves detecting and isolating faulty sensors to exclude them from the fusion process. To achieve this, a commonly used measure of mismatch is the difference between the observation from the sensor and the prediction of the state by the used evolution model (the odometric model in our case). This measure, called a 'residual', is subjected to an appropriate change detection methodology, which helps exclude any erroneous observations from the fusion and estimation procedure. These residuals serve as anomaly quantifiers between the behavior predicted by a model and that observed through the system's sensors. Their analysis enables fault detection [21-22]. However, it should be noted that there are other methodologies that do not rely on the use of a dynamic evolution model. Examples include fuzzy approaches [23] and artificial neural network-based approaches [24].

During the robot's motion, its wheel encoders contribute to the odometric evolution model to predict its pose. Additionally, at each moment, the robot gathers observations from its onboard sensors. In the case of normal operation (i.e., without faults), this information is consistent. However, in the event of sensor failure, a drift in the estimation of the robot's state relative to the actual state will be observed. After detecting and excluding the faulty sensors, only the correct observations are considered in the fusion algorithm.

At each instant $k$, the residual can be defined as follows:

$$Res_k = Z_k - f\left(X_{k/k-1}\right) \tag{2.18}$$

Where $Z_k$ is the measurement vector and $f\left(X_{k/k-1}\right)$ is the predicted vector.

After the generation of residuals, we will employ a fault detection method to evaluate the state of each sensor, categorizing them as either normal ($u_k = 0$) or faulty ($u_k = 1$). In the nominal case (i.e., without faults), the value of the residual should be close to 0; otherwise, it deviates from it. The primary challenge lies in selecting the threshold applied to these values, ensuring the following property:

$$u_k = \begin{cases} 0 & if\ Res_k < Th_k \\ 1 & otherwise \end{cases} \tag{2.19}$$

In the event of a sensor being faulty, it is removed from the fusion and estimation algorithms. In the subsequent section, we will provide an overview of the current state-of-the-art methods that deal with handling residuals and the selection of appropriate thresholds.

## 2.3.4. Statistical process control: State of the art

In the context of mobile robot localization, SPC [25] is a method employed to ensure the reliability and accuracy of a robot's position estimation. Residuals, which represent the disparities between predicted and actual robot positions, play a pivotal role in this process. SPC leverages these residuals to identify deviations from expected localization behavior, serving as valuable indicators of localization uncertainty or errors. By monitoring and analyzing residuals, mobile robot localization using SPC assists in detecting anomalies, introducing necessary adjustments or interventions, and ultimately enhancing the precision and consistency of the robot's position estimation, contributing to improved navigation and overall performance in autonomous robotic systems. In order to monitor the generated residuals, we propose in this work applying SPC methods with an adaptive entropy-based threshold proposed initially in [26].

In the field of SPC, one of the essential tools is the control chart, also known as the process behavior chart. These charts are widely used in a wide range of applications. In particular, they have been widely implemented as an effective online tool for the detection of anomalies in areas such as industrial manufacturing [27], finance and economics [28-29], computer sciences and telecommunications [30] and in other areas of applications (see, e.g., [31-33]).

First introduced by Shewhart [34], the control chart is recognized as an effective, fast and reliable SPC tool able to detect changes and anomalies in the process characteristics. The control chart is a straightforward graphical tool using sequentially observed data and having correction activities in time. Consequently, the process is focused on a target to maintain its dispersion within a specified tolerance interval. The principle of operation of the Shewhart control chart can be summarized as follows: Let $xN(\mu_0, \sigma^2), k = 1,2,3, \dots, n$ is a sequence of independent observations following a normal distribution with mean $\mu_0$ and standard deviation$\sigma$. The process is considered under control if $x_k$ doesn't exceed the upper and the lower control limits (UCL and LCL), i.e. thresholds value. Commonly, the thresholds are set to$\pm 3\sigma$.

This type of control charts is popular because of its ease of implementation without extensive statistical training together with reduced time and computing resources. However, this technique is effective when the magnitude of change is $2\sigma$ or more. Based only on the current observation, it does not take into account previous observations and loses its effectiveness in detecting small changes in behavior. In contrast, alternative methods have been introduced specifically to address the detection of small changes in the process. The most popular methods are the CUSUM chart initiated by Page [35] and the EWMA chart introduced by Roberts [36]. In particular, these latter methods have the ability to take into account both past and current observations to establish process statistics. Consequently, thanks to this memory aspect, shifts process parameters are detected with fast reaction. The following describes the conventional CUSUM and EWMA control charts.

### a. Conventional CUSUM control chart

The CUSUM chart is typically used for detecting small changes in the mean of a process. It directly integrates all observations into the observation sequence by plotting the cumulative sums of the deviations of the observations from a predefined target value.

The CUSUM algorithm operates through two statistics $C_k^+$ and$C_k^-$. These statistics are called upper and lower sums respectively. They are calculated as follows:

$$\begin{cases} C_k^+ = max[0, X_k - (\mu_0 + K) + C_{k-1}^+] \\ C_k^- = max[0, -X_k + (\mu_0 - K) + C_{k-1}^-] \end{cases} \quad (2.20)$$

Where:

- $C_0^{+C_0^{-=0}}$.
- K is commonly called reference value or tolerance threshold.

The process is considered out of control when $C_k^+$or $C_k^-$ exceeds a threshold $Th$. A typical value of $Th$ is usually defined as $5\sigma$.

**b. Conventional EWMA control chart**

Like the CUSUM chart, the EWMA chart is effective in detecting small changes in the mean of the process. The performance of these two charts is approximately equivalent.

The EWMA statistic is an exponentially weighted average of all previous data, including the most recent measurements. The statistic is defined as follows:

$$z_k = \lambda x_k + (1 - \lambda) z_{k-1}, 0 < \lambda \leq 1 \quad (2.21)$$

With$z_0 = \mu_0$, $\lambda$ is defined as a weighting factor. The upper and lower control limits of the EWMA algorithm are defined as follows:

$$\begin{cases} UCL = \mu_0 + L\sigma \sqrt{\dfrac{\lambda}{(2 - \lambda)}} \\ LCL = \mu_0 - L\sigma \sqrt{\dfrac{\lambda}{(2 - \lambda)}} \end{cases} \quad (2.22)$$

The process is considered out of control when the $z_k$ statistic exceeds one of the control limits. A typical value of L is usually defined as 3.

**c. Recent studies on adaptive control charts**

Generally, the use of the control charts requires the determination of three parameters: the sampling interval that is, how often to sample; the sample size; and the threshold value. By changing one or more of these parameters, control charts are considered adaptive. In this context, a vast literature has been devoted to adaptive control charts that can improve the performance of monitoring process and detecting shifts faster. The first adaptive control charts were based on sample size variation [37-39] . In [40] the author compared the performance of many different adaptive Shewhart control charts and concluded that the adaptive aspects significantly improve the performance of the standard Shewhart control chart. A comprehensive survey covering univariate adaptive control charts up to the end of 1997 was presented by Tagaras [41]. Another

detailed survey discussed recent adaptive Shewhart, CUSUM and EWMA charts focusing on their design, properties and performance was proposed by Psarakis [42].

There have been many recent studies on adaptive charts to improve their performance. Wu et al. [43] proposed a new adaptive CUSUM control chart denoted by **ACUSUM II**. This latter is based on adjusting the reference parameter $K$ of the conventional CUSUM and adding a new feature related to an additional charting parameter $w$, i.e., the exponential of the sample mean shift in $\left(x_t - \mu_0\right)^w$. They compared the proposed chart with seven other CUSUM charts. They found that the ACUSUM II chart is more preferable as it retains most of the advantages of the single-chart schemes, such as the simplicity of design and implementation.

In [44], Abbasi et al. proposed new adaptive CUSUM chart named as **IACCUSUM** chart. The IACCUSUM chart is an adaptive version of the CCUSUM chart proposed by Crosier in 1986 [45]. This update based on an unbiased estimator of the mean shift. Monte Carlo simulations have been used to compute the ARL of these control charts. It has been found that the proposed charts uniformly and significantly outperform their existing counterparts.

Li [46] proposed an adaptive CUSUM chart having adaptive control limit with new cautious parameter learning scheme and he proved that the proposed monitoring procedure is easy to implement, and have better overall performance for detecting different mean shifts than existing methods.

A function based adaptive EWMA control chart (**FAEWMA**) was proposed by Noor-ul-Amin et al. [47]. The idea of this method is based on the determination of the magnitude of the shift with the help with some and then smoothing value of the plotting statistic of the proposed chart is computed as per estimated shift size through unbiased estimator. A comparative discussion with respect to the ARL values proves that their proposed chart is more sensitive to small to moderate shift sizes than the AEWMA chart investigated recently in [48].

Sarwar and Noor-ul-Amin [49] investigated a design of a new adaptive EWMA control chart (**AEWMA CC**). This novel chart introduces a memory-based control chart for monitoring irregular variations in the process mean of a normally distributed process. The concept involves estimating the mean shift by using an estimator that relies on the EWMA statistic and subsequently determining the smoothing constant for plotting EWMA statistics through the use of a proposed continuous function. They found that the AEWMA CC with a small smoothing factor is strong and efficient especially at small shift sizes.

Kim et al. [50] proposed adaptive CUSUM charts with the adaptive runs rule. Abbas et al. [51] proposed a mixed EWMA–CUSUM control chart for detecting a shift in the process mean. Kouadri et al. [52] have developed an adaptive threshold technique based on a two-dimensional defect indicator with a circular control limit. Dey et al. [53] designed an adaptive threshold to remove the effects of modelling uncertainties based on its known bounds and nominal system dynamics. Bakdi, Kouadri, and Bensmail [54] have developed a threshold technique based on a modified EWMA control chart with limited window length.

More recently, Awais and Haq [55] proposed new Shewhart-EWMA and Shewhart-CUSUM control charts using Varied L Ranked Set Sampling for monitoring the process mean.

Haq, Akhtar and Khoo [56] presented adaptive CUSUM and EWMA charts with variable sampling intervals for monitoring the process mean. Haq and Razzaq [57] proposed two types of the weighted adaptive CUSUM chart for monitoring different kinds of shifts in the variance of a normal process. Many other studies have focused on monitoring both process mean and variance – see [58-60].

As shown above, there have been many studies of adaptive control charts to monitor mean or/and variance shifts, either by adjusting the sampling interval, the sample size or the threshold value which highly influences the performance. In this work, we propose enhanced control charts using Adaptive Entropy-based Threshold (AET-Control chart). The purpose of our approach is to find automatically, the threshold value that minimizes the uncertainty of the situation (i.e. normal or faulty hypothesis) knowing the decision. This uncertainty is measured by the Shannon conditional entropy.

Consequently, we present in the following, an adaptive control chart, for which the threshold is learned automatically using an entropy-based criterion. Moreover, a gradient method is presented in order to reduce calculation complexity and facilitate finding this threshold value in real-time. Finally, we present experimental results on the robot platform.

### 2.3.5. Proposed AET-Control chart

Introduced by Claude Shannon [61], information theory initially allowed the resolution of problems related to data transmission and compression. Later, the applications of this theory have been extended to other fields: statistics, signal processing, computer science, cryptography, economics, etc. [62]. Accordingly, a reformulation of the detection strategy by using an entropy-based criterion was initially introduced by Hoballah and Varshney [63]. In this context, we propose to apply an Adaptive Entropy-based Threshold Control chart (AET-Control chart) for monitoring the mean of a process that follows a normal distribution.

This criterion has been compared to the Bayesian criterion and has shown interesting properties [64-65]. The main benefit of this criterion is the ability to determine an adaptive threshold for any change detection techniques based on the (generalized) likelihood ratio.

In this work, we treat the control charts from the point of view of hypothesis testing. Thus, the basic idea of the control charts is similar to the following sequential hypothesis test:

$$\begin{cases} H_0 = S_k N(\mu_0, \sigma_0^2), \\ H_1 = S_k N(\mu_1, \sigma_1^2), \\ k = 1,2, \dots, n \end{cases} \tag{2.23}$$

Where $\mu_1 \neq \mu_0$ and/or$\sigma_1 \neq \sigma_0$. $S_k$ is the used statistic (e.g. $C_k^{+\wedge C_k^-}$ for CUSUM chart; $z_k$ for EWMA chart). In this work, we assume for simplicity that the distributions are Gaussian and that the changes are limited to the mean ($\sigma_1 = \sigma_0$). As long as the statistic $S_k$is within the control limits, the process is assumed to be under control: hypothesis $H_0$ is considered true. However, a statistic that lies outside the control limits is interpreted as evidence that the process is out of control: hypothesis $H_1$ is considered true. Figure 2.4 shows the hypothesis test principle.

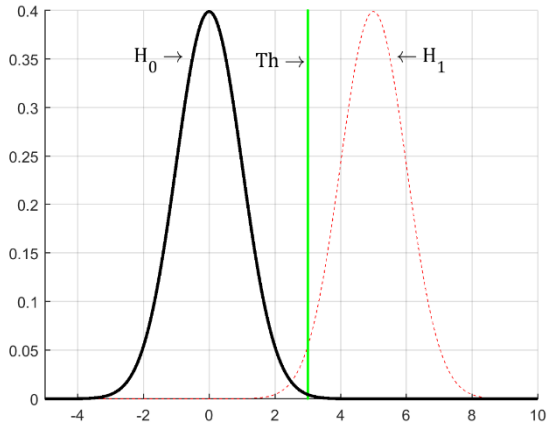


Figure 2.4 Hypothesis test principle.

The objective of the control chart is to detect unusual variations as early as possible, while keeping the probability of a false alarm at a reasonable level. This principle is similar to the hypothesis discrimination. In this context, the decision has two possible values$u \in \{0,1\}$, depending on whether true hypothesis $H$ is considered to be $H_0$ or$H_1$.

The threshold $Th$ is the boundary between the two hypothesis. This value greatly influences the performance of the control chart. For this purpose, we aim at finding, in real time, the most appropriate threshold $Th$ based on an entropy criterion. This latter is explained and detailed in the following.

For a given threshold, and knowing that $H_0$ and $H_1$ follow Gaussian distribution, we can calculate the probability of detection $P_D$ and false alarm $P_F$ as follows:

$$P_D = p(u = 1/H_1) = p(S_k > Th/H_1) \tag{2.24}$$

$$P_F = p(u = 1/H_0) = p(S_k > Th/H_0) \tag{2.25}$$

The proposed criterion is the minimization of the part of $H$ which is not explained by the decision$u$. In other words, the objective is to match the entropy of the true hypothesis $h(H)$ to that of the taken decision$h(u)$. This quantity is defined by Shannon's conditional entropy $h(H/u)$ described as follows (see figure 2.5) [61]:

$$h(H/u) = E\left\{\log\left(\frac{1}{P(H/u)}\right)\right\} = -\sum_{i,j\in\{0,1\}} p(u = i, H_j)\,.\,logp(H_j/u = i) \tag{2.26}$$

This quantity represents the uncertainty on $H$ knowing the decision $u$. It can be expressed according to $P_0, P_D$ and $P_F$as follows [65]:

$$h(H/u) = -\sum_{i\in\{0,1\}} \left[\alpha_i log\frac{\alpha_i}{\alpha_i + \beta_i} + \beta_i log\frac{\beta_i}{\alpha_i + \beta_i}\right] \tag{2.27}$$

With:

$$\begin{cases} \alpha_1 = P_0 P_F \\ \alpha_0 = P_0(1 - P_F) \\ \beta_1 = (1 - P_0)P_D \\ \beta_0 = (1 - P_0)(1 - P_D) \end{cases} \quad (2.28)$$

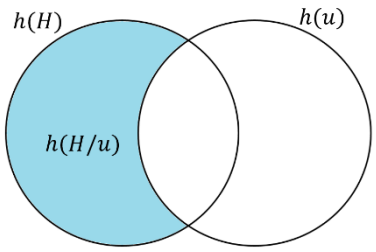


Figure 2.5 Conditional entropy representation.

Therefore, the optimal value of the threshold $Th^{OPT}$is the one that minimizes the conditional entropy$h(H/u)$. In order to find$Th^{OPT}$, an exhaustive search can be considered (see Algorithm 1). It consists of testing all the possible values of $Th$ and keeping only the value minimizing$h(H/u)$. We note that $[Th_{min}, Th_{max}]$ can be set as the bounds of possible threshold values: in our case, we will assume $Th_{min} = \mu_0$ and $Th_{max} = \mu_1$. Furthermore, $\mu_1$ can either be known from the database measures or set according to the desired $ARL_0$ value (will be explained in more detail in the next section).

Algorithm 1: The optimization methodology of the entropy threshold by an exhaustive search

---

$P_0$ is known, Initialize $h_{min} \rightarrow \infty$

For $Th = Th_{min}$ to $Th_{max}$

Calculate $P_D$ and $P_F$

Calculate $h(H/u)$ (Equation 2.27)

If $h(H/u) < h_{min}$

$h_{min} = h(H/u)$

$Th^{OPT} = Th$

End If

End For

---

For each hypothesis, the prior probabilities $P_j$ is assumed to be known (i.e. the probability $P_0$ of $H_0$ is calculated iteratively based on previous iterations). In figure 2.6, a ROC curve illustrates the efficiency of the criterion for $P_0$ allowing from 0 to 1.

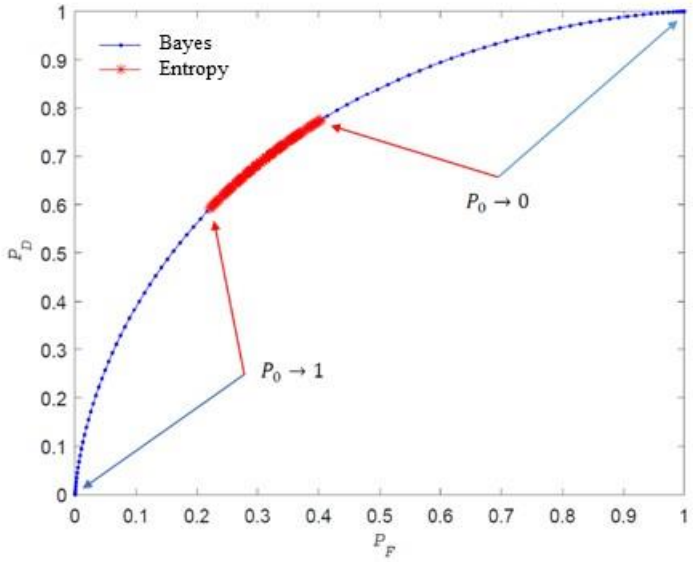


Figure 2.6 ROC curve.

It is worth noting that the entropy criterion allows for a concentration of the entire potential range of values for $P_F$ and $P_D$, represented by the small red arc. Therefore, it is a robust criterion concerning $P_0$. Specifically, when $P_0$ is close to 0 or 1, the ROC curve remains close to the ideal point ($P_F = 0$ and $P_D = 1$). This is not the case with the Bayesian criterion. Indeed, when a rare event occurs (e.g., a sensor error; $P_0$tends to approach 1), the Bayesian criterion neglects this event. The entropy-based criterion takes this event into account significantly.

Furthermore, the exhaustive search is time consuming and requires significant computing resources. To overcome this challenge, and especially in an application requiring real-time operation, a gradient-based technique is much more efficient. The latter will be presented in the following.

## A gradient-based technique

The gradient-based technique consists in finding, as fast as possible, the optimal threshold $Th^{OPT}$ for which $h(H/u)$ is minimum. For a given probability$P_0$, the derivative $\frac{\partial h(H/u)}{\partial Th}$ is a decreasing function when$Th < Th^{OPT}$, and it is equal to zero for$Th^{OPT}$. Accordingly, $h(H/u)$ increasing function otherwise.

Finding the optimal threshold $Th^{OPT}$ is equivalent to find the value of the likelihood ratio $\Lambda = \frac{p(S_k/H_1)}{p(S_k/H_0)}$ for which $\frac{\partial h(H/u)}{\partial \Lambda}\Big|_{\Lambda = Th^{OPT}} = 0$. This equation leads to the following expression:

$$Th^{OPT} = \frac{P_0}{1 - P_0} \times \frac{log\big(1/p\,(H_0/u_1)\big) - log\big(1/p\,(H_0/u_0)\big)}{log\big(1/p\,(H_1/u_0)\big) - log\big(1/p\,(H_1/u_1)\big)} \tag{2.29}$$

The detection rule is then expressed as follows:

$$\frac{p(u/H_1)}{p(u/H_0)} \underset{u=0}{\overset{u=1}{\gtrless}} \frac{P_0}{1-P_0} \times \frac{C_{10}-C_{00}}{C_{01}-C_{11}} = Th^{OPT} \tag{2.30}$$

Where $C_{ij}$ is the cost corresponding to the decision $u_i$when $H_j$ is true. If a wrong decision is made, the system is penalized; if on the other hand a good decision is made, then it is favored. Minimizing $h(H/u)$ thus consists in minimizing an average risk whose costs are no longer constants, as in the Bayesian case, but dependent on a posteriori probabilities. These costs are proposed as follows:

$$C_{ij} = \frac{1}{p\left(H_j/u_i\right)}, i,j = 0,1. \tag{2.31}$$

They can also be represented in terms of detection and false alarm probabilities as follows:

$$\begin{cases} C_{00} = \log\frac{\alpha_0+\beta_0}{\alpha_0} & C_{10} = \log\frac{\alpha_1+\beta_1}{\alpha_1} \\ C_{01} = \log\frac{\alpha_0+\beta_0}{\beta_0} & C_{11} = \log\frac{\alpha_1+\beta_1}{\beta_1} \end{cases} \tag{2.32}$$

Let a new threshold $Th^k$at step$k$ of the algorithm$(k \geq 0)$ calculated from the following equation:

$$Th^k = \frac{P_0}{1-P_0}\frac{C_{10}^{k-1}-C_{00}^{k-1}}{C_{11}^{k-1}-C_{01}^{k-1}} \tag{2.33}$$

Therefore:

$$P_0\left(C_{10}^{k-1}-C_{00}^{k-1}\right) = Th^k(1-P_0)\left(C_{11}^{k-1}-C_{01}^{k-1}\right) \tag{2.34}$$

The derivative of $h(H/u)$can be calculated as a function of the threshold$Th$ according to the following equation [26]:

$$\frac{\partial h(H/u)}{\partial Th^k} = \frac{\partial P_F}{\partial Th^k} \times \left[P_0\left(C_{10}^k-C_{00}^k\right) + Th^k(1-P_0)\left(C_{11}^k-C_{01}^k\right)\right] \tag{2.35}$$

Consequently, we get these equations:

$$\frac{\partial h(H/u)}{\partial Th^{k-1}} = \frac{\partial P_F}{\partial Th^{k-1}}(1-P_0)\left(C_{11}^{k-1}-C_{01}^{k-1}\right)\left(Th^k-Th^{k-1}\right) \tag{2.36}$$

$$Th^k = Th^{k-1} + \frac{\partial h(H/u)}{\partial Th^{k-1}} \left[ \frac{\partial P_F}{\partial Th^{k-1}} (1 - P_0)\left(C_{11}^{k-1} - C_{01}^{k-1}\right) \right]^{-1} \quad (2.37)$$

A recurrence equation is thus obtained:

$$Th^k = Th^{k-1} - \tau^{k-1} \frac{\partial h(H/u)}{\partial Th^{k-1}} \quad (2.38)$$

The stopping condition of this algorithm is $|Th^k - Th^{k-1}| < \varepsilon$, where ε is the accuracy of the threshold value defined by the user. Using equation (2.38) and from any initial state of the threshold $Th^0$, the gradient-based technique will converge towards a locally-optimal solution.

The entropy threshold optimization methodology using the gradient technique is summarized by the figure 2.7.

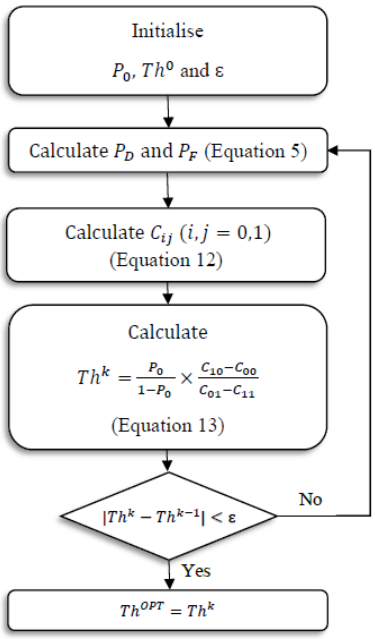


Figure 2.7 The optimization methodology of the entropy threshold using gradient technique.

## 2.3.6. Experimental results

In this section, we analyze the application of the proposed AET-Control chart within the context of the mobile robot platform.

In this context, we consider the residual $Res_k$ as the disparity between the Marvelmind measurement and the odometric evolution model calculated by the wheel encoders (refer to section 2.3.3).

The Marvelmind measurements exhibit proximity to the odometric evolution model with some inherent noise (Hypothesis $H_0$). Consequently, the residual $Res_k$ approximately follows a Gaussian distribution with a mean $\mu_0 \cong 0$ and a standard deviation $\sigma \cong 1$. Conversely, after adding simulated sensor faults (Hypothesis $H_1$), the Marvelmind measurements diverge from the

odometric evolution model, leading to a change in the mean or standard deviation of the residual $Res_k$.

The experimental data were obtained in a simple scenario lasting 20 seconds, with a frequency of 10Hz, leading to a total of 200 iterations. The robot moved at a speed of 0.11 m/s. Figure 2.8 displays the Marvelmind (in green) and the odometric evolution model (in black) trajectories. Due to the relatively short travel distance, the trajectories closely align. To simulate an out-of-control process (sensor faults), a bias is introduced to the Marvelmind measurements, starting from the 101st iteration. The goal is to promptly detect this simulated faults. In Figure 2.29, the fault-free residuals (on the x-axis) are contrasted with the residuals when a fault is introduced into the Marvelmind system.

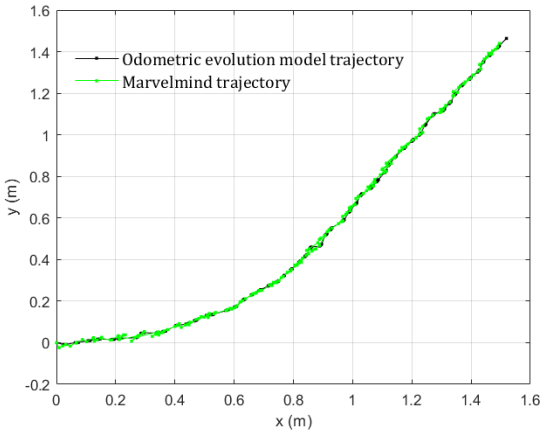


Figure 2.8 Visualization of the odometric evolution model and the Marvelmind trajectories.

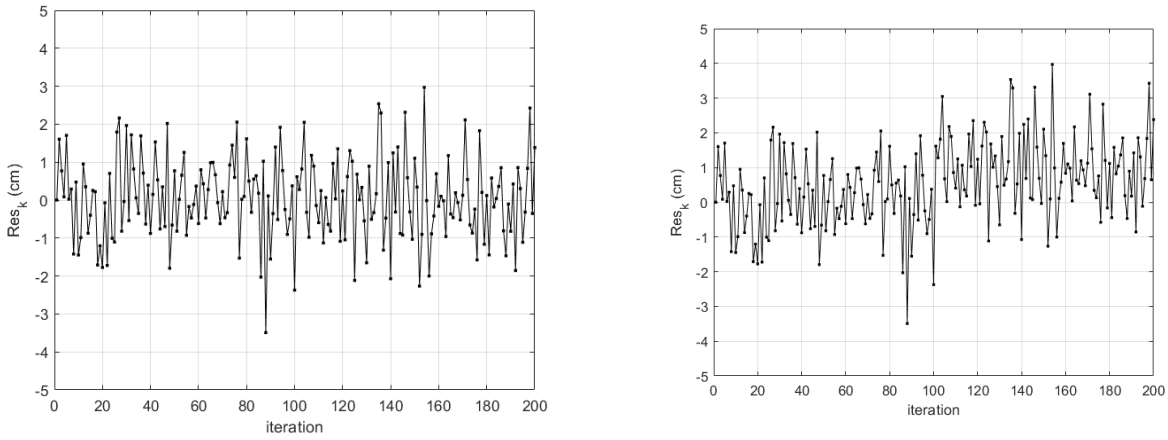


(a) (b)

Figure 2.9 Visualization of the residuals : $Res_k$ (a) without faults – (b) with introduced fault from the 101st iteration with a mean shift 1.

We apply the Shewhart, CUSUM and EWMA charts respectively with the following parameters (commonly used in the literature):

- Shewhart: Fixed threshold $Th = 3$
- CUSUM: Fixed threshold $Th = 5; K = 0.5$

- EWMA: $L = 3.054; \lambda = 0.4$

On the other hand, we apply the proposed AET-Control chart. In this context, the *apriori* probability of the normal hypothesis $H_0(P_0)$ is calculated iteratively as the ratio of the number of iterations of $H_0$ (under the threshold value) to the total number of iterations, starting with an initial value of 1. The faulty hypothesis $H_1$ represents the faulty case (the added sensor faults) to be detected:$N(\mu_1 = 1, \sigma = 1)$.

For Shewhart chart, figure 2.10 shows the residual $Res_k$ (black curve), the fixed and the adaptive threshold (red and green curve respectively). Similarly, figure 2.11 shows the statistics $C_k^+$ and $C_k^-$ determined from the CUSUM chart (black curve), the fixed and the adaptive thresholds (red and green curve respectively). Finally, figure 2.12 shows the statistic $z_k$ determined from the EWMA chart (black curve), the Upper and Lower Control Limits UCL/LCL with the fixed and the adaptive threshold (red and green curve respectively).

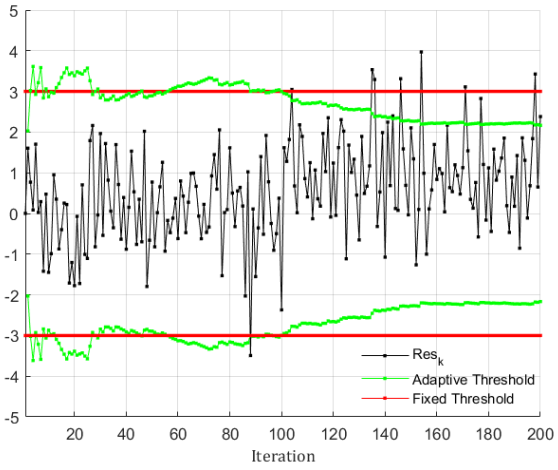


Figure 2.10 Shewhart – results with fixed/adaptive thresholds.

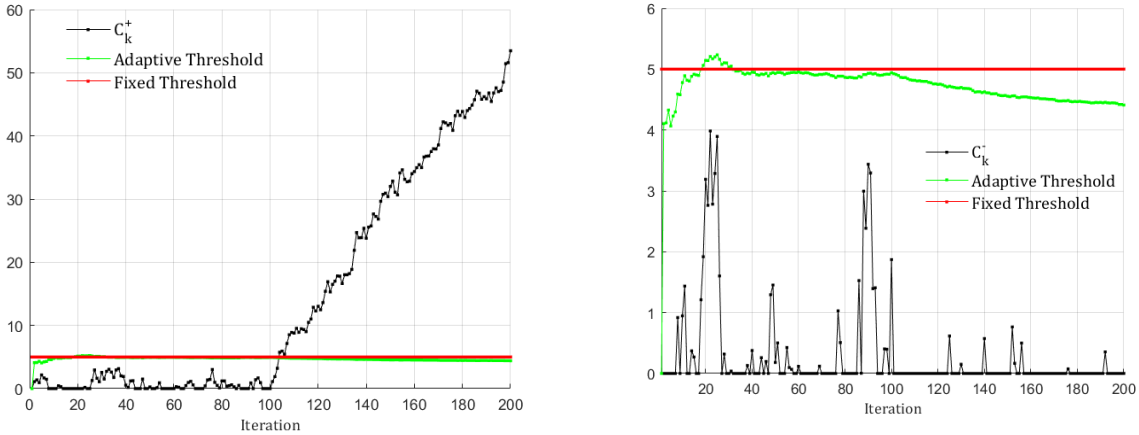


(a) (b)

Figure 2.11 CUSUM chart– results with fixed/adaptive thresholds.

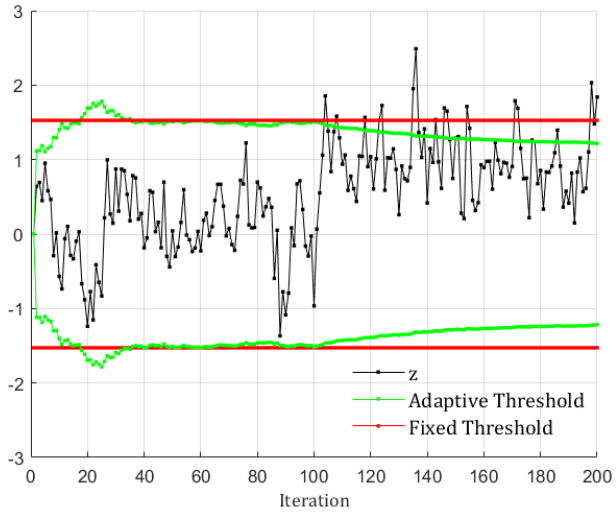


Figure 2.12 EWMA – results with fixed/adaptive thresholds.

Using the conventional control charts, the threshold being fixed, we observe several missed detections (especially in figures 2.10 and 2.12). In contrast, using the proposed approach, the calculated threshold is more adapted to the measured statistics. This threshold is intended to be more sensitive when the change model has occurred. This is done by learning from the behavior of the process, minimizing the uncertainty of the decision with respect to the true hypothesis over time (principle of the entropy criterion). Therefore, our approach can detect the anomaly (the mean shift) more efficiently and without prior knowledge of the detection threshold.

### 2.3.7. Conclusion

In this section, we have introduced a localization approach based on the extended Kalman filter. We have assessed the system's robustness in the face of sensor faults by employing a combination of residual generation and change detection methods. For this purpose, we have provided an overview of the state of the art in the SPC. Furthermore, we have proposed an improvement in the form of an adaptive threshold, by using an entropy-based criterion. Additionally, we have presented experimental results conducted on the robot platform, showcasing a more robust localization system when faced with sensor faults.

In the following section, we delve into a detailed examination and evaluation of the performance of the adaptive threshold approach, using the most widely used tool: the ARL. We also provide a comparative analysis with various approaches found in the existing literature.

## 2.4. Performance evaluation: Average Run Length (ARL) study

### 2.4.1. Introduction

In this section, the performance of the proposed AET-Control chart approach is evaluated in terms of the ARL values computed through Markov Chain (MC) method. This evaluation is

conducted using data obtained from the robot platform. The determined ARL values are compared with the following adaptive control charts:

(a) ACUSUM II [43],

(b) IACCUSUM [44],

(c) Adaptive CUSUM with cautious parameters [46],

(d) FAEWMA [47],

(e) AEWMA CC [49].

The remainder of this section is structured as follows: we first provide an explanation of the ARL metric employed for the evaluation. Following that, we proceed to assess the effectiveness of the proposed AET-control chart, conducting a comparative analysis against the recently published adaptive control charts from the aforementioned literature.

### 2.4.2. Average Run Length definition

The Average Run Length is a key parameter in control chart analysis, it has been commonly used as a performance indicator adopted to compare and evaluate the effectiveness of various control charts. The ARL is defined as the average number of samples before an out-of-control signal is detected. If the observations of the process are independent (e.g. Shewhart control chart), then the ARL can be determined exactly according to the following relationship:

$$ARL = \frac{1}{p(out - of - controlsignal)} \tag{2.39}$$

In the case where we have no mean shift in the process, the value of ARL is the 'in-control' average run length and is denoted as$ARL_0 = 1/\alpha$, where $\alpha$ is the probability of false alarms. $ARL_0$ should therefore be as large as possible to minimize the probability that an out-of-control signal is a false alarm.

On the other hand, when we have a change in the process mean, the ARL value is the 'out-of-control' run length and is denoted as$ARL_1 = 1/\beta$, where$\beta$ is the probability of missed detections. $ARL_1$should be as small as possible so that a change in the process mean is quickly detected.

In the CUSUM and EWMA control charts, the plotted statistics are correlated. Therefore, the ARL cannot be calculated directly by the equation (2.39). Various methods are effective alternatives for estimating the ARL values.

The main methods for ARL computation are the Markov chain approach [66], the integral equation approach [67] and Monte Carlo simulation [36] . In this study, we have chosen the Markov chain approach (APPENDIX A) because of its ease of implementation, as well as the accuracy of its results for both CUSUM and EWMA charts. In the following, we outline the study focused on evaluating the ARL.

## 2.4.3. ARL numerical comparison

Since the $ARL_0$ represents the false alarm rate of the control charts, it is convenient to set it to a desired and identical level for all the control charts being compared. Then, the performance evaluation is based mainly on $ARL_1$ for the out-of-control situation: the control chart is considered the most sensitive and best performing if it has the smallest $ARL_1$ value.

The ARL values are calculated based on the dataset obtained from the residual measurements, which represent the difference between the Marvelmind measurements and odometric evolution model, following a normal distribution with mean $\mu_0 = 0$ and the standard deviation $\sigma = 1$. In this study, the average process shift $\delta$ goes from 0 to $2\sigma$ with a step size of$0.25\sigma$. This simulated shift is incorporated in the residual measurements, representing the deviation of Marvelmind data from the odometric evolution model.

For convenience, we refer to the control charts with the proposed entropy-based adaptive control chart as the AET-Shewhart chart, AET-CUSUM chart and AET-EWMA chart.

### i. Shewhart charts

The performance comparison of the conventional Shewhart (with fixed threshold) and the AET-Shewhart charts (with adaptive threshold) is presented in the table 2.1. We desire to have$ARL_0 = 370$. To attain this target, the fixed threshold of the conventional Shewhart control chart will be chosen equal to 3 and for the AET-Shewhart chart we set $\mu_1 = 2.75$.

| PROCESS MEAN SHIFT ($\delta$) | SHEWHART | AET-SHEWHART |
|---|---|---|
| **0** | 370.38 | 370.74 |
| **0.25** | 281.11 | **106.69** |
| **0.5** | 155.2 | **29.86** |
| **0.75** | 81.21 | **10.37** |
| **1** | 43.89 | **4.68** |
| **1.25** | 24.95 | **2.66** |
| **1.5** | 14.97 | **1.82** |
| **1.75** | 9.46 | **1.43** |
| **2** | 6.30 | **1.23** |

Table 2.1 ARL comparison of conventional and proposed AET-Shewhart charts for$ARL_0 = 370$.

### ii. CUSUM charts

Concerning CUSUM charts, the performance of five methods is compared, the parameters are set as follows:

**The conventional CUSUM chart**

We choose the reference$K$equal to 0.5 as commonly used [68], and the fixed threshold $Th$is equal to 5. Thus, we get the $ARL_0$ equal to 500.

**The AET-CUSUM chart**

We set $\mu_1 = 4.91$to obtain $ARL_0$ = 740 and $\mu_1 = 4.48$ to obtain $ARL_0$= 500.

**ACUSUM II, IACCUSUM, and Adaptive CUSUM with new cautious parameter**

We directly use the values of ARL existing in the articles for $ARL_0$=740 and for $ARL_0$=500.

The comparison results are presented in the following tables. In table 2.2, we compare our proposed approach (AET-CUSUM) with ACUSUM II, for $ARL_0 = 740$. In table 2.3, we compare our proposed approach with the conventional CUSUM, IACCUSUM, and ADAPTIVE CUSUM with cautious parameters, all for an $ARL_0$ of 500.

| PROCESS MEAN SHIFT ($\delta$) | AET-CUSUM | ACUSUM II |
|---|---|---|
| **0** | 740.22 | 739.16 |
| **0.5** | **37.91** | 40.15 |
| **1** | **9.30** | 10.14 |
| **1.5** | **4.65** | 5.22 |
| **2** | **2.85** | 3.38 |
| **2.5** | **1.90** | 2.42 |
| **3** | **1.32** | 1.85 |

Table 2.2 ARL comparison of the AET-CUSUM and ACUSUM II control charts for$ARL_0 = 740$.

| PROCESS MEAN SHIFT ($\delta$) | CONVENTIONAL CUSUM | AET-CUSUM | IACCUSUM | ADAPTIVE CUSUM WITH CAUTIOUS PARAMETERS |
|---|---|---|---|---|
| **0** | 500 | 501.40 | 500 | 500 |
| **0.25** | 145.56 | **124.10** | 136.23 | 184.3 |
| **0.5** | 38.88 | **33.49** | 35.40 | 36.6 |
| **0.75** | 17.32 | **14.30** | 15.38 | 17.85 |
| **1** | 10.52 | **8.25** | 8.93 | 11.25 |
| **1.25** | 7.49 | **5.6** | 6.11 | 8.02 |
| **1.5** | 5.82 | **4.06** | 4.54 | 6.09 |
| **1.75** | 4.77 | **3.10** | 3.57 | 4.78 |
| **2** | 4.06 | **2.45** | 2.93 | 4.01 |
| **2.5** | 3.15 | **1.61** | 2.13 | _ |
| **3** | 2.60 | **1.18** | 1.66 | _ |

Table 2.3 ARL comparison of the conventional CUSUM, AET-CUSUM, IACCUSUM, and adaptive CUSUM with cautious parameters control charts for$ARL_0 = 500$.

### iii. EWMA chart

Concerning EWMA chart, the performance of four methods is compared (table 2.4), the parameters are set as follows:

**The conventional EWMA chart**

The ARL values of the conventional EWMA are taken from [69] for$\lambda = 0.5 \wedge L = 3.071$.

**The AT-EWMA chart**

We set $\lambda = 0.5 \wedge \mu_1 = 1.71$ in order to obtain $ARL_0 = 500$.

**FAEWMA and AEWMA CC charts**

The ARL values are those such that the conditions are satisfied with $ARL_0$ = 500.

| PROCESS MEAN SHIFT ($\delta$) | CONVENTIONAL EWMA | AET- EWMA | FAEWMA | AEWMA ACC |
|---|---|---|---|---|
| **0** | 500 | 503.67 | 500.85 | 500.51 |
| **0.25** | 255 | 82.69 | 99.49 | **70.55** |
| **0.5** | 88.8 | **21.31** | 24.44 | 26.21 |
| **0.75** | 35.9 | **8.71** | 9.64 | 13.68 |
| **1** | 17.5 | **4.86** | 5.05 | 8.75 |
| **1.25** | _ | **3.82** | _ | 6.04 |
| **1.5** | 6.53 | **2.57** | 2.3 | 4.57 |
| **2** | 3.63 | **1.84** | 1.54 | 2.96 |
| **2.5** | 2.50 | **1.56** | _ | 2.09 |
| **3** | 1.93 | **1.53** | _ | 1.56 |

Table 2.4. ARL Comparisons of the conventional EWMA, AET-EWMA FAEWMA and AEWMA ACC control charts, for$ARL_0 = 500$.

### iv. Discussion

In our analysis, the effectiveness of the proposed AET-Control chart becomes evident as it consistently outperforms conventional Shewhart, CUSUM, and EWMA control charts with fixed threshold across all magnitudes of process shifts. Notably, the ARL associated with the AET-Control chart exhibits a decreasing value as the shift size increases, indicating its ability to promptly detect significant alterations in the process mean.

Tables 2.2 and 2.3 present compelling evidence, showing that the proposed AET-Control chart excels in comparison to other adaptive control charts for small to moderate shifts ($\delta \leq 1$), while the performance of these methods tends to converge for detecting larger shifts ($\delta > 1$). This observation underscores the robustness of the AET-Control chart in a wide range of scenarios.

Furthermore, in table 2.4, we observe that the AET-EWMA chart consistently outperforms FAEWMA and AEWMA ACC for shifts ranging from 0 to 1, with the exception of $\delta = 0.25$, where AEWMA ACC takes the lead. When it comes to large shifts, the AET-EWMA and FAEWMA charts demonstrate similar performance, reinforcing the efficacy of the AET approach across various magnitudes of process change.

## 2.4.4. Conclusion

In this section, a comparative study has been presented with seven different control chart techniques in the literature. Markov Chain simulations have been used to compute the ARL

values of these control charts. It has been found that the proposed technique outperforms the conventional control charts with fixed thresholds and other recent adaptive control charts existing in the literature. Based on the current work, AET-Control charts perform well in detecting small to large changes in the process mean.

## 2.5. Conclusion

In this chapter, our central objective was to establish a fault tolerant fusion system with the capacity to improve the localization of robotic system. This goal necessitated a thorough analysis of various components, encompassing the use of the Extended Kalman filter for achieving high accuracy in robot localization, the generation of residuals, and a comprehensive overview of the latest advancements in SPC.

The main contribution was the introduction of the AET-Control chart, a promising approach to enhancing change detection. Subsequently, we conducted an in-depth performance evaluation through an ARL study. This evaluation aimed to quantify the efficiency of our proposed method and involved a numerical comparison of ARLs. The results highlighted the robustness of our AET-Control chart, particularly in scenarios involving small to moderate shifts, where it exhibited superior performance compared to other control charts documented in the literature. In summary, this chapter has led to the development of an innovative approach that demonstrates substantial promise in the field of robot localization. The fusion of multiple sensors, coupled with advanced statistical control techniques, has the potential to significantly enhance the precision and fault tolerance of robotic systems.

An essential aspect of this work is the integration of antennas on the robots. With the integration of antennas into our robotic system, with high-precision and fault-tolerant localization, we anticipate a substantial improvement in the overall results of our research. It should be noted that a previous thesis established the groundwork by carrying out a proof of concept for the implementation of microwave techniques on a mobile robot system [17]. Expanding upon this foundation, the following chapters introduce microwave techniques designed for precise materials characterization.

# Chapter 3. Conventional microwave techniques and limitations

## Chapter outlines

## 3.1. Introduction

Nondestructive testing and evaluation (NDT&E) is a concept associated to a set of techniques used to inspect, analyze, and assess the properties, integrity, and quality of materials without causing any damage to the material being examined [70-71]. More specifically, NDT&E allows to identify defects, flaws, irregularities, or potential failures within materials or structures, thus enabling proactive maintenance, quality control, and safety assessments. NDT&E plays a critical role in various industries, including aerospace, automotive, construction, manufacturing, power generation, and more [72-75]. By employing these methods, engineers and technicians can gain valuable information about the condition and properties of the tested materials, ensuring that they meet required standards and comply with safety regulations.

NDT&E includes a wide range of testing methods [76-78]. Each method is designed to address specific applications and related materials. Established and common NDT&E techniques include: visual inspection, ultrasonic testing, radiographic testing, magnetic particle testing, liquid penetrant testing, eddy current testing, acoustic emission testing, etc. [79-82]. Among these methods, techniques based on electromagnetic radiations have attracted both the scientific and industrial communities, as they provide benefits such as penetration into materials and possibility to operate in a contact/non contact manner. A classification of these methods thanks to their wavelengths of operation is illustrated in figure 3.1. Microwave nondestructive testing and evaluation (MNDT&E) concept is considered in this work.

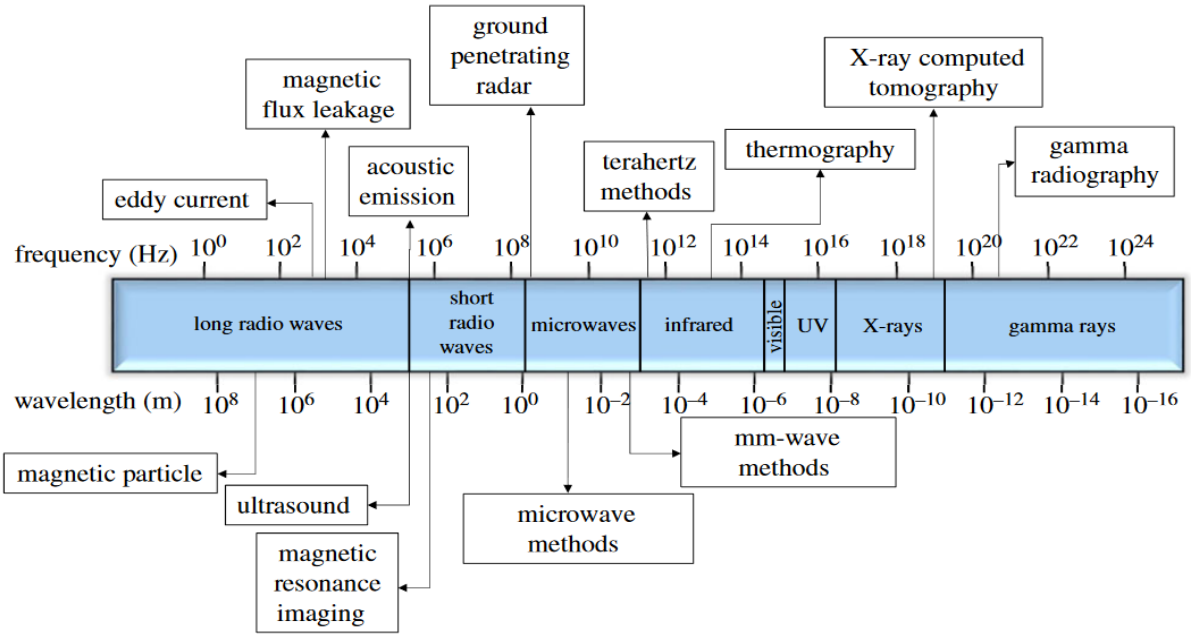


Figure 3.1 Non-destructive and evaluation techniques on the frequency spectrum [83].

MNDT&E was initially introduced in the 1970's to characterize the dielectric properties of solid materials [84]. The idea was to use microwave electromagnetic waves in the frequency range of 300 MHz to 300 GHz to penetrate and interact with materials and provide important information about their internal structures and hidden flaws. The potential of MNDT&E lies in its

ability to inspect a wide range of materials, including composites, ceramics, polymers, and even dielectric materials (e.g. concrete) with a high level of precision and efficiency [85-87]. MNDT&E methods are non-ionizing in contrast with X-ray or Gamma-ray techniques. The non-invasive nature of this technology allows for remote inspection, rapid testing, and real-time monitoring. MNDT&E techniques have been widely employed in various applications, such as medical application [88-89],the characterization of dielectric materials [90-91], the detection and evaluation of defects in different structures [92], and the identification and measurement of fatigue cracks on metal surfaces [93].

This chapter begins with presenting the theoretical background of microwave characterization, including general basis of the electromagnetic properties of materials, microwave measurement systems, and characterization techniques. Following this, we propose a free-space monostatic MNDT&E technique for low-power, non-ionizing, contactless, and real-time characterization of dielectric materials. The proposed measurement system is built up with conventional and commercially available microwave systems to measure the near-field complex reflection $S_{11}$ of planar dielectric materials. Dedicated modeling and calibration procedure are then used to extract the complex permittivity in order to characterize these materials (i.e. recognize their types). We initiate the process with the use of a double ridge guide horn antenna as the primary instrument, followed by a transition to a more compact and simplified horn antenna. Both antennas are subject to comprehensive testing and evaluation under controlled laboratory conditions.

The reminder of this chapter is organized as follows. In the first section, a dedicated state of the art is presented. Then, the measurement setup based on the double ridge guide horn antenna is presented, along with detailed explanation of the calibration procedure. In the third section, we present the measurement setup based on the more compact and simple horn antenna. Finally, the chapter concludes with a discussion section, where we analyze and compare the outcomes and limitations of the two measurement approaches.

## 3.2. Microwave characterization: State of the Art

For decades, microwave characterization techniques have been employed within both research and industry communities. These characterizations provide valuable insights into material health and properties. This section aims to provide a comprehensive synthesis of the fundamental theoretical principles covering the electromagnetic waves-to-material interaction, along with the corresponding instrumentations. Primarily, the electromagnetic properties of materials are presented. Subsequently, the definition of the scattering parameters is introduced. The final section pertains to the presentation of microwave measurement systems.

### 3.2.1. Electromagnetic properties

At microwave frequencies, the properties of a dielectric materials is basically characterized by its complex permittivity [94]. The complex permittivity ($\varepsilon^*$) describes the interaction of a dielectric material with an applied sinusoidal electric field $\vec{E}$. $\varepsilon^*$ has two parts: the real part ($\varepsilon'$) and the imaginary part ($\varepsilon''$). These parts are related to the storage and dissipation components of electrical energy in the dielectric material, respectively.

$$\varepsilon^* = \varepsilon' - j\varepsilon'' = \varepsilon_0\varepsilon_r^* = \ \varepsilon_0(\varepsilon_r' - j\varepsilon_r'') \quad (3.1)$$

- $\varepsilon'$represents the real part of the complex permittivity, or dielectric constant, which indicates how the material responds by storing electrical energy in a varying electric field. A higher $\varepsilon'$ implies a higher capacity of the material to store electrical energy as polarization.
- $\varepsilon''$(dielectric loss factor) is the imaginary part of the complex permittivity and represents the material's ability to dissipate electrical energy as heat. A higher $\varepsilon''$ implies a more dissipative material that converts electrical energy into heat.
- $\varepsilon_r^*$ represents the complex permittivity relative to free-space.
- $\varepsilon_0$ represents the free-space permittivity.

Thus, by using microwave techniques, electromagnetic waves interact with dielectric materials, i.e. are partially reflected by the surface material and partially penetrate dielectric materials. Based on the analysis of the material's permittivity, this interaction provides valuable information about the MUT, including its type, geometry, and the presence of surface or subsurface defects.

### 3.2.2. Scattering parameters definition

At microwave and millimeter waves frequencies (300 MHz to 300 GHz), propagation phenomena result in variations of voltages and currents along transmission lines. Impedance, admittance, or hybrid matrices, which are related to voltage and current concepts, are difficult to describe. Instead, pseudo-waves related to the concept of power are preferred, as power is easily measurable in microwave and millimeter wave frequency ranges [95]. This approach allows the use of the scattering parameters (S-parameters) matrix to describe the system.

Pseudo-waves are purely mathematical quantities defined with respect to an arbitrary reference impedance for each access point of the circuit. The S-parameters are a set of measurements used to characterize the behavior of a microwave circuit, network, or device, as they provide information about impedance matching, power transfer, and signal integrity. They describe the voltage ratios of incident waves $a_1$, $a_2$ and reflected electromagnetic waves $b_1$, $b_2$ at the ports of the circuit (figure 3.2).

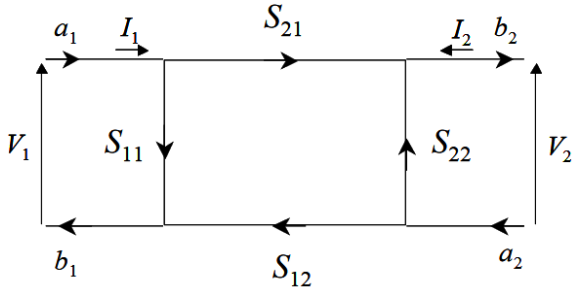


Figure 3.2 Graph illustrating a quadrupole circuit [95].

For a dipole, the reflection coefficient:

$$S_{11} = \frac{b_1}{a_1} \tag{3.2}$$

For a two-port network, the S-parameters are represented as a matrix:

$$\begin{bmatrix} b_1 \\ b_2 \end{bmatrix} = \begin{bmatrix} S_{11} & S_{12} \\ S_{21} & S_{22} \end{bmatrix} . \begin{bmatrix} a_1 \\ a_2 \end{bmatrix} \tag{3.3}$$

Where,

- $S_{11}$ represents the reflection coefficient at port 1 (reflection from port 1).
- $S_{12}$ represents the transmission coefficient from port 2 to port 1.
- $S_{21}$ represents the transmission coefficient from port 1 to port 2.
- $S_{22}$ represents the reflection coefficient at port 2 (reflection from port 2).

In summary, using microwave techniques to study the variations in electromagnetic properties, such as permittivity, by analyzing S-parameters provides a reliable approach for material characterization. This thesis specifically focuses on using the measured magnitude and phase of the reflection coefficient $S_{11}$ considering a monostatic measurement configuration. By doing so, it aims to provide an in-depth comprehension of material behavior and enhance the capability to identify defects with higher accuracy.

### 3.2.3. Microwave measurement systems

#### a. Vector network analyzer (VNA)

The Vector Network Analyzer (VNA) is the commonly employed measurement instrument to determine the S-parameters [96]. VNAs were commonly though as laboratory instruments due to their high cost, weight, size, and complexity. However, with the development of modern commercial VNA solutions, it has become widely used in various applications. These updated VNA solutions have effectively addressed the limitations of the past and are now extensively used across diverse sectors.

A VNA generally consists of a frequency synthesizer module, a module for separating signals (incident, reflected and transmitted) into various channels, and a heterodyne detection module for the vector measurement of waves [94]-[97]. The use of the VNA generates two categories of measurement errors: random errors (non-reproducible) and systematic errors (reproducible) [96]. Random errors are related to the environmental variations (humidity, temperature, mechanical vibrations) and the measurement system itself. These variations can be minimized by reducing the intermediate frequency bandwidth (IFBW) and employing averaging techniques. On the other hand, systematic errors are characteristics of the measurement set-up and are reproducible. These errors can be corrected through a vector calibration procedure, also known as ‘calibration’. The standard procedure for calibrating a VNA involves connecting a set of well-known DUTs, including a short, open, and known load in one-port configuration. The remaining step consists to calculate error parameters that relate measured quantities to calibrated ones [94].

The configuration of a VNA requires the precise adjustment of several key parameters to ensure accurate measurements and the operational performance of the VNA. These parameters of interest are:

- **Frequency range**: Setting the desired frequency span for measurements.
- **Sweep Time**: Specifies the time the analyzer takes to acquire data for a sweep.
- **Number of points**: Specify number of data points that the VNA measures during a sweep.
- **Intermediate frequency bandwidth (IFBW)**: Refers to the width or range of frequencies within the intermediate frequency (IF) domain that the VNA is capable of measuring during a scan. A smaller IFBW indicates a smaller frequency range, which can help reduce noise and improve measurement resolution but may result in longer scan times. Inversely, a larger IFBW allows for a wider frequency range to be processed, which can speed up measurements but may compromise noise performance and resolution. The choice of IFBW depends on the specific measurement requirements and the compromise between measurement speed and accuracy.
- **Power level**: Adjusting the signal power for optimal measurements.

## b. Six-port reflectometer

The Six-Port Reflectometer has gained increasing attention in research laboratories and metrology institutes. Its simplicity of implementation, low cost, small form factor integration and high performance for measuring microwave phase-shifts make it a valuable tool for conducting characterizations outside a laboratory environment [98].

This instrument was first introduced by Glenn F. Engen in the 1970s [99]. The general schematic diagram is illustrated in the figure 3.3. The term ‘six ports’ is directly derived from the structure itself, which consists of two input ports and four output ports. The microwave reference signal feeds into the six-port network through port 1. The MUT, for which we aim to determine the reflection coefficient, is connected to port 2. The remaining four ports are connected to power detectors. Power measurements followed by mathematical data processing enable the measurement of the complex reflection coefficient. Therefore, the performance of the six-port reflectometer depends on both the hardware and the calibration of the measurements. In this context, various calibration methods have been proposed [100-102].

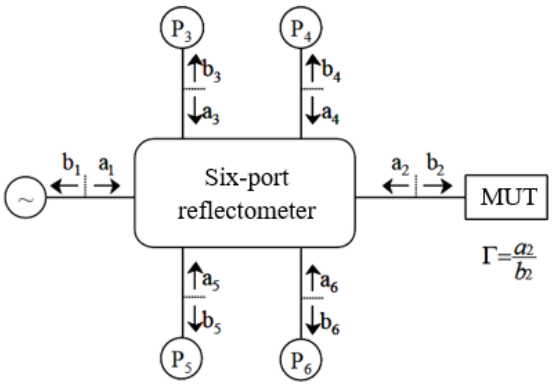


Figure 3.3. Six-port architecture [100].

The six-port reflectometer finds numerous applications, such as in radars for distance or velocity measurements [103-104], precise geometrical measurements [105-106], radar and imaging applications [107-109], medical applications [110], material characterization [111] and other applications [112-113].

### 3.2.4. MNDT&E techniques for material characterization and defects detection

MNDT&E field has gained recent recognition from the American Society for Nondestructive Testing, being classified as a 'Method' on its own [114]. Highly suitable for material characterization, defects detection and evaluation, microwaves techniques achieve this capability by effectively penetrating the materials with high sensitivity to changes in dielectric properties [115-116]. Several practical advantages are associated with these techniques. They include non-contact operation, low power requirements, real-time data provision, compatibility with autonomous robotic systems, generation of high-resolution images, and the ability of cost-effective testing solutions [117-118].

Consequently, a wide variety of MNDT&E techniques have been developed. These methods primarily rely around the measurement of S-parameters of the MUT [119]. Subsequently, an appropriate approach is necessary to shift from the measured parameters to the electromagnetic characteristics of the MUT. Such a procedure might involve well-established mathematical modeling based on the physical principles that relate the measured parameters to the electromagnetic properties. Alternatively, it could also involve modern technological advancements, such as the integration of ML and DL models, which have proven to be valuable tools in facilitating this transition.

Furthermore, various parameters should be considered when selecting a MNDT&E measurement method such as frequency range, sample preparation, sample surface roughness, required measurement accuracy, moisture and temperature [100] - [110] - [120].

In the following, we present most common MNDT&E methods for material characterization and evaluation. These methods are categorized into resonant and non-resonant techniques. Additionally, we discuss the recent advancements in this field, including the integration of ML and DL models with MNDT&E techniques.

#### a. Resonant methods

Resonant methods give precise information on the electromagnetic properties of materials over a limited frequency range. The measurements focus on changes in the resonance frequency and quality factor (Q). By analyzing these parameters, it becomes possible to determine the complex permittivity $\varepsilon_r$ of the MUT. This extraction is typically performed within a narrow frequency range or at a single frequency [121]. Various studies based on resonant microwave technique for material characterization and defect detection can be found in the literature [122-126]. For example, in[127], the authors presented a novel approach that uses a microwave sensor array with an advanced ML model to effectively classify three distinct materials: cardboard, wood, and plastic. The sensor array comprises five planar resonating elements, each functioning at a unique frequency within the range of 1 GHz to 10 GHz. The study demonstrates that the proposed ML model outperforms traditional classification models, highlighting its superior performance in material classification tasks. In [90] a compact microwave resonant sensor

operating in the unlicensed 2.5 GHz band is used for the identification of four distinct plastic materials in pellet form. The classification of these materials is accomplished thanks to ML algorithms that use resonant parameters, specifically the resonance frequency and quality factor, as features. In [93] authors introduce a microwave direction-sensitive sensor for metal crack detection. This sensor adopted two feeding ports to obtain perpendicular polarization currents, thus realizing directional detection. The performance was validated by both simulations and experiments. The results showed that the two feeding ports had width sensitivities of 100 MHz/mm and 63.3 MHz/mm respectively.

## b. Non resonant methods

Non-resonant methods are inherently broadband. They relate the measured S-parameters to the dielectric properties of the MUT. These characterization techniques include coaxial probing [128], free-space methods [129] or open-ended waveguide (OERW) [130-131]. Every method comes with its distinct limitations and constraints, and the selection of the appropriate method is determined by the specific application it is intended for. In this context, the thesis we focus on two microwave characterization approaches including both a monostatic **free-space** setup with a single antenna and an alternative approach based on a **rectangular open-ended waveguide (OEWR)**.

Free-space measurements techniques have the advantages of allowing reflection and transmission measurements without contact with the sample, simplicity in MUT preparation, ability to characterize high temperature materials, and simple measurement setup [132]. In its standard configuration, the free space measurement setup comprises of a VNA, two horn antennas and a sample holder. Each horn antenna will be placed as the transmitter and receiver antenna respectively, and the MUT will be placed between them as presented in figure 3.4 [133]. However, its implementation within an industrial environment proves to be challenging due to the required equipment. In such cases, monostatic measurements are preferred. These measurements rely on the use of a single antenna for both transmitting and receiving waves (figure 3.5), often associated with radar techniques. This method is particularly well-suited for applications where access to only one side of the MUT is feasible [134].

The dielectric properties of the MUT are then extracted from the measured reflected and/or transmitted signals (i.e. $S_{11}$ and$S_{21}$) using appropriate conversion methods. This latter is mandatory to identify the types of materials. Significant studies have taken place using free-space measurement techniques for material characterization. For example, in an earlier well cited work [132], a system was introduced for measuring dielectric properties of moist granular materials. The system used a free-space measurement approach in the frequency range from 5 to 17 GHz at a temperature of$23^{o}$. It is based on employing a horn/lens antenna and a vector network. In [135] a microwave free-space measurement system was introduced for evaluating the complex permittivity of liquid samples. This approach involved measuring the S-parameters of quartz plates. Subsequently, a container was created using these plates, housing liquid samples to form a quartz plate-liquid-quartz plate arrangement. The measured S-parameters of the assembly were de-embedded, leading to calibrated S-parameters of the tested liquid material. In [91] a microwave sensor for characterizing the complex relative permittivity of concrete samples is proposed. The sensor operates by measuring the scattering parameters $S_{11}$ and $S_{21}$ in a free-space propagation transmitter-receiver setup. The estimation of the complex relative permittivity values

of the concrete blocks is achieved using conversion method named Nicolson-Ross-Weir. In [136], a 3-D printed wide band free-space measurement system is demonstrated. It operates within a wide frequency range of 2 to 18 GHz to evaluate the complex dielectric properties of rigid and flexible materials. The study involved the characterization of four types of commercially available materials: polyimide film, liquid crystalline polymer sheet, ceramic composites, and polypropylene with different thicknesses. The extracted dielectric properties were then compared with experimental parameters for a range of materials to validate the effectiveness of the measurement approach. In [137], the feasibility and effectiveness of a 24 GHz radar microwave system for object detection at varying distance is demonstrated. The results indicate a high level of accuracy, approximately 96.6%, in the classification process. The proposed approach offers a promising solution for efficient and real-time target identification and classification.

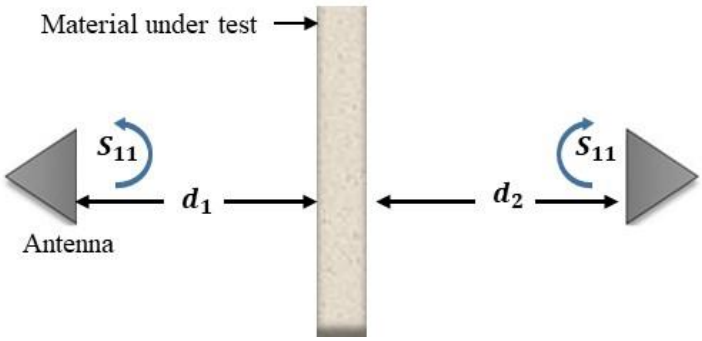


Figure 3.4 Principle of bi-static free-space measurement [17].

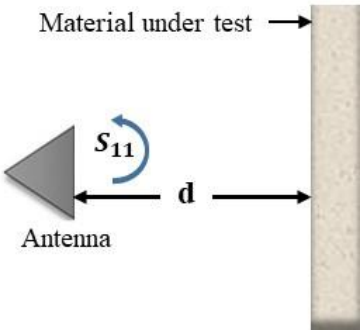


Figure 3.5 Principle of monostatic free-space measurement [17].

In the category of non-resonant methods, the OERW is commonly used for near field applications [83]. This sensor, characterized by its rectangular shape, is used to guide high-frequency electromagnetic waves, provides strong interaction with thick and multi-layered structures [83]-[131]-[138-139]. In OERW-based methods, the MUT is placed against the waveguide, or at a standoff distance between the probe and the MUT [140]. Given the operational principle of the OERW, it is well suited for accurate and real-time inspection across various types of applications. Consequently, significant amount of research and development have been invested in these applications. This includes tasks such as dielectric material characterization [141], delamination evaluation in the layered dielectric structures [142], thickness variation in a stratified composite [143-144] and defect sizing and detection of metal [145]. In [146], the

authors present a rapid and robust technique for assessing the complex permittivity of non-magnetic materials. This method is based on the use of two rectangular waveguides and has demonstrated the ability to yield accurate outcomes. The related system is presented in figure 3.6.

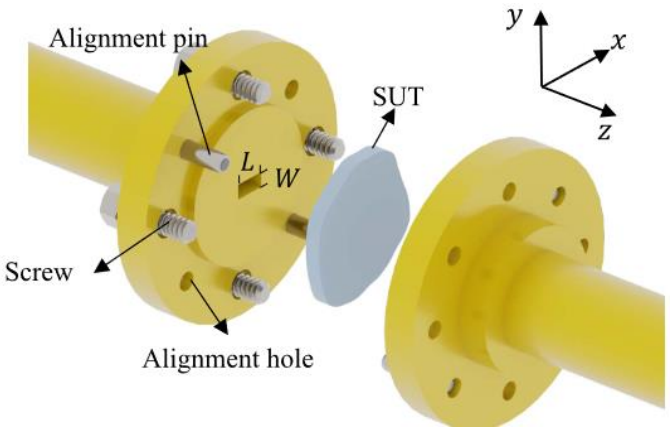


Figure 3.6 Measurement setup using millimeter-wave rectangular waveguides. The MUT is positioned between the two waveguide flanges [139].

In [147], OERW was used for the detection of cracks on substrate under thermal barrier coatings. The system operates in the frequency range 26.5 GHz - 40 GHz. The amplitude and phase-shift of the complex reflection coefficient are employed as to characterize the cracks, through a scanning measurement. In [148], an OERW is used to detect and characterize internal defects in coated glass fiber reinforcement plastic pipes (figure 3.7). The results show that the proposed method can clearly reveal the area and the depths of the defects.

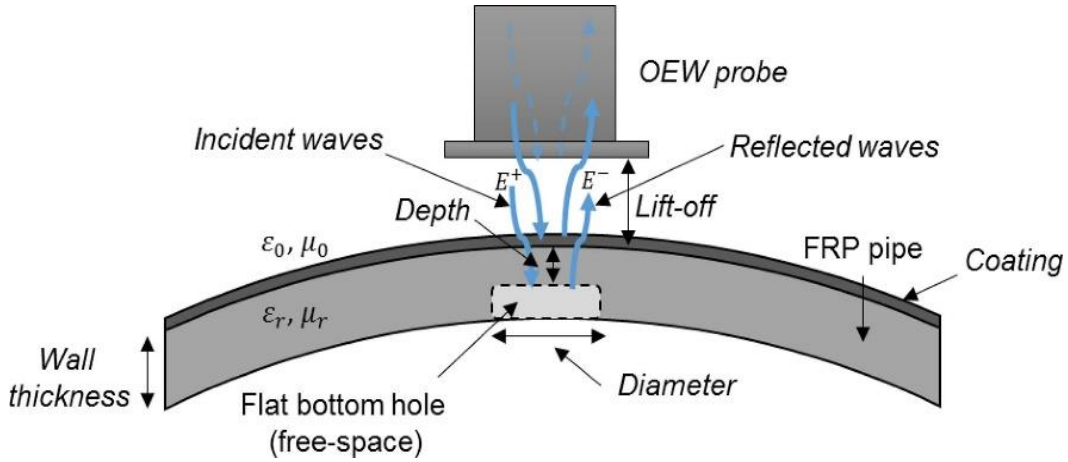


Figure 3.7 Microwave Open-ended Waveguide for glass fiber reinforcement plastic pipe scanning [148].

The table 3.1 presents a comparative study between the two microwave characterization techniques: free-space radar and transmission line.

| | Free-space | Transmission line (Waveguide) |
|---|---|---|
| **Frequency range** | 50 MHz – 330 GHz | 50 MHz – 75 GHz |
| **S-parameters** | $S_{11} - S_{21}$ (reflection / transmission) | $S_{11} - S_{21}$ |
| **MUT** | Moderate to large planar solid / liquid | Small to Moderate planar solid |
| **Measured dielectric properties** | Permeability – permittivity | Permeability – permittivity |
| **Strengths** | • Non-contact<br>• ability to operate in high temperature environments<br>• simple measurement setup<br>• Minimal constraints on sample size and shape | • Accurate characterization<br>• High interaction with thin and multilayered structures<br>• Particularly effective for small samples |
| **Challenges** | Multiple reflections between the sample and the antenna | Limitation of the air gap effects |

Table 3.1 Summary of measurement methods: free-space and waveguide approaches [133]-[149].

## 3.3. Double ridge guide horn antenna

### 3.3.1. Principle of monostatic free-space measurements

A free-space monostatic radar is designed for applications where access to only one side of the target material is possible. In such scenarios, the radar system operates in a monostatic configuration, using a single antenna for both transmitting and receiving electromagnetic signals. In this work, we propose a monostatic free-space system in order to characterize the dielectric MUT in microwave range. Figure 3.8 gives a schematic diagram of the proposed system.

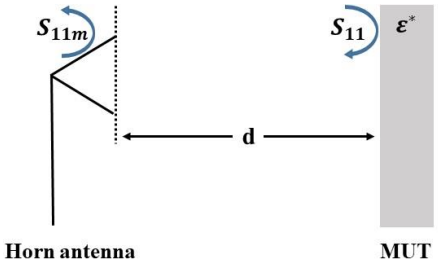


Figure 3.8 Schematic diagram of the free-space monostatic microwave measurement instrumentation with MUT positioned at distance d.

In this setup, the antenna is connected to a Vector Network Analyzer (VNA) to measure the reflection coefficient of the planar (MUT). The measured reflection coefficient $S_{11m}$ is in the reflection coefficient measured by the VNA. To establish a relationship between $S_{11m}$ and the calibrated reflection coefficient $S_{11}$of the MUT located at a reference distance *d*, a calibration procedure is required. Figure 3.9 provides the flow chart of the system calibration process.

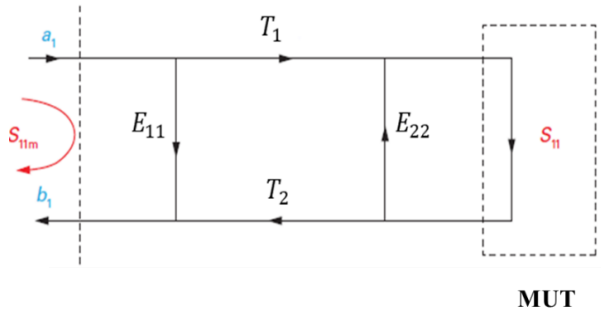


Figure 3.9 Flow chart of the wave propagation between the aperture of the antenna and the MUT.

The material in electromagnetic range can be described as mentioned in the state-of-the-art chapter by its complex permittivity. This permittivity is defined as:

$$\varepsilon^* = \varepsilon' - j\varepsilon'' = \varepsilon_0\varepsilon_r^* = \varepsilon_0\,(\varepsilon_r' - j\varepsilon_r'') \tag{3.4}$$

where $\varepsilon'$is the dielectric constant and $\varepsilon''$ is the loss factor.

In a first approximation, we consider that the microwave response $S_{11}$ of the MUT is mainly attributed to the first wave reflection at the air - material interface. Applying boundary conditions at the air-material interface, it is found that this parameter is related to the permettivity by the following equation [95]:

$$\sqrt{\varepsilon^*} = \frac{1 - S_{11}}{1 + S_{11}} \tag{3.5}$$

The relation between $S_{11}$ and the measured $S_{11m}$ is derived by the flow chart in (3.6) :

$$S_{11} = \frac{S_{11m} - E_{11}}{T_1T_2 + E_{22}(S_{11m} - E_{11})} \tag{3.6}$$

The calibration step consists to determine $E_{11}$, $E_{22}$, and $T_1T_2$, which respectively correspond to directivity, source match and reflection tracking error terms. Specifically, $T_1T_2$ referred to the transmission losses and phase-shift that occur when an electromagnetic wave propagates from the VNA towards the reference plane and vice versa. Once the $S_{11}$of the MUT is known, it enables the determination of the permittivity of the MUT (equation 3.5), and the characterization of its type. In this following, we use a double ridge guide horn antenna operates in the frequency range between 150 KHz and 6 GHz to introduce a MNDT&E of the dielectric MUT.

## 3.3.2. Experimental setup

The proposed instrumentation consists of the double ridge guide horn antenna [SAS-571] (figure 3.10 (a)) associated to the VNA [Anritsu® MS46121B] presented in the figure 3.11(a). The SAS-571 double Ridge Guide Horn Antenna is intended for general laboratory use in a wide variety of industrial and scientific applications. It is lightweight, compact and has been manufactures for broadband response. It has been used as reference antenna, for its good compromise between high bandwidth and directivity for a parametric study. Figure 3.10 provides a detailed representation of the antenna. Table 3.2 presents the characteristics of the double ridge guide horn antenna. Table 3.3 presents the characteristics of the VNA.

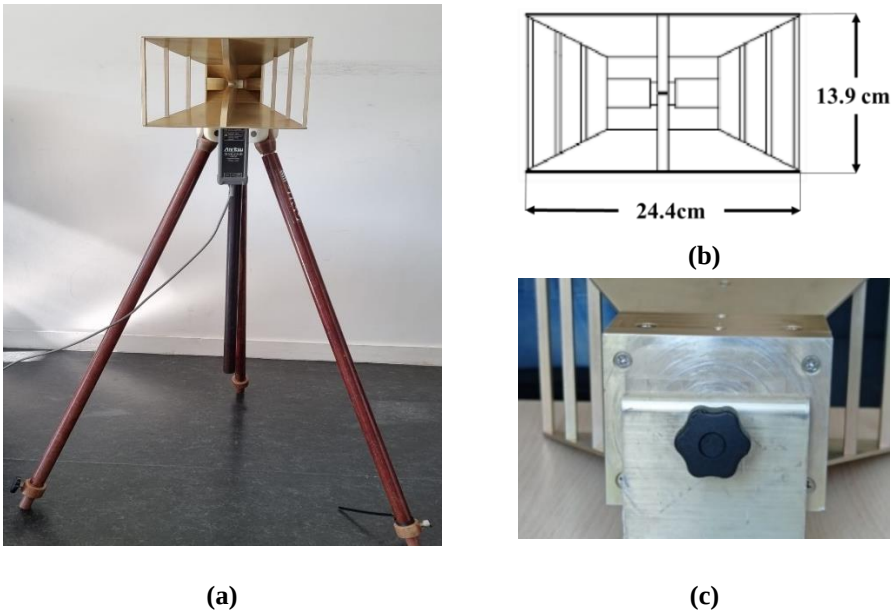


Figure 3.10 Double ridge guide horn antenna [SAS-571]: (a) front view; (b) physical dimensions of the aperture; (c) back view.

| | |
|---|---|
| **Frequency range** | 700 MHz - 18 GHz |
| **Gain** | 1.4 to 15 dBi |
| **Connector** | N-Type, female |
| **Weight** | 1.59 kg |

Table 3.2 Specifications of the double ridge guide horn antenna [SAS-571].

Before starting the measurements, the VNA must be calibrated in order to eliminate the systematic errors and provide quantitative results. Calibration plays an essential role by establishing a reference point at the measurement port and correcting for any known imperfections within the VNA system. A short-open-load (SOL) calibration using the calibration-kit: OSLN50A-8 from Anritsu® (figure 3.11(b)) is applied. The calibration kit features type N(m) connectors and is designed for a frequency range from DC to 8 GHz with a 50 Ω impedance. For more details about the calibration-kit in Appendix B.


(a) (b)

Figure 3.11 (a) Compact 1-port vector network analyzer Anritsu® MS46121B (150 kHz – 6GHz). (b) Calibration-kit Anritsu® (OSLN50A-8).

| | |
|---|---|
| **Frequency range** | 150KHz – 6 GHz |
| **Output power** | – 5 dBm (for frequency from150 kHz to 46 MHz)<br>+ 3 dBm (for frequency from 46 MHz to 4 GHz)<br>– 5 dBm (for frequency from 4 GHz to 6 GHz) |
| **Connecter** | N-type |
| **Power (max)** | 23 dBm |
| **Dimensions** | 52 mm x 148 mm x 36 mm |
| **Weight** | < 0.4 kg |

Table 3.3 VNA (Anritsu® MS46121B) system specifications.

The VNA associated with the antenna attached to a tripod, is employed to measure the reflection coefficient $S_{11}$ of the planar dielectric material. The MUT is positioned on a mechanical displacement system with a step of 500µm, as illustrated in the figure 3.12. The measurement configuration is detailed in the table 3.4. The VNA IFBW is set to 100Hz as compromise between measurement time and measurement accuracy. The measurements are performed in the frequency range between 150 KHz and 6GHz.

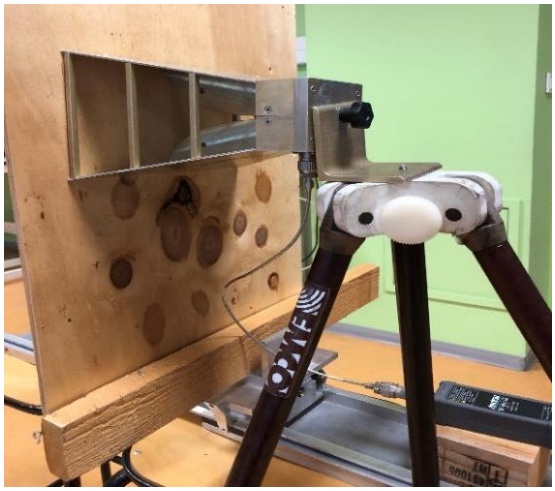

Figure 3.12 Picture of the free-space measurement system with wooden MUT.

The measurement process comprises three distinct steps. In the first step, the reflection coefficients are measured under free-space conditions without the presence of the MUT. This step involves multiple repetitions of measurements to determine the measurement reproducibility, a critical factor that can significantly influence overall performance. Following this, measurements associated to the calibration procedure are performed. Specifically, we measured the reflection coefficient of a planar metal sample (perfectly conductive and reflective free-space material) from contact to 15 cm with step of 1 mm. We repeat the measurements twice to validate the reproducibility of the measurements. In the third step, the MUT replaces the metal sample at the reference plane established during the calibration step. We measure the $S_{11m}$ of the MUTs to extract their permittivity and validate the proposed technique.

| | |
|---|---|
| **Frequency range** | 150 KHz – 6 GHz |
| **Intermediate frequency bandwidth – IFBW (Hz)** | 100 |
| **Number of points** | 201 |

Table 3.4 $S_{11}$ measurement configuration using the double ridge guide horn antenna and the VNA.

The $S_{11}$measurements in free space are performed before starting measurements on the material samples. The resulting measurements are presented in the figure 3.13. The maximum errors in magnitude and phase-shift of the complex reflection coefficient are 0.2 % and 0.0027°, respectively (figure 3.14, 3.15).

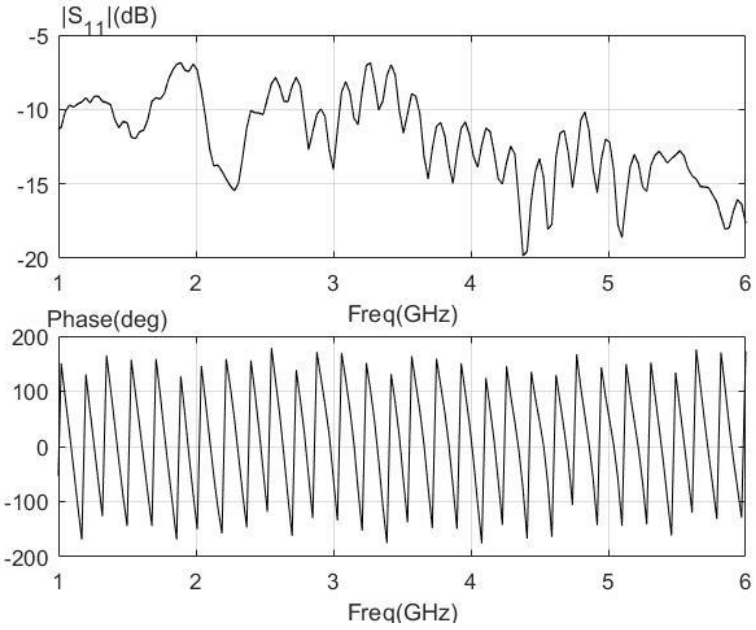


Figure 3.13 Measured $S_{11}$ without MUT in the frequency range from 1 to 6 GHz.

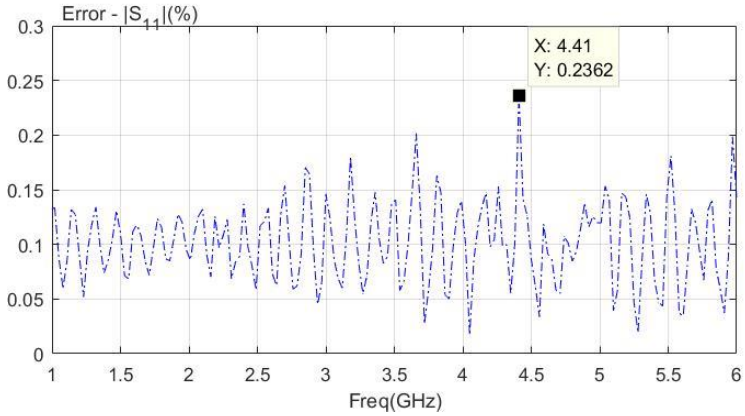


Figure 3.14 Percentage of the relative errors between the multiple measured $S_{11}$of the empty free-space.

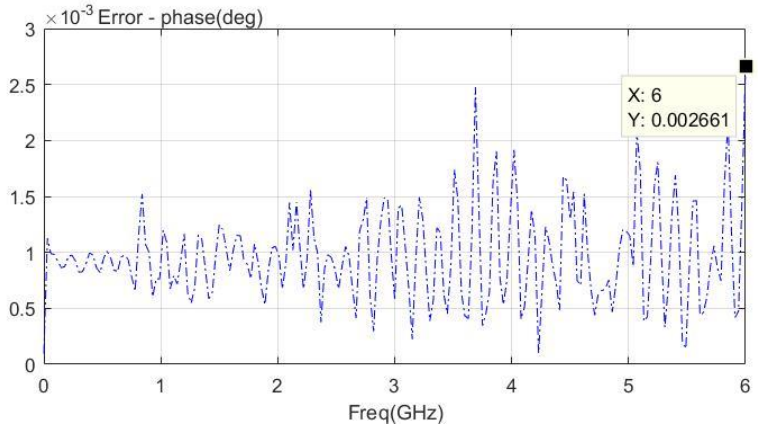


Figure 3.15 The relative errors between the multiple measured $S_{11}$ of the empty free-space.

### 3.3.3. Free-space Calibration procedure

The free-space calibration step consists of determining the three complex terms $E_{11}$,$E_{22}$ and $T_1T_2$. This calibration procedure, inspired by [150], is based on the well-known calibration technique SOL (Short–Open–Load) commonly used in traditional guided microwave measurements. However, this approach introduces a difference by measuring standard material at three distinct known distance separations between the antenna and this standard. In our calibration setup, we use the metal sample as the standard material. The measured complex reflection coefficient $S_{11m}$ can be expressed as a function of the real complex reflection $S_{11}$ of the MUT located at distance *d* from the antenna by:

$$S_{11m} = E_{11} + \frac{T_1T_2S_{11}}{1 - E_{22}S_{11}} \tag{3.7}$$

Where $S_{11} = -e_0^{-2\delta_0\Delta r}$ with $\delta_0$ denotes the free-space propagation constant, $\Delta r$ denotes the stand-off distance between the reference plane and the MUT.

A linear system of three equations is required to determine the three error terms $E_{11}$,$E_{22}$ and $T_1T_2$. Thus, the free-space calibration process consists of the following key steps:

1. **Set the Reference Plane**: Fix the reference plane at a fixed distance *d* and place the metal at this reference point.
2. **Measure** $S_{11m}$: In the presence of the metal, record $S_{11m}$ at three distinct distances: *d, d-1,* and *d+1*.
3. **Calculate** $S_{11}$ **of the Metal**: Calculate the $S_{11}$ parameter of the metal at these three distances using the following equation:

$$S_{11} = -e_0^{-2\delta_0\Delta r} \tag{3.8}$$

with $\Delta r = 0$ at the reference plane, $\delta_0 = j\frac{2\pi}{\lambda_0}$; $\lambda_0 = \frac{c}{F}$.

4. **Solve the System of Equations**: Insert the measured of $S_{11m}$ values and the calculated $S_{11}$ values in the equation (4) and solve the resulting system of three equations with three unknowns to calculate the error terms ($E_{11}$, $E_{22}$, and $T_1T_2$).

## 3.3.4. Results and permittivity characterization

In this following, the operating frequency is set to 6 GHz, wavelength $\lambda = 50mm$. The reference calibration plane is set to $d = 14.9$ cm and then at $d = 10$ cm. We intentionally choose to operate at a relatively short antenna-to-material distance to minimize the diffraction effects at the edges of the sample.

**Case 1: Reference plane for $d = 14.9$cm.**

In case 1, we position the reference plane at $d = 14.9$cm ($d \simeq 3\lambda$), leading to measurements of the metal at distances of 14.8 cm, 14.9 cm, and 15 cm. The standard parameters are detailed in table 3.5. We record three sets of measured $S_{11m}$values (both magnitude and phase-shift) at these distances. Subsequently, we calculate the corresponding $S_{11}$ values using equation (5) with $\Delta r$ = -1, 0, and +1. $S_{11m}$ and $S_{11}$ values are then fed into equation (4) to form a system of three equations. The solution of this system is presented in table 3.6.

| **Standard** | $\Delta r(mm)$ | $S_{11m}(Lin)$ | $S_{11m}(deg)$ | $S_{11}(Lin)$ | $S_{11}(deg)$ |
|---|---|---|---|---|---|
| **Cal 1** | -1 (148) | 0.0801 | -125.6012 | 1 | -165.6 |
| **Cal 2** | 0(149) | 0.0929 | -133.9922 | 1 | -180 |
| **Cal 3** | 1(150) | 0.1042 | -142.781 | 1 | 165.6 |

Table 3.5 Free-space standards parameters used for free-space calibration with reference plane positioned at $d = 14.9cm$; frequency: 6GHz.

| | | | |
|---|---|---|---|
| **Directivity** | $E_{11}$ | $-0.0557 - 0.0008i$ | $-22.25dB; -87.46°$ |
| **Source match** | $E_{22}$ | $-0.0981 - 0.0735i$ | $-20.41dB; -141.51°$ |
| **Reflection tracking** | $T_1T_2$ | $0.0128 + 0.0589i$ | $-16.73dB; 77.13°$ |

Table 3.6 Complex error terms determined from the free-space calibration procedure at $d = 14.9cm$; frequency: 6 GHz.

Figure 3.16 presents the measured and modelled $S_{11m}$ of the metal as function of the distance ranging from 145 to 150 mm ($\Delta r = -41mm$) . The measured and modeled values show close similarity near the reference plane ($\Delta r = 0$), but they begin to diverge as the distance from the reference plane increases. It is essential to note that when the antenna operates in close proximity to the sample, the spherical nature of propagation waves results in amplitude variations in these

waves function of the distance traveled. Consequently, this calibration procedure provides accurate data only if the calibration standards are close to the material reference plane.

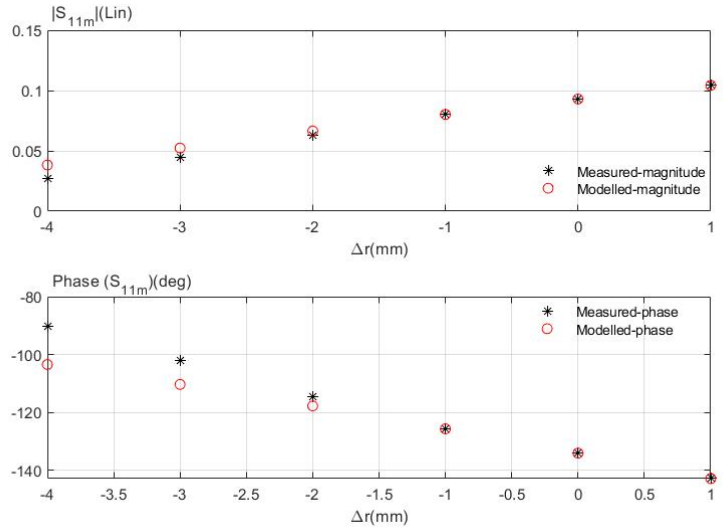


Figure 3.16 Comparison between modelled and measured $S_{11m}$ as a function of $\Delta r$ with reference plane placed at $d = 14.9cm$– frequency: 6 GHz.

Figure 3.17 shows the measured and modelled $S_{11}$of the metal as function of the distance ranging from 145 to 150 mm ($\Delta r = -41mm$). The expected magnitude of $S_{11}$for a metal is 1 ($and\ phase = -\Pi$), as it reflects all incoming electromagnetic waves emitted by the antenna. We can see that the amplitude of the measured $S_{11}$ for the metal closely approaches unity in the proximity of the measurement reference plane ($\Delta r = 0$). As previously explained, this occurs because we are conducting measurements within the antenna's near-field region, where measurements are affected by the spherical nature of the waves.

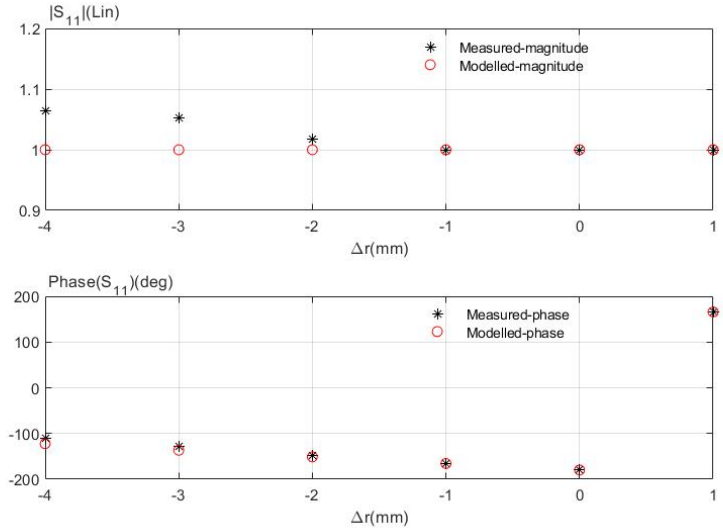


Figure 3.17 Comparison between modelled and measured $S_{11}$ as a function of $\Delta r$ with reference plane placed at $d = 14.9cm$– frequency: 6 GHz.

**Case2: Reference plane for d=10 cm.**

With the reference plane fixed at a distance of $d = 10$ cm ($d = 2\lambda$), we record three sets of measured $S_{11m}$ values, including both magnitude and phase, at distances 9.9 cm, 10 cm, and 10.1 cm. Following this, we compute the corresponding $S_{11}$values using equation (5) with $\Delta r$ = -1, 0, and +1. These $S_{11m}$ and $S_{11}$ values, shown in table 3.7, are subsequently used in equation (4) to form a system comprising three equations. The resolution of this system is detailed in the table 3.8.

| **Standard** | $\Delta r(mm)$ | $S_{11m}(Lin)$ | $S_{11m}(deg)$ | $S_{11}(Lin)$ | $S_{11}(deg)$ |
|---|---|---|---|---|---|
| **Cal 1** | -1 (99) | 0.1055 | -122.741 | 1 | -165.6 |
| **Cal 2** | 0(100) | 0.1170 | -136.39 | 1 | -180 |
| **Cal 3** | 1(101) | 0.1236 | -144.196 | 1 | 165.6 |

Table 3.7 Free-space standards parameters used for free-space calibration with reference plane positioned at d=10 cm; frequency – 6 GHz.

| | | | |
|---|---|---|---|
| **Directivity** | $E_{11}$ | $-0.1104 - 0.0201i$ | $-20.36dB; -172.64°$ |
| **Source match** | $E_{22}$ | $-0.4814 + 0.5510i$ | $-2.27dB; 131.38°$ |
| **Reflection tracking** | $T_1T_2$ | $-0.0467 + 0.0173i$ | $-26.92dB; 158.22°$ |

Table 3.8 Complex error terms determined from the free-space calibration procedure at $d = 10cm$; frequency: 6 GHz.

For the reference plane placed at d=10 cm, the impact of diffraction effects at the edges of the MUT decreases. The calibration procedure provides more precise and reliable data. In contrast, calibrating at 14.9 cm places the reference farther from the antenna, increasing the potential for diffraction-related errors ($T_1T_2 \vee 0.0495$at distance 10 cm is less than $T_1T_2 \vee 0.06029$ at distance 14.9 cm).

Figure 3.18 presents the measured and modelled $S_{11m}$ as function of the distances ranging from 96 to 104 mm ($\Delta r = -44mm$). We observe a close correspondence between the measured and modeled $S_{11m}$ values for distances exceeding 100 mm (the metal is very thin).

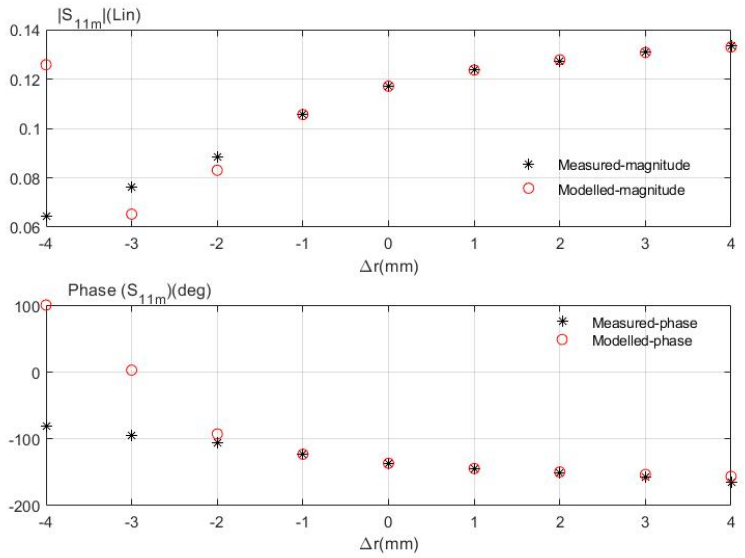


Figure 3.18 Comparison between modelled and measured $S_{11m}$ as a function of $\Delta r$ with reference plane placed at $d = 10cm$– frequency: 6 GHz.

Figure 3.19 presents the measured and modelled $S_{11}$ as function of the distances ranging from 96 to 104 mm ($\Delta r = -44mm$). We can see that the amplitude of the measured $S_{11}$ for the metal closely approaches unity in the proximity of the measurement reference plane and still very close to one in the more far distances, the reference at 10 cm lead to better modeling. After calibration $S_{11}$, the modeled phase-shift demonstrates the expected linear behavior.

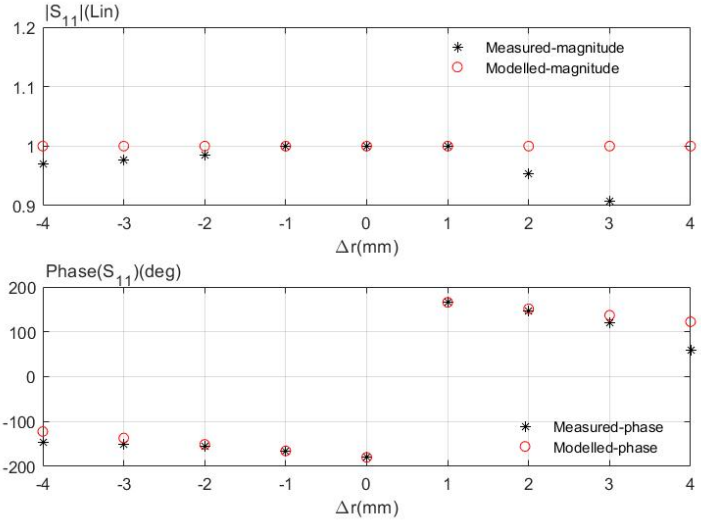


Figure 3.19 Comparison between modelled and measured $S_{11}$ as a function of $\Delta r$ with reference plane placed at $d = 10$cm - frequency: 6 GHz.

Following the modeling and calibration of the system, we place the wooden MUT at the designated reference plane. Subsequently, we measure the reflection coefficient $S_{11m}$ for this MUT. Figure 3.20 and 3.21, present the measured $S_{11m}$ of wood and metal, magnitude and phase-shift, at distances 14.9 cm and 10 cm respectively.

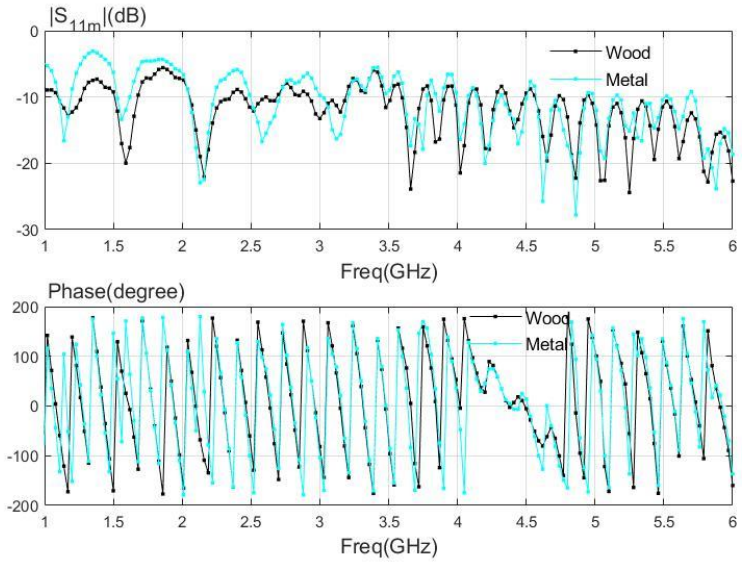


Figure 3.20 Measured reflection coefficient $S_{11m}$ of the wood and metal MUT as function of frequency ranging from 1 to 6 GHz; *d*=10 cm.

It is important to note that each material has a unique signature, confirming the effectiveness of the microwave system in characterizing materials. We applied equation (3) with the measured $S_{11m}$ at frequency 6 GHz to deduce the calibrated $S_{11}$. Subsequently, we employed equation (2) to calculate the permittivity of the MUT based on the measured $S_{11}$ values in the reference plane of the MUT.

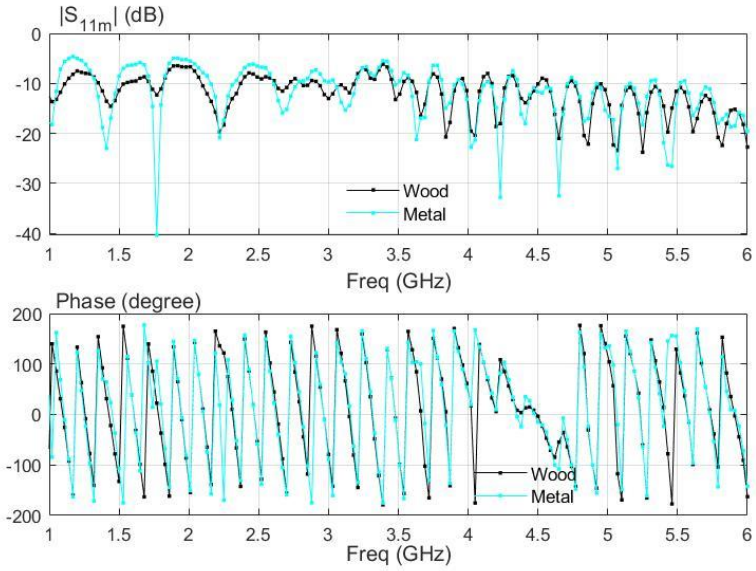


Figure 3.21 Measured reflection coefficient $S_{11m}$ of the wood and metal MUT as function of frequency ranging from 1 to 6 GHz; *d*=14.9 cm.

In the table 3.9, we present a comparison between our permittivity results and those reported in the literature [151-153]. It is important to note that the complex permittivity of dry wood at a specific frequency can exhibit variability due to factors such as wood type, moisture content, temperature, and other environmental conditions. Consequently, these values should be

considered approximate, and the actual values may differ based on the specific wood sample and measurement conditions. Our findings fall within the range documented in the existing literature.

| **Permittivity** | $\varepsilon'$ | $\varepsilon''$ |
|---|---|---|
| **Literature (F/m)** | 1.2 - 4.5 | 0.01 - 0.6 |
| **Reference plane 10 cm (F/m)** | 1.2325 | 0.6154 |
| **Reference plane 14.9 cm (F/m)** | 2.0396 | 0.6964 |

Table 3.9 Extracted complex permittivity of wooden MUT at two reference plans: *d* = 10 cm and *d* =14.9 cm; frequency is set to 6GHz.

# 3.4. Simple horn antenna

## 3.4.1. Experimental Setup

In this section, we introduce an alternative technique for MNDT&E material characterization purposes. Our proposed approach relies on the use of a simple and compact horn antenna [from ATM®: Advanced Technical Materials, P/N 187-251-6] as depicted in figure 3.22, in conjunction with the VNA from [Anritsu® MS46121B]. The reason for choosing this specific horn antenna is based on its compact design, which facilitates its integration onto a robot platform. Furthermore, preliminary to measurements, we performed 3D electromagnetic simulations in CST Microwave Studio to predict the microwave response. The simplicity of the antenna structure is better suited for designing the structure. As a result, all subsequent research studies within this thesis rely on this antenna for conducting measurements and performing analytical assessments. Table 3.10 presents the specifications of the horn antenna.

Prior to conducting any measurements, it is mandatory to ensure the VNA's accuracy, and this is achieved through a calibration process using the same calibration-kit from Anritsu® (OSLN50A-8). Following VNA's calibration, the antenna is connected to the input port of the VNA using N-to-SMA coaxial transition and SMA-to-waveguide transition. No coaxial cable is considered to minimize random errors commonly attributed to cable movement during measurements.

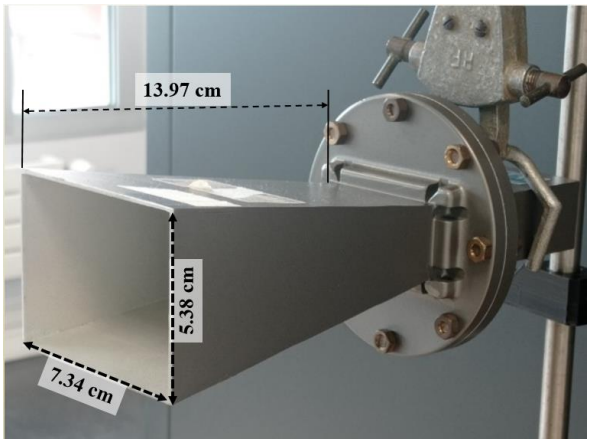

Figure 3.22 Horn antenna ATM® (P/N 187-251-6).

| | |
|---|---|
| **Frequency range** | 3.95 GHz – 5.85 GHz |
| **Gain** | 10 dB nominal |
| **Connector** | SMA -Type |

Table 3.10 Specifications of the double ridge guide horn antenna ATM® (P/N 187-251-6).

For precise positioning and control, both the measurement instruments (antenna and VNA) and the MUT are situated within the same mechanical displacement system in section 1, with a step size of 500 µm, as depicted in figure 3.23. This setup ensures that the MUT can be systematically and accurately analyzed during the experimentation.

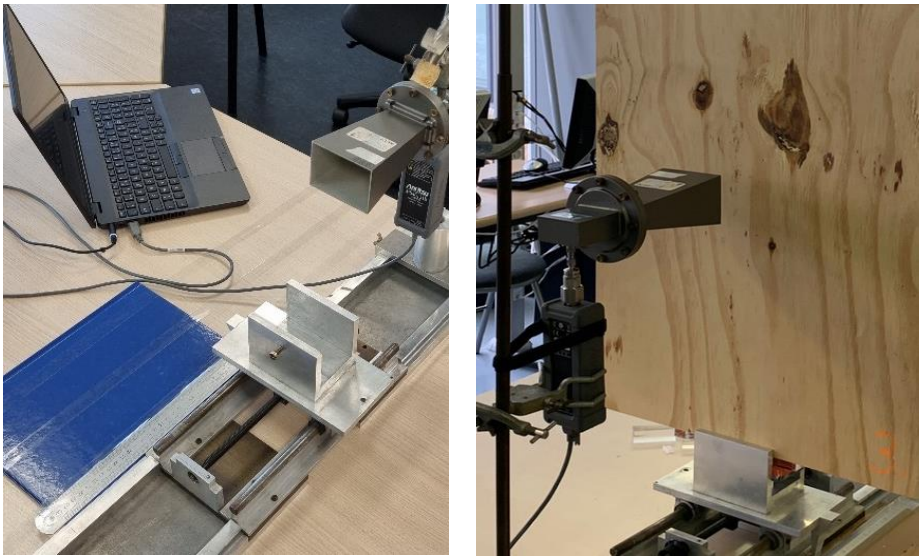

(a) (b)

Figure 3.23 Measurements system (a) without MUT (b) Wood MUT.

The measurements are conducted within the frequency range covered by the antenna, between 3.95 to 5.85 GHz, with the measurement configuration outlined in table 3.11.

| | |
|---|---|
| **Frequency range** | 3.95 - 5.85 GHz |
| **IFBW (Hz)** | 100 |
| **Number of points** | 863 |

Table 3.11 $S_{11}$ measurement configuration using the horn antenna and the VNA.

The VNA associated with the antenna is used to measure the reflection coefficient of the planar dielectric material. Specifically, the measured reflection coefficient, $S_{11m}$, is determined at the antenna's aperture. To establish the relationship between $S_{11m}$ and the real material's reflection coefficient $S_{11}$ the same free-space calibration procedure, explained in section 1, is applied. This measurement process consists of three successive steps:

(1) Initially, multiple measurements of the reflection coefficient are taken without MUT to ensure the reproducibility of the measurements.
(2) Subsequently, measurements related to the calibration procedure are conducted. The reference plane is positioned at a distance $d = 14.9$cm from the antenna.
(3) Finally, measurements of the MUT's reflection coefficient, which is the primary focus of characterization, are executed.

## 3.4.2. Results and permittivity characterization

The $S_{11}$measurements in free space are performed before starting measurements on the material samples. The resulting measurements are presented in the figure 3.24.

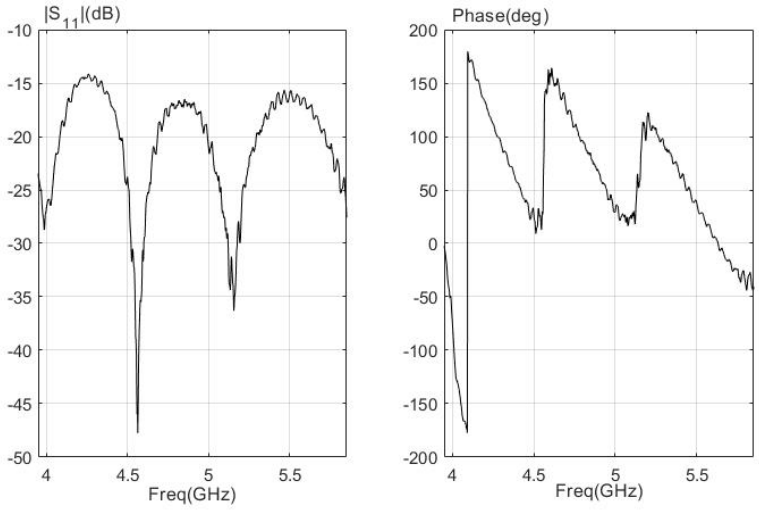


Figure 3.24 Free-space $S_{11}$ measurements without MUT.

For the free-space calibration procedure, the operating frequency is set to 5 GHz. The reference calibration plane is set to $d = 14.9$ cm. We record three sets of measured $S_{11m}$ values (magnitude and phase-shift) at distances of 14.8 cm, 14.9 cm, and 15 cm. Subsequently, we calculate the corresponding $S_{11}$ values using equation (5) with $\Delta r$ = -1, 0, and +1. This results in a system of three unknowns, and we calculate the error terms.

Figure 3.25 shows the measured and modelled $S_{11m}$of the metal as function of the distances ranging from 142 to 150 mm ($\Delta r = -71mm$). $S_{11}$of a metal is theoretically -1, otherwise in the figure 3.26 it is shown that $S_{11m}$ is between 0 and 0.5. The measured and modeled values show close similarity near the reference plane ($\Delta r = 0$).

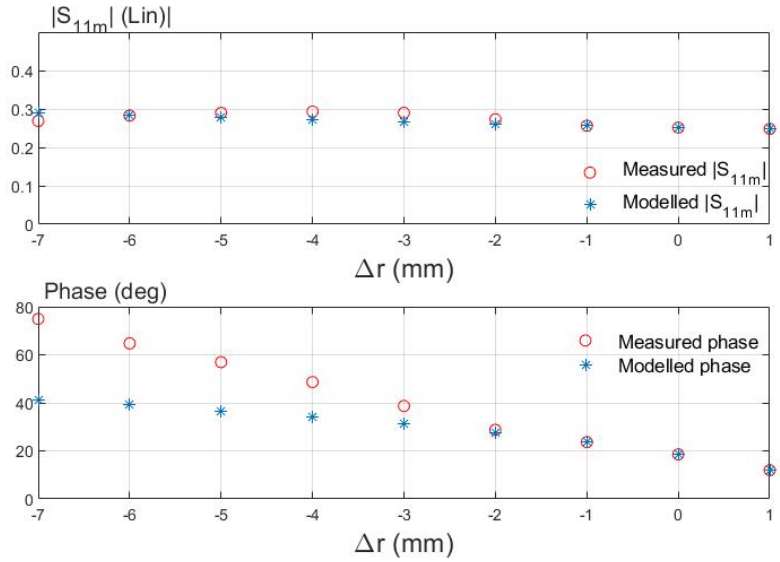


Figure 3.25 Comparison between modelled and measured reflection coefficient $S_{11m}$ as a function of the stand-off distance Δr from the reference plane (d =14.9 cm) – frequency: 5 GHz.

Figure 3.26 shows the measured and modelled $S_{11}$of the metal as function of the distance ranging from 142 to 150 mm ($\Delta r = -71mm$). The expected magnitude of $S_{11}$for a metal is 1, as it reflects all incoming electromagnetic waves emitted by the antenna. We can see that the amplitude of the measured $S_{11}$ for the metal closely approaches unity in the proximity of the measurement reference plane $\Delta r = 0$, but they begin to diverge as the distance from the reference plane increases. As previously explained, this occurs because we are conducting measurements within the antenna's near-field region, where measurements are affected by the spherical nature of the waves.

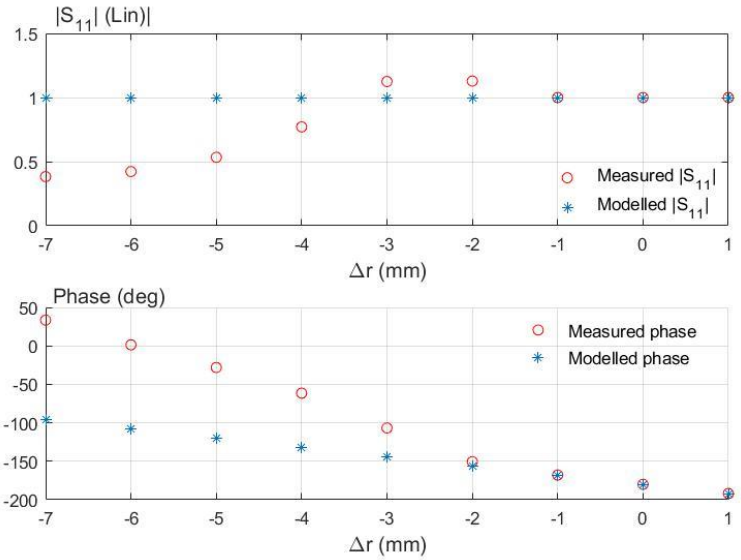


Figure 3.26 Comparison between modelled and measured reflection coefficient $S_{11}$ as a function of the stand-off distance Δr from the reference plane (d=14.9 cm) – frequency: 5 GHz.

After the free-space calibration procedure, measurements of the wooden MUT are performed. We position the MUT at the reference plane, $d = 14.9$cm, and measure the $S_{11m}$. We use equation (3) to determine its $S_{11}$, subsequently deriving its permittivity based on the equation (2).

Figure 3.27 presents the measured $S_{11m}$ of the metal and the wooden MUT. We use the same MUTs as discussed in section 1. From the measured $S_{11m}$values, we calculate $S_{11}$and, consequently, determine the permittivity of the wooden MUT.

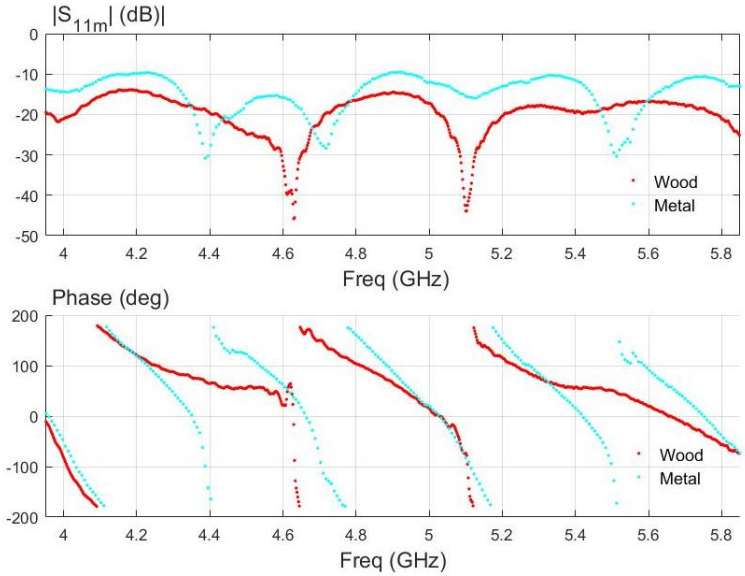


Figure 3.27 Measured $S_{11m}$ of wood and metal in the frequency range 3.95 - 5.85 GHz.

We applied equation (3) with the measured $S_{11m}$ to deduce the measured $S_{11}$. Subsequently, we employed equation (2) to calculate the permittivity of the MUT based on the measured $S_{11}$values. The results are shown in the table 3.12.

| **Permittivity** | $\varepsilon'$ | $\varepsilon''$ |
|---|---|---|
| **Wood** | 1.445 | 0.621 |

Table 3.12 Extracted complex permittivity; reference plane 14.9 cm; frequency=5 GHz.

The complex permittivity of dry wood in the microwave range can vary depending on several factors, including the type of wood, its moisture content.

## 3.5. Discussion

Analytical modeling for the determination of the complex permittivity often encounters limitations due to various factors, such as the material thickness, frequency dependency, distance between the material and the antenna and the **simplifying assumptions, etc.** These limitations can significantly affect the accuracy of the extracted permittivity values. In this study, we assumed that the material was very thin, focusing on the analysis of the reflection coefficient at the surface of the material, while neglecting the absorption of electromagnetic waves by the material. This simplification introduces inaccuracies into the modeling process. On the other hand, accounting for absorption effects can result in a more complex modeling approach. Moreover, as materials become more complex in terms of composition or geometry, analytical models become to increasingly challenging develop and may fail to provide accurate results. This underscores the need for alternative approaches. In this regard, ML and DL models offer a promising solution to overcome these limitations. By training on a diverse set of data, ML and DL models can characterize materials with high precision, regardless of their thickness or distance between the reference plane and the antenna. These models learn complex patterns and relationships within the data, allowing for more accurate and versatile characterization of materials. Consequently, the integration of ML and DL approaches in material characterization can lead to more comprehensive and accurate results, particularly when dealing with complex or non-standard material configurations.

## 3.6. Conclusion

In this chapter, we presented two MNDT&E techniques tailored for material characterization, employing two distinct antennas. These antennas play a central role in measuring the reflection coefficient of the MUT. Furthermore, we provided a detailed description of a free-space calibration procedure specifically used to establish the relationship between the materials' permittivity and the measured reflection coefficient. To validate the efficiency of these methodologies, we conducted practical experiments using two wooden MUT samples, and subsequently, we compared our findings with previously documented results in the literature.

In the next chapter, we present three ‘intelligent’ MNDT&E techniques for material characterization and defects detection. These techniques rely on using two microwave instruments: the simple and compact horn antenna featured in the second section and a rectangular open-ended waveguide. ML and DL approaches are used to perform the analysis of the measured reflection coefficients, promising enhanced capabilities for material characterization and defects detection.

# Chapter 4. AI-based microwave techniques for material characterization and defects detection

## Chapter outlines

## 4.1. Introduction

In the previous chapter, we discussed the use of conventional microwave instrumentation along with calibration method for material characterization (e.g. material's permittivity determination). However, these methods have limitations related to factors such as environmental noise, the thickness of the MUT, and the distance between the radar and the MUT. To address these limitations, this chapter propose three '**intelligent' MNDT&E** techniques for materials characterization. This strategy involves integrating microwave techniques with ML and DL models to analyze the microwave response. This combination enables automated, accurate and fast material inspection even when dealing with complex scenarios involving multiple material types and thicknesses. Moreover, this advancement presents advantages such as reducing the dependency on the operators skills and experience, reducing the dependency on complex conversion methods, and potentially enhancing the sensitivity of material characterization and defects detection [1-2].

The proposed techniques are based on two microwave characterization instruments: monostatic free-space radar and an OERW. Our objective is to develop a compact, low-power, fast instrument for classifying and evaluating the materials sensed by microwaves, thus eliminating the need for quantitative extraction of the material's complex permittivity. These approaches coupled with ML and DL models, are employed and validated within two distinct environmental settings: controlled laboratory conditions and more challenging real-world noisy conditions. Using these measurement systems yields accurate results when evaluating materials in both scenarios.

The coding of ML and DL algorithms is carried out in Python, harnessing the capabilities of its rich libraries and frameworks. For preprocessing tasks and data visualization, MATLAB is employed.

The remaining sections are organized as follows. The first section provides a dedicated overview, starting with the foundational concepts of ML and DL models used in this chapter. Following this, the state-of-the-art discussion introduces the MNDT&E technique coupled with ML and DL models for free-space material characterization. The second section introduces the first MNDT&E technique, using monostatic free-space radar with ML models for material characterization. In the subsequent section, another MNDT&E technique is introduced, employing an OERW combined with ML models for contact material characterization. The third part details a distinct MNDT&E technique, integrating an OERW with a 1D-CNN model for defect detection within materials. Finally, the chapter concludes by summarizing the findings and discussing the practical implications of these techniques.

## 4.2. Machine learning fundamentals

In this section, we provide a general overview of the fundamental concepts of Artificial Intelligence (AI), focusing on models used in this work. The aim is to present a basic

understanding and highlight key concepts essential for the rest of the thesis. For more comprehensive understanding of machine learning (ML) and deep learning (DL) models, readers are directed to [154-155].

### 4.2.1. Artificial intelligence

Artificial intelligence (AI) is a field of computer science dedicated to the construction of intelligent programs and machines capable of thinking like humans. This includes the ability to learn, solve problems, understand natural language, recognize patterns, and make decisions. AI comprises a wide range of techniques, including ML, DL, computer vision, all with the objective of developing systems that can autonomously perform intelligent actions and improve their performance over time.

**ML** is a subset of AI that involves the use of algorithms and statistical models to enable computers to learn from and improve their performance on a specific task without being explicitly programmed. The essence of ML lies in the ability of the system to recognize patterns and make decisions based on data. ML has wide-ranging applications, including natural language processing [156], image recognition [157], medical applications [158-161], material characterization and defects detection [162-165] and many more [166-168]. It continues to be a rapidly evolving field with significant potential to change the face of various industries and improve decision-making processes. In a typical ML process, the system is fed with a large amount of data, and it uses this data to identify patterns, relationships, and trends. As the system processes more data, it adjusts its algorithms and models to improve its accuracy and performance on the task at hand. There are three main types of ML, including supervised learning, unsupervised learning, and reinforcement learning (figure 4.1).

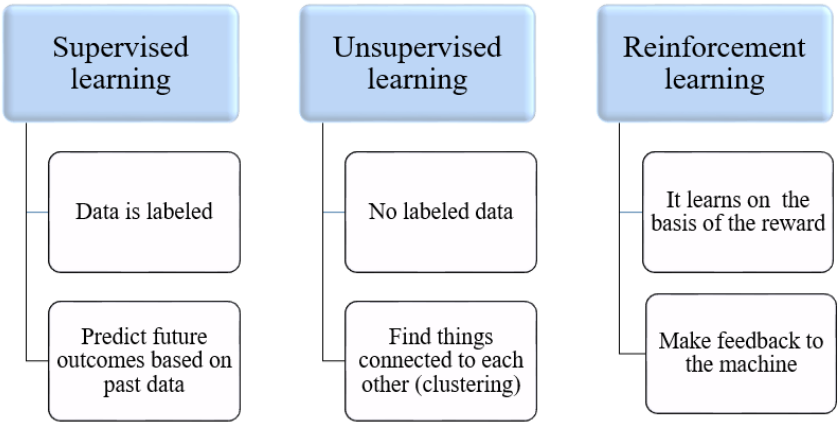

Figure 4.1 Characteristics of supervised, unsupervised and reinforcement learning.

In **supervised learning** (SL), the dataset is commonly divided into two distinct subsets as described in figure 4.2: a non-testing subset comprising both training and validation subsets, and a testing subset [169]. In the training phase, the system learns from labeled data and selects a subset of features. Throughout this phase, the model adjusts its parameters based on the input data and corresponding labels [170]. While, in the testing phase, the trained model aims to make predictions on new, unseen data (testing subset). Once the testing phase is complete and based on its results, the most optimal classification model is selected. This model is then utilized during the

application phase, where it gains the ability to classify and assign classes to previously unseen new data. SL can be categorized in Classification problem (for discrete output, such as binary or labeled predictions, e.g., determining the MUT is wood or glass) and Regression problem (for continuous output, e.g., predicting the permittivity of new MUT). This type of learning includes a wide range of ML models, like logistic regression, decision trees (DCT), as well as more advanced models such as random forests (RF), K-nearest neighbors, support vector machines (SVM), and even deep learning (DL) models [169].

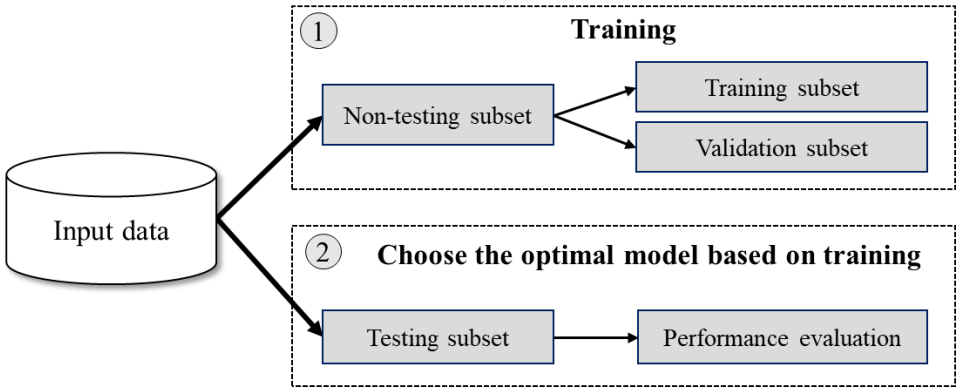


Figure 4.2 Supervised learning: data splitting and performance evaluation.

In **Unsupervised learning**, the model is trained on unlabeled data, meaning there are no corresponding output labels or target values provided during the training process [171]. The primary objective of unsupervised learning is to identify patterns, structures, or relationships within the data without any explicit guidance or pre-defined categories (e.g., analyzing the $S_{11}$ data obtained from various measurements without labeling them, and identify groups of similar reflection patterns). Unsupervised learning finds its primary applications in Clustering, generative models, anomaly detection, and Dimensionality Reduction. Some examples of unsupervised models include K-means and principal component analysis (PCA).

**Reinforcement learning** involves training the system to make decisions in an environment by receiving feedback and rewards for its actions. It is applied in various domains, with one of its notable applications being in board and video games [172].

In the following, our attention is directed towards the methodologies implemented within this study. First, we start by presenting the used conventional SL techniques: SVM, DCT and RF. Then, the well-known dimensionality reduction method: PCA is presented. Following this, we provide an overview of DL principles and introduce the one-dimensional Convolutional Neural Network (1D-CNN) model that will be further used in this work. Lastly, we conclude by presenting the performance metrics employed in this study to evaluate the used classifiers and determine the optimal choice.

### 4.2.2. Support vector machine

The SVM is a powerful and widely used SL algorithm that has demonstrated exceptional performance in various classification and regression tasks [173]. The fundamental idea behind

SVM is to find the optimal hyperplane that best separates different classes in the feature space, while maximizing the margin between them. This hyperplane serves as the decision boundary, allowing SVM to efficiently classify new, unseen data points. SVM can handle linearly separable as well as non-linearly separable data by using kernel functions. These kernels implicitly map the data into a higher-dimensional space, enabling feasible separation. Some common types of kernels used in SVM include linear kernel (figure 4.3), radial basis kernel (RBF) and polynomial kernel (figure 4.4).

Its ability to handle high-dimensional data and its robustness against overfitting make SVM a versatile tool in a wide range of applications, including material characterization [174], remote sensing [175] and medical diagnosis [176].

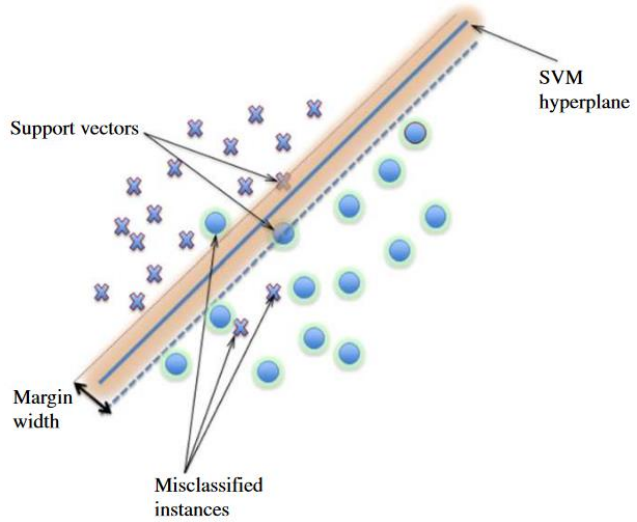


Figure 4.3 Linear SVM classification example [177].

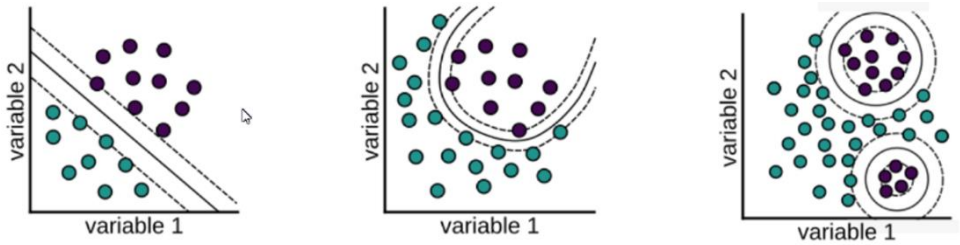


*(a) Linear* *(b) 2nd order Polynomial* *(c) Radial basis*

Figure 4.4 Examples of SVM kernel functions [178].

## 4.2.3. Random forest

The RF and DCT are two widely used ML algorithms that excel in various classification and regression tasks [179]. DCT, described in figure 4.5, is a simple and interpretable model that recursively partitions the data based on the features, creating a tree-like structure of decision nodes and leaf nodes. Each decision node represents a split based on a feature, and each leaf node corresponds to a class or predicted value. While DCT is prone to overfitting on complex datasets, RF addresses this issue by constructing an ensemble of multiple decision trees and combining their predictions (figure 4.6). By averaging or voting on the outputs of individual trees, RF improves generalization and robustness, reducing the risk of overfitting. Moreover, RF takes

advantage of training each tree on a randomly sampled subset of the data, further enhancing the model's performance.

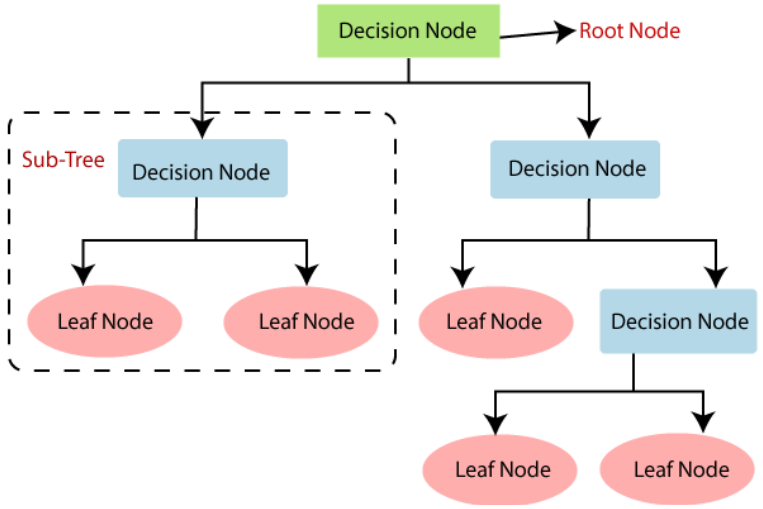


Figure 4.5 Schematic of decision tree algorithm.

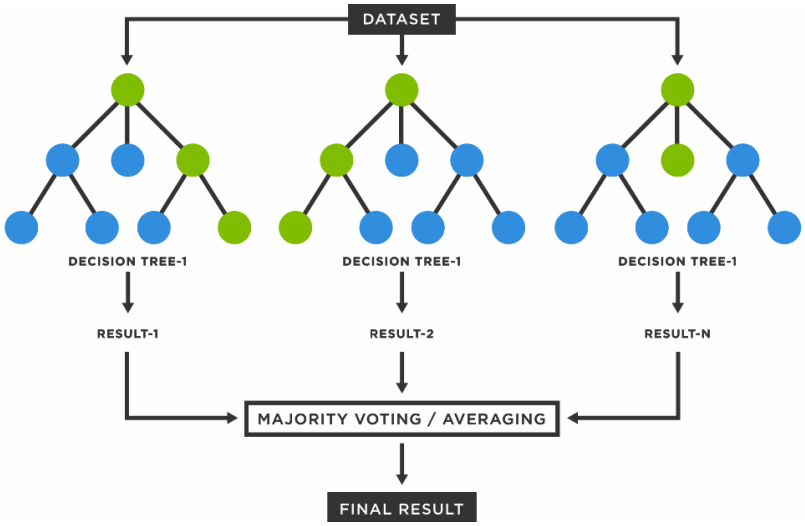


Figure 4.6 Schematic of random forest algorithm.

## 4.2.4. Principal component analysis

The PCA is the most popular dimensionality reduction technique widely used in various fields of data analysis and ML [121]. The primary goal of PCA is to transform a high-dimensional dataset into a lower-dimensional space while preserving its most important features. It achieves this by identifying the principal components, which are orthogonal vectors that represent the directions of maximum variance in the data. These principal components capture the most significant information in the original data, allowing to discard the less relevant features. In order to capture 100% of the data variability, all principal components would be required. However, by using just the first k principal components, which represent at least 70% of the data

variance, we achieve dimensionality reduction while preserving essential information for prediction tasks [180]. By reducing the dimensionality of the data, PCA not only simplifies the computational complexity but also helps in data visualization and interpretation. Figure 4.7 displays the data in its original space and demonstrates its projection based on the first two PCA components, specifically denoted as PCA 1 and PCA 2.

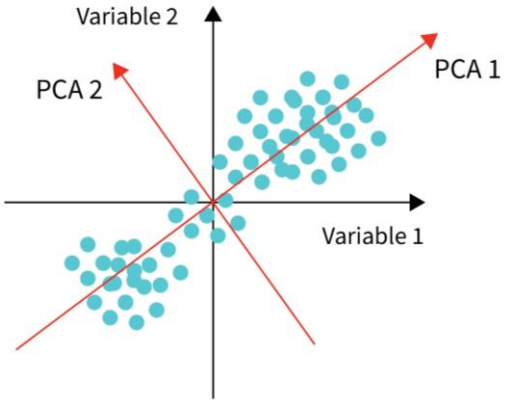


Figure 4.7 PCA illustration. PCA1, representing the first principal component, captures the highest variance in the data. PCA2, the second component, accounts for the next highest variance while being orthogonal to PCA1.

### 4.2.5. Deep learning

Deep Learning (DL), inspired by the structure and functioning of the human brain, constitutes a subset of ML [154]. DL has gained significant dominance in recent years due to its exceptional capabilities in handling complex and large datasets, in addition to its ability to automatically learn features from input data. It consists of multiple nonlinear processing units organized in input, several hidden and an output layers (figure 4.8). The term ‘deep’ refers to the number of layers in the network—the more layers, the deeper the network. The layers are interconnected via nodes, or neurons, with each hidden layer using the output of the previous layer as its input. As the neural network goes deeper, it can progressively extract more abstract and high-level features, enabling the model to understand and recognize complex patterns that would be challenging for traditional ML methods. However, despite its remarkable success, DL also presents challenges, such as the need for large amounts of labeled data, potential overfitting, and computational complexity [181]. In the table 4.1, we provide a comparison between DL and ML.

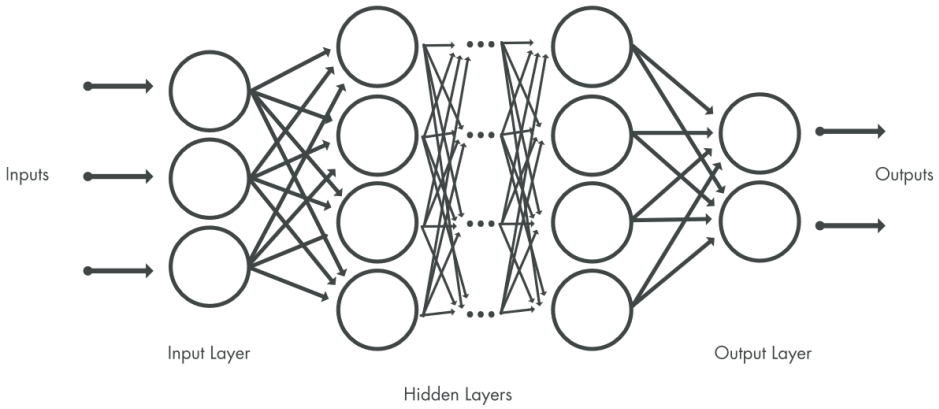


Figure 4.8 Deep neural network architecture [182].

| Machine learning | Deep learning |
|---|---|
| Typically employs simple models | Uses complex neural networks with multiple layers |
| Requires manual feature extraction | Automatically extract feature from input data |
| Well-suited for small dataset | Performs well with large dataset |
| Requires less computational power and time | Requires significant computational resources and time |

Table 4.1 Summary of the main differences between ML and DL.

In 1957, Frank Rosenblatt created the perceptron, the first prototype of what we now know as a neural network [183]. This early development created the basis for complex neural networks that have evolved over the years. In the field of DL various models have been emerged, such as deep feedforward networks, convolutional neural networks, recurrent neural networks, generative adversarial networks, recursive neural networks, deep belief network, etc. [181]. Each with distinct characteristics and applications [184]. In the context of this thesis, our focus goes toward the Convolutional Neural Network (CNN) model.

## a. Convolutional Neural Network

CNN stands as one of the most widely used algorithms for DL with images and videos. Its key strength lies in integrating the feature extraction and feature classification processes into one learning framework (figure 4.9). CNN can extract automatically the 'learned' features from the input data. The network then learns to detect low-level features like edges and corners in early layers and progressively builds up to more complex and abstract features in deeper layers (figure 4.10). This advantage plays a pivotal role in improving classification performance, making CNN particularly attractive for complicated engineering applications.

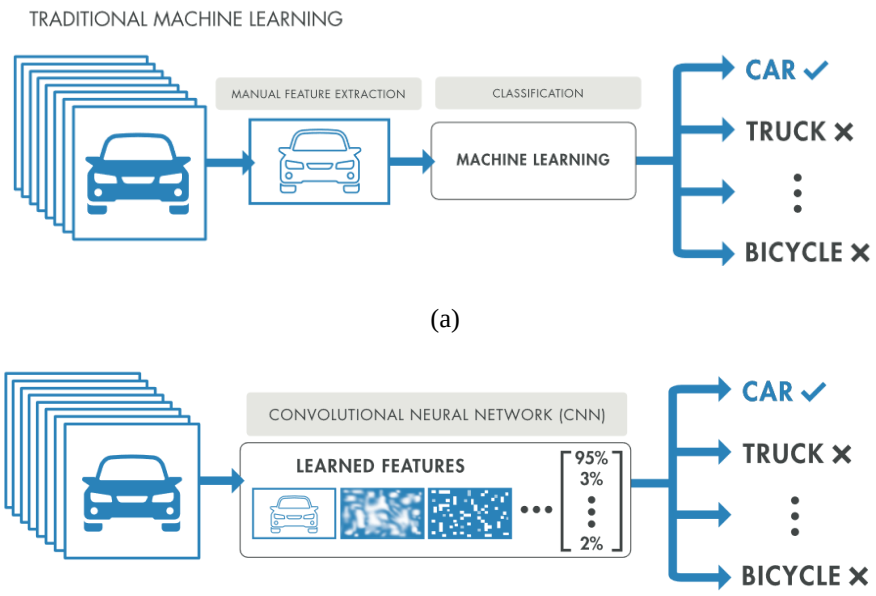


Figure 4.9 Illustrative Scheme of : (a) traditional machine learning models ; (b) CNN: The Network takes an image as input, progressing through multiple layers—initiating with automated feature extraction and concluding with classification output [182].

Between the input image and the output layer, the CNN consists of a sequence of linear and non-linear operations where each layer is computed based on the previous layer (figure 4.10). The hidden layers of a CNN include:

1. **Convolutional Layers**: These layers use filters slides over the input image to perform convolution operations, producing feature maps that highlight relevant features.
2. **Pooling Layers**: Pooling layers down sample the feature maps (e.g. by taking the maximum of the feature: MaxPooling), reducing spatial dimensions while retaining essential information. Pooling helps make the network more robust to variations in object position and scale.
3. **Fully Connected Layers**: Also known as dense layers, these layers are typically used in the next-to-final layer of the network for classification or regression tasks. Their primary function is to establish connections between deep features extracted from feature maps and the output.

The last layer of the CNN architecture uses a S**oftmax** function to provide the classification result. Non-linear a**ctivation functions** are used to introduce non-linearity into the network, allowing it to model complex relationships in the data. Common examples are ReLU (Rectified Linear Activation) and Sigmoid.

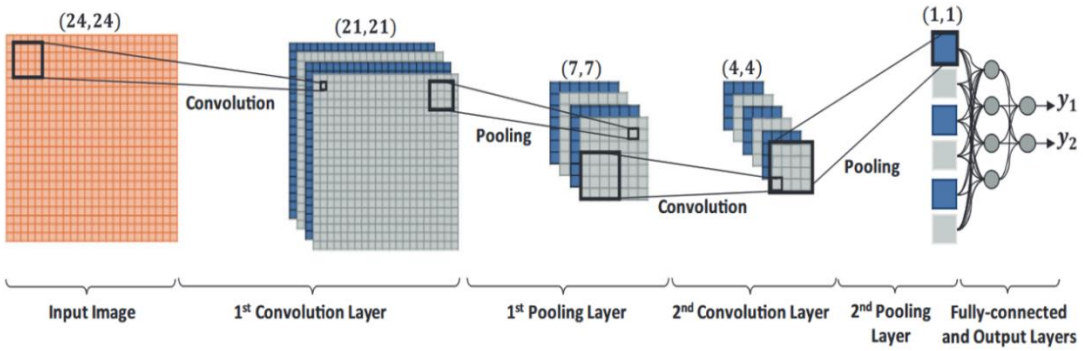


Figure 4.10 The illustration of a CNN with 2 convolutions and one fully-connected layers [185].

Generally, CNNs aim to learn the relationship between the input image and the output, storing the acquired experience in their kernels. Each convolutional layer is defined by its filter weights, established during the training stage through an iterative update process. These weights are initially initialized and then adjusted via backpropagation to minimize a cost function. Once the training is complete, all weights remain fixed during the testing phase.

The standard CNN provides the primary tool for various 2D signals applications such as images and video [121]. However, this option is not practical for many applications with 1D signals particularly when learning data is limited [185]. To address this issue, 1D-CNN has been recently introduced and rapidly demonstrated exceptional performance in various applications, including surface and subsurface defects detection.

## b. 1D-CNN

1D-Convolutional Neural Network (1D-CNN), the modified version of the standard CNN (also known as 2D-CNN), has been recently developed [186-187]. Notably, in 2015, Kiranyaz et al. [188] introduced the first compact and adaptable 1D-CNN designed to directly process patient's ECG signals. In a relatively short period of time, 1D-CNN has gained significant popularity, by presenting the best performance across various signal processing applications such as early anomaly detection in electrocardiogram beats [189-191], structural health monitoring and structural damage detection [192-194]. Research has demonstrated that in certain scenarios, 1D-CNNs are a better choice compared to the 2D-CNN when dealing with 1D signals. The reasons for this preference are as follows:

1. There is a notable difference in the computational complexity between the two models. The computational workload of a 1D-CNN is significantly lower than that of a 2D-CNN.
2. While training a 2D-CNN often requires specialized hardware setups like cloud computing or GPU arrays, however, training a 1D-CNN can be efficiently performed on standard computers, especially when using a limited number of hidden layers, such as two or fewer.
3. The reduced computational requirements of 1D-CNNs make them well-suited for real-time applications and cost-effective solutions. This advantage is particularly evident when deploying these networks on devices like mobile phones or wearable [195-197].

The layers used in a 1D-CNN are similar in concept to those used in a 2D-CNN, but they are adapted to operate on one-dimensional data. It's important to note that the primary difference between 1D and 2D-CNNs lies in how the convolution and pooling operations are applied to the data. In a 1D-CNN, these operations are applied along the temporal dimension, whereas in a 2D-CNN, they are applied spatially to both width and height dimensions. Figure 4.11 illustrates the architecture of a 1D-CNN applied to sequential data with dimensions (m*n). In this setup, a single convolutional layer is employed. Thus, it is important to note that the width of the convolutional filter is the same width of the input dimensions. The convolutional filter is applied in one direction along the data. This enables the filter to slide through the sequential data, capturing relevant features as it progresses along the sequence.

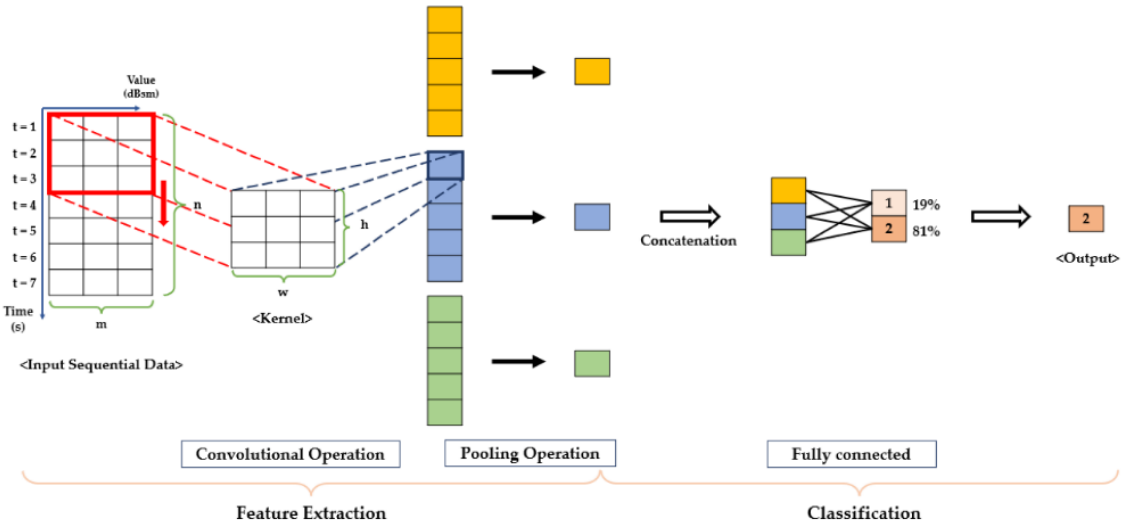


Figure 4.11 An architecture of the 1D-CNN for classification of two classes [198].

## 4.2.6. Performance evaluation

A robust approach to validate ML models is to train them on non-testing data and subsequently evaluating their performance using unseen or testing data. However, when dividing a dataset once into training and testing subsets, it is crucial to ensure that the division is representative of all classes present in the dataset. If the division is not random and results in an unbalanced distribution of classes between the two sets, it can indeed lead to poor performance evaluation and potentially biased results. K-fold cross Validation (CV) technique comes in to solve the problem [199].

Using K-fold CV, the non-testing subset is randomly divided into k folds (groups). During each round, one fold is kept aside for validation and the remaining folds were used for training [200]. The k-fold CV concept is illustrated in figure 4.12. By implementing this process, all the data in the dataset are utilized at least once to evaluate the performance of the trained models. *k* is usually chosen to be 5 or 10 as a bias-variance trade-off [201] . In our study k is set to five, meaning that the dataset is divided into five folds.

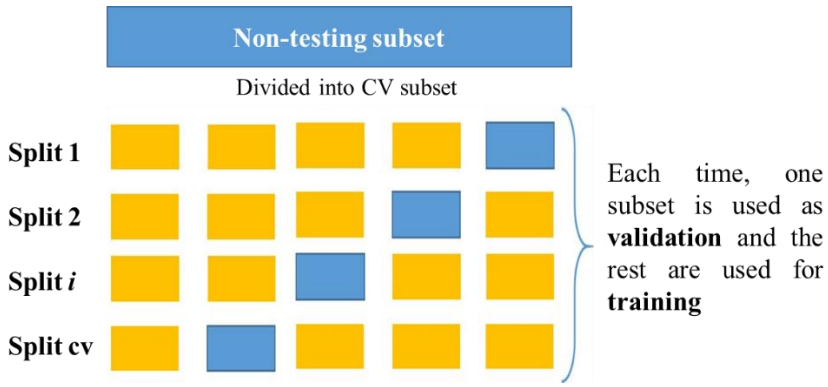


Figure 4.12 K-fold cross validation technique.

After implementing 5-fold cross-validation, the model's performance is assessed using a range of performance metrics. These metrics are applied both on the testing subset and a separate non-testing subset, enhancing the models' overall robustness. Here, we present the performance metrics utilized in this study.

Evaluation metrics play a crucial role in assessing the performance and effectiveness of ML models. These metrics quantify how well the model is performing on a given task and provide valuable insights into its strengths and weaknesses. In this study, the following performance measures were employed:

- **Accuracy** quantifies the number of correct predictions made by the classifier, divided by the total number of predictions made.
- **Sensitivity,** also known as recall or true positive rate, quantifies the effectiveness of a test in correctly detecting positive instances.
- **Precision** denotes the accuracy of the positive predictions made by the algorithm. It is computed by dividing the true positives by the sum of true positives and false positives.
- **F1 score**: a harmonic mean of precision and sensitivity, offers a balanced measure that considers both false positives and false negatives (as shown in equation 1).

These performance metrics are often multiplied by 100 to represent them as percentages.

$$F1_{score} = \frac{2 * (precision * sensitivty)}{(precision + sensitivty)} \quad (4.1)$$

## 4.3. Material characterization based on ML and microwave techniques

Recently, there has been a growing focus on the advancement of MNDT&E approaches [202] due to the necessity of reducing the dependence on the operators' skills and experience [145]. Hence, employing intelligent classifiers in signal processing provide reliable and fast inspection, potentially enhancing the sensitivity of material characterization and defects detection [203]. Using ML is further justified, as its nonlinear classification capabilities can effectively address the complexity of the acquired data [204].

Commonly, intelligent MNDT&E progresses through three distinct phases. The first stage is a preprocessing phase which aims to eliminate the noise and eliminate unnecessary data. The second stage is the features extraction and selection which aims to extract and select the most significant features from the input data. Finally, the classification or prediction stage aims to classify material's unique characteristics and recognize the defects as well as to estimate the defects' characteristics.

In summary, this combination enables accurate and rapid material characterization, even when dealing with complex scenarios involving multiple material types. Moreover, it reduces the dependency on complex conversion methods and provides an automated process. In the following, we present important studies of combined MNDT&E techniques with AI models.

In [205] the authors propose a novel nondestructive method for health monitoring of wind turbine blade. The method utilizes frequency modulated continuous wave radar FMCW sensing within the frequency range of 24-25.5 GHz, combined with ML analytics. The study's findings indicate that blade types can be accurately classified by their composition, and diameter differentials of 3 millimeters with a classification accuracy exceeding 95%. In [206] authors introduce a novel approach that uses microwave free-space technique with ML analytics to identify foreign materials present in uncleaned peanuts. The method relies on the measurement of dielectric properties and bulk density of these materials. Both linear regression and ANN algorithms are employed in the analysis. The experimental results demonstrate that the ANN algorithm provides the most accurate estimation of foreign material content, with a standard error of performance of 1.36%. In comparison, the linear regression algorithm achieves a standard error of performance of 2.39%. In [145] a real-life experiment for intelligent crack detection in metallic surfaces. the proposed approach is based on using AI-models with a waveguide sensor loaded with split-ring resonator. The AI-models combines ANN and SVM algorithms. The experimental evaluation of this approach was performed on a metallic plate with different cracks, and was able for accurate crack detection. **In the following table, we provide a summary of the significant studies, including the used techniques and the field of applications.**

| Reference number | Technique | Application |
|---|---|---|
| [205] | FMCW Radar with ANN, SVM & DCT | Classification of blade types by their composition |
| [206] | Four microwave free-space antenna system with linear regression and ANN | Identification of foreign materials present in uncleaned peanuts |
| [207] | Coaxial line with ANN | Retrieval of the complex permittivity of MUTs |
| [208] | Coaxial line with CNN | Prediction of the complex dielectric properties of granular catalysts |
| [209] | Waveguide sensor with PCA, ANN and SVM | Detection of sub-millimeter cracks in metallic surfaces |
| [210] | OERW with ANN | Detection of defects in dielectric structures |
| [211] | FMCW radar with k-means and NN | Characterization of dielectric material properties |

Table 4.2 Summary of MNDT techniques with ML and DL method used in various applications.

## 4.4. ML-based monostatic free-space radar for material characterization

In this section, we introduce and experimentally validate a novel intelligent MNDT&E technique to characterize planar dielectric materials in non-contact manner regardless their thicknesses. The proposed technique relies on using a monostatic free-space radar system to measure the $S_{11}$ parameters (magnitude and phase-shift) of the MUT along with the use of ML models to categorize three well-known dielectric materials: wood, glass, and plexiglas. The antenna is positioned at a distance from the MUT. Given various factors, including the unknown geometry of the MUT and the impact of surrounding noise, performing analytical modeling of the propagation path through the material becomes impractical. In overcoming these challenges ML algorithms have a crucial role to play [212].

In the following the methodology of the proposed technique is presented in the section 4.4.1. Remaining sections present the experimental setup, dataset construction, data processing, the implementation of ML models, and conclude with the presentation of results and performance evaluation.

### 4.4.1. Methodology

As described in figure 4.13, the proposed methodology consists of three main steps: (1) data acquisition, (2) data processing, (3) training and evaluating the ML classifiers. The data acquisition step involves generating a novel and unique dataset by conducting measurements in two distinct environments conditions. The first group of data was recorded under laboratory conditions, while the second group was obtained in relatively noisy environments to simulate realistic conditions. Initially, the radar system measures the$S_{11}$, capturing variations in magnitude and phase-shift across a frequency range varying from 3.95 to 5.85 GHz with a step of 2.2MHz. The recorded data is influenced by the type of the MUT. Before feeding the data into the ML algorithms, a preprocessing step is conducted, applying five different features scenarios. The purpose of studying different training features is to identify the optimal features, achieving a balance between the number of features and the performance of the ML algorithms. Five ML algorithms are then employed to classify the materials, and their output falls into one of the following four categories: wood, glass, Plexiglas, or air (no MUT). To evaluate and compare the performance of different scenarios, a variety of evaluation metrics are used. These metrics provide valuable insights into the effectiveness of the proposed methodologies.

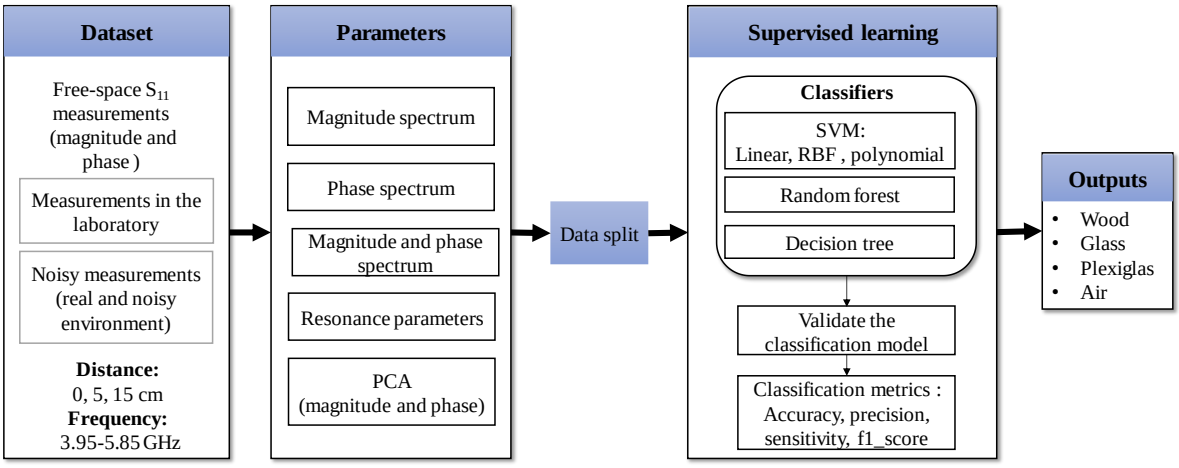


Figure 4.13 Block diagram of the proposed methodology for material characterization.

## 4.4.2. Experimental setup

The radar system is built up with a compact one-port VNA [Anritsu® MS46121B – figure 4.14(a)] connected to a horn antenna [ATM® P/N 187-251-6 – figure 4.14 (b)]. The antenna is connected to the input port of the VNA using N-to- SMA coaxial transition and SMA-to-waveguide transition. No coaxial cable is considered to reduce random errors commonly found and attributed to cable movement during measurement operation. The measurement configuration is depicted in table 4.3.

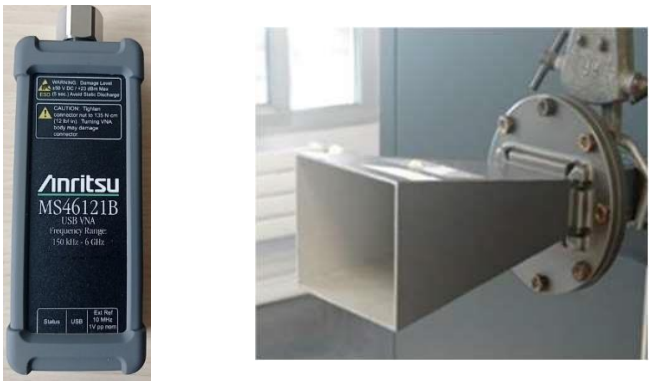


*(a)* *(b)*

Figure 4.14 (a) Compact 1-port vector network analyzer Anritsu® MS46121B (150 kHz – 6GHz). (b) Horn antenna [ATM® P/N 187-251-6].

In particular, the VNA IFBW is set to 100Hz as compromise between measurement time (10s) and measurement accuracy. Before starting the measurement, the VNA must be calibrated to correct systematic errors and ensure the quantitative measurements. The calibration procedure is performed at the input coaxial plane of the horn antenna. A short-open-load (SOL) calibration (calibration-kit: OSLN50A-8 from Anritsu®) is used.

| | |
|---|---|
| Frequency range (GHz) | **3.95 – 5.85** |
| IFBW (Hz) | 100 |
| Number of points | 863 |

Table 4.3 $S_{11}$ measurement configuration using the horn antenna and the VNA.

### 4.4.3. Quantifying measurement uncertainties

Uncertainty quantification step is conducted before any measurements; a repeatability study is considered to quantify the overall measurement uncertainty and to ensure the reproducibility of measurements including mechanical positioning of the MUT. To that end, the MUT consists of wood in planar structure was positioned at a stand-off distance set to 5 cm. $S_{11}$ is measured 10 consecutive times. Between two consecutive measurements, we remove and put back the material at the same position. The resulting data are plotted in figure 4.15. From these data, the maximum standard deviation between all measurements are computed at each frequency. Maximum standard deviations of 0.0018 and 3deg, for the linear magnitude and phase-shift of $S_{11}$ respectively, are obtained.

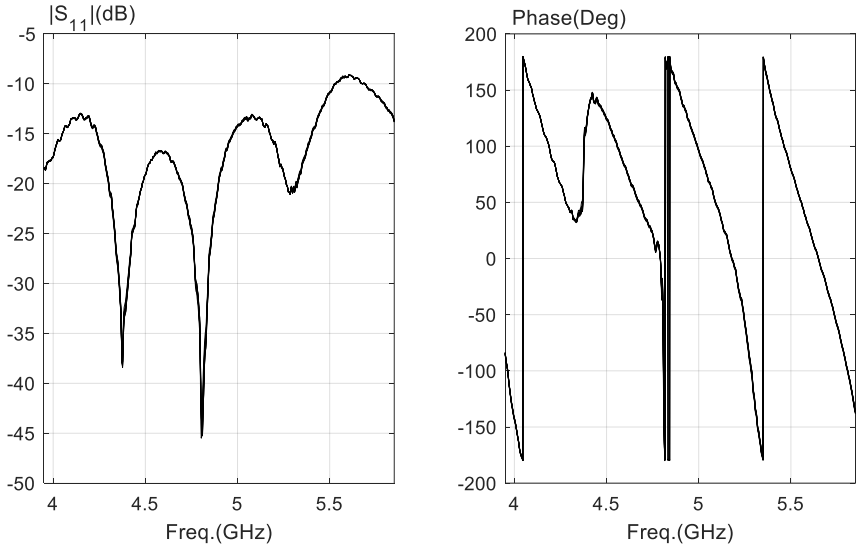


Figure 4.15 Ten measured $S_{11}$ in the frequency range 3.95 – 5.85 GHz. MUT = planar wood sample – stand-off distance is set to 5 cm.

The resulting measurement uncertainty, attributed mainly to displacement error, is informative as it shows the limits of the measurement device. The results of quantification study confirm the precision of the proposed measurement system and provide essential groundwork for the upcoming measurements. As we proceed, we will observe that the highest standard deviation in both magnitude and phase-shift remains smaller than the fluctuations attributed to the difference in MUT types. This highlights the system's ability to effectively distinguish and quantify changes in the MUT.

## 4.4.4. Acquisition and construction of an original dataset

The measurements campaign consists of two steps. First, the$S_{11}$is measured without MUT. Then, $S_{11}$ measurements are performed for all samples at three stand-off distances (0 cm, 5 cm, and 15 cm) between the antenna and MUT. The steps are repeated under the two conditions: controlled laboratory and more challenging realistic conditions.

The $S_{11}$measurements without MUT are performed throughout the experimental days before starting any measurements on the material samples. Figure 4.16 presents the photograph of the experimental system without MUT.

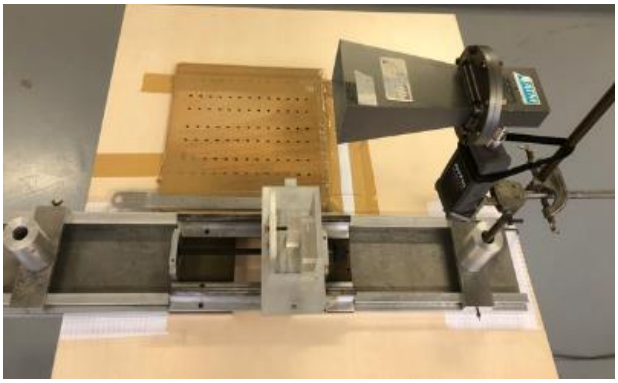

Figure 4.16 Experimental system of microwave sensing without MUT in front of the horn antenna.

Figure 4.17 shows the measured magnitude and phase-shift of $S_{11}$ without MUT. The magnitude has two minima at two frequencies. These minima are referred to as resonance frequencies (table 4.4).

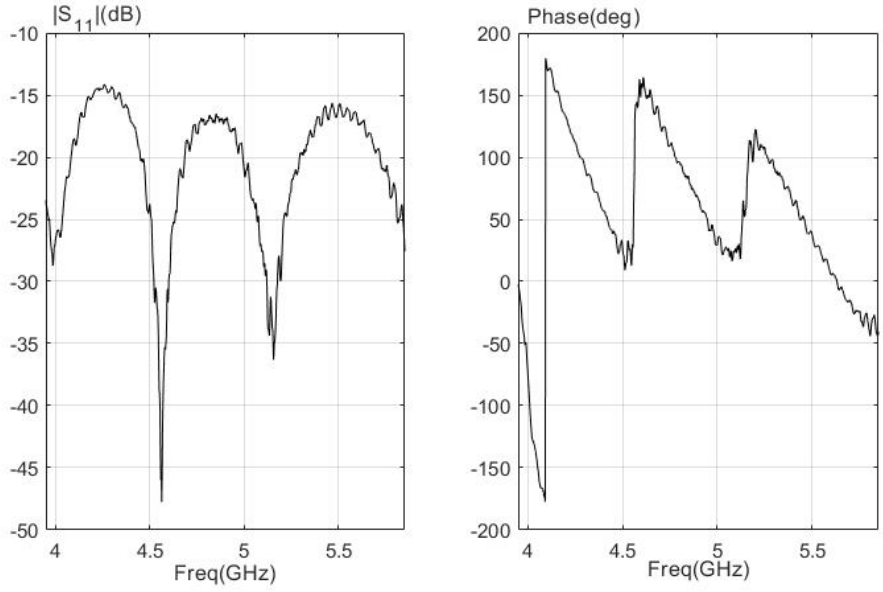


Figure 4.17 Measured $S_{11}$ without MUT.

| Resonance frequency 1 | Resonance frequency 2 |
|---|---|
| $4.5145 \pm 0.1605$ | $5.0918 \pm 0.1590$ |

Table 4.4 Resonance frequencies presented in the measured $S_{11}$ by the antenna without MUT.

After conducting measurements without MUT, the system is used for measuring the $S_{11}$ of different materials. Samples with known material properties, such as, wood, glass and Plexiglas are used. Figure 4.18 shows photos of some samples, while table 4.5 presents the thicknesses of the samples.

Figure 4.18 Some of the material samples considered for materials classification.

| Material | Thickness (cm) |
|---|---|
| Wood | { 0.6 ; 0.9 ; 1; 1.6; 1.8} |
| Glass | {0.2; 0.4; 0.5} |
| Plexiglas | {0.25; 0.4} |

Table 4.5 Thicknesses of the experimental samples.

Measurement data were collected over twelve days. The experimental measurement system set up is shown in the figure 4.19. The antenna is fixed for all experiments and only the MUT is moved using a mechanical displacement mechanism with 500μm displacement resolution.

Figure 4.19 Experimental system for microwave broadband free-space sensing. Different planar MUT in front of the horn antenna.

The MUT is positioned parallel to the antenna with stand-off distances set respectively to 0, 5 and 15 cm to maximize the electromagnetic coupling and limit the diffraction effects. In particular, operation in the near-field conditions reduce drastically non-systematic errors commonly found in conventional configurations operating in the far-field region. In particular, diffraction at the edges are eliminated and measurement sensitivity is enhanced. Indeed, as the antenna operates in the near-field of the material, electromagnetic coupling between the antenna and the material induce free-space interferences between incident and reflected waves. These interferences cause frequency resonances in the magnitude spectra of the measured broadband$S_{11}$. The locations and levels of these interferences are specific to the MUT. Nevertheless, the analytical modelling of the propagation is challenging, highlighting the interest of ML algorithms.

Table 4.6 presents the number of samples recorded at three stand-off distances under the two conditions: first group recorded in laboratory conditions and the second group recorded in noisy conditions.

| Stand-off distance (cm) | First group | Second group |
|---|---|---|
| 0 | 158 | 45 |
| 5 | 161 | 49 |
| 15 | 154 | 55 |

Table 4.6 Number of recorded measurements using the horn antenna at three stand-off distances for the two groups.

The measurements conducted without MUT and those for all samples are combined into a single dataset. Figure 4.20 illustrates the recorded magnitude and phase-shift of $S_{11}$of some wood samples with different thicknesses at stand-off distance set to 5 cm. It is worth noting that each wood sample exhibits unique characteristics in terms of magnitude and phase-shift, which is further supported by slight variations in resonance frequencies as presented in table 4.7. These differences are mainly related to the varying thicknesses of the wood samples.

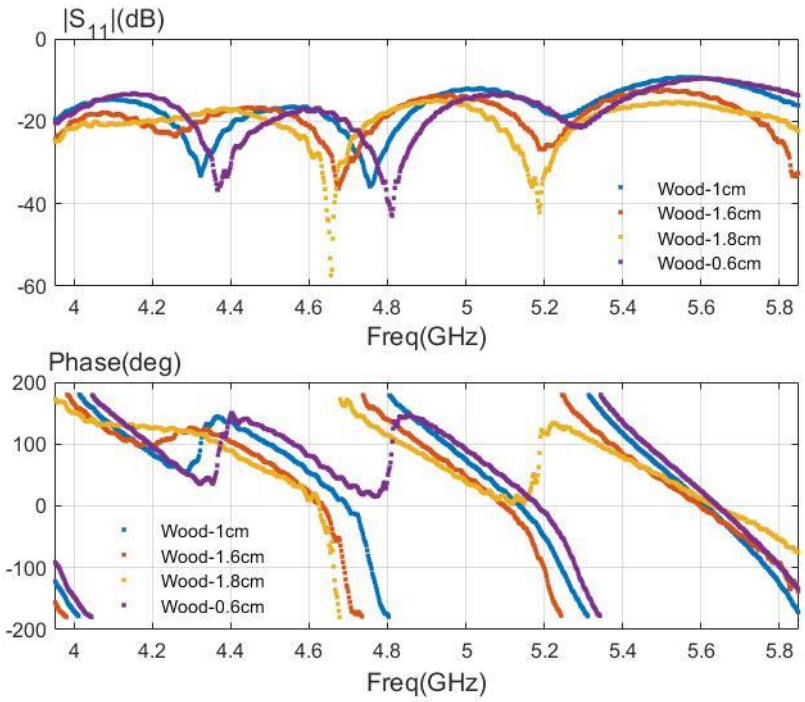


Figure 4.20 Measured $S_{11}$ of wood samples with different thicknesses. The stand-off distance is set to 5 cm.

In addition, the recorded $S_{11}$(magnitude and phase-shift) of various material samples at stand-off distance set to 5 cm are presented in figure 4.21. The antenna aperture is positioned at the center of each MUT.

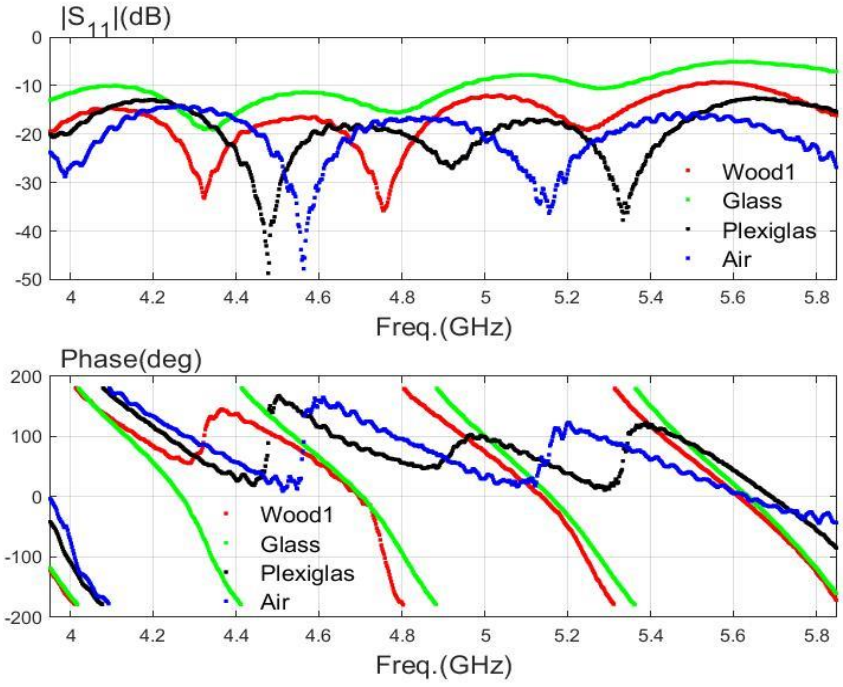


Figure 4.21 Measured $S_{11}$ of some samples. The stand-off distance is set to 5 cm.

It is noticed that each type of material has its own resonance frequencies. This observation aligns with the results presented in the table 4.7. The unique resonance parameters displayed by each material make them suitable as features for training ML algorithms.

| | **Wood** | **Glass** | **Plexiglas** |
|---|---|---|---|
| **Sample 1** | 4.317; 4.7548 | 4.3302; 4.787 | 4.4776; 5.346 |
| **Sample 2** | 4.3192; 4.757 | 4.3412; 4.823 | 4.4776; 5.3312 |
| **Sample 3** | 4.6866; 5.8372 | 4.34258; 4.757 | 4.4776; 5.3356 |
| **Sample 4** | 4.7152; 5.2278 | 4.3236; 4.7548 | 4.4776; 5.3334 |

Table 4.7 Extracted resonance frequencies (GHz) for some samples. The stand-off distance is set to 5 cm.

Figure 4.22 presents the recorded $S_{11}$ (magnitude and phase-shift) of various material samples at stand-off distance set to 0 cm. It is worth noting that there are no resonance frequencies observed when the MUT is in direct contact with the antenna. However, distinctive differences exist in both the magnitude and phase-shift characteristics of each material, highlighting their unique properties.

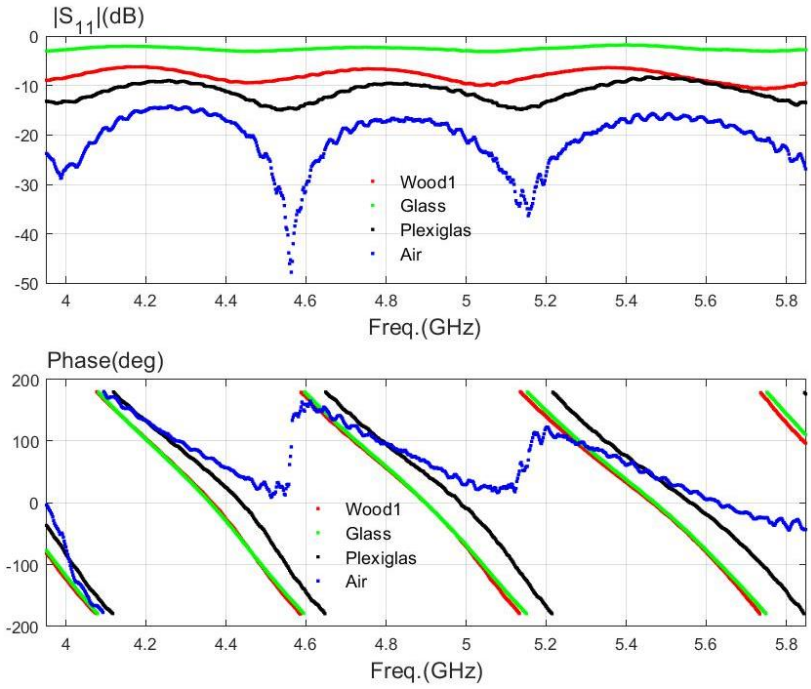


Figure 4.22 Measured $S_{11}$ of some MUTs. The stand-off distance is set to 0 cm.

Figure 4.23 presents the recorded $S_{11}$ (magnitude and phase-shift) of the same materials with stand-off distance set to 15 cm. As previous findings, each material features its distinctive characteristics, and resonance frequencies become evident in the recorded magnitude. However,

as the stand-off distance between the antenna and the MUT increases, the influence of diffraction effects becomes more important. Consequently, as shown in the figure 4.23, the recorded data show a degree of proximity, indicating the impact of distance on the measurements.

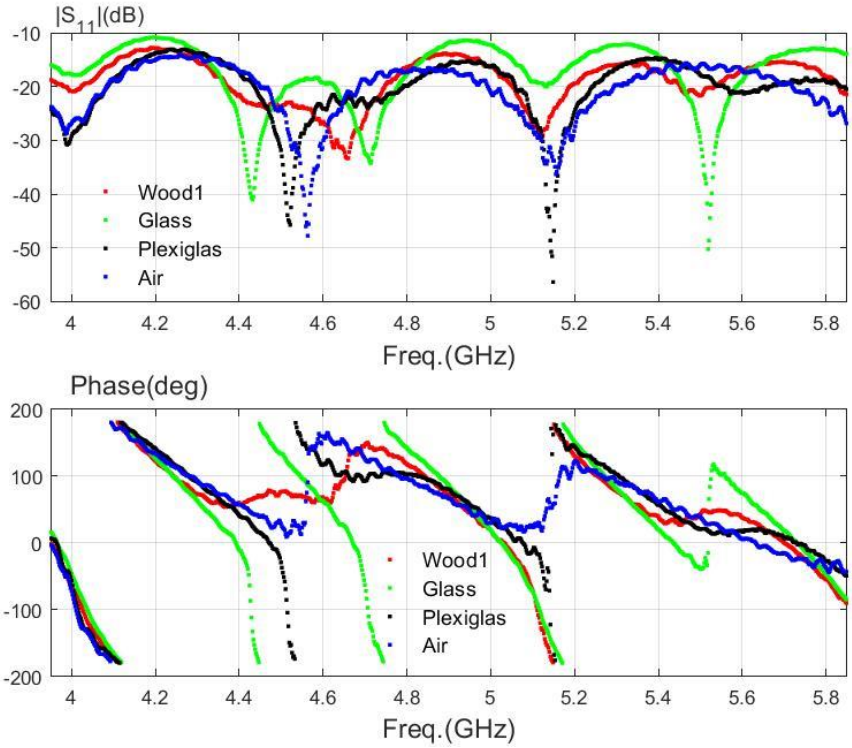


Figure 4.23 Measured $S_{11}$ of some MUTs. The stand-off distance is set to 15 cm.

## 4.4.5. Data processing and Machine learning

### a. Feature selection

Feature selection is a process that involves selecting the best subset of features from a large set of available features. This process offers advantages such as reducing overfitting (less redundant features), increasing classification accuracy, and reducing computational complexity. Thus in order to obtain a good classification, the selection of appropriate features is crucial. These features must consider correlations with the physical characteristics of the MUTs from the point of view of material science. Therefore, we employ two feature selection scenarios.

Initially, we use recorded magnitude of $S_{11}$measurements, then proceed to include recorded phase measurements, highlighting the significance of measuring both parameters for material characterization.

We use PCA, which is widely recognized as one of the most popular methods for dimensionality reduction in feature selection [213-217]. Specifically, we retain PCA components that contribute to more than 90% of the total variance in the magnitude and phase-shift data.

Furthermore, we used the resonance parameters as features to drive the ML algorithms. The use of resonance frequencies as features has recently received a significant attention in the literature [90]-[137]. The resonance frequency and the corresponding magnitude (or the quality factor at -3dB bandwidth) is directly affected by the MUT's type where. This observation is

aligned with the findings presented in the figure 4.21 and 4.23. For this reason, six features (resonance parameters) were extracted from the measured data: both minimum magnitudes, corresponding frequencies, named resonance frequency. To achieve robust classification, the corresponding phase-shifts are also considered.
Consequently, the five different scenarios for features selection are used: (a) using only the recorded magnitude measurements, (b) using only the phase-shift measurements, (c) using both magnitude and phase-shift measurements, (d) using the six resonance parameters, (e) using PCA components applied to both magnitude and phase-shift measurements.

## b. Data split

In this study, the collected data consists of two distinct groups (figure 4.24). The first one, which was recorded in laboratory conditions, was used as the non-testing subset to train the ML models. This subset was further divided into training and validating subset using 5-fold cross-validation (CV). The second group, which was recorded in realistic and noisy conditions, was used as the testing or unseen subset for the purpose of validating the ML algorithms to avoid possible bias, overfitting and poor generalization [218].

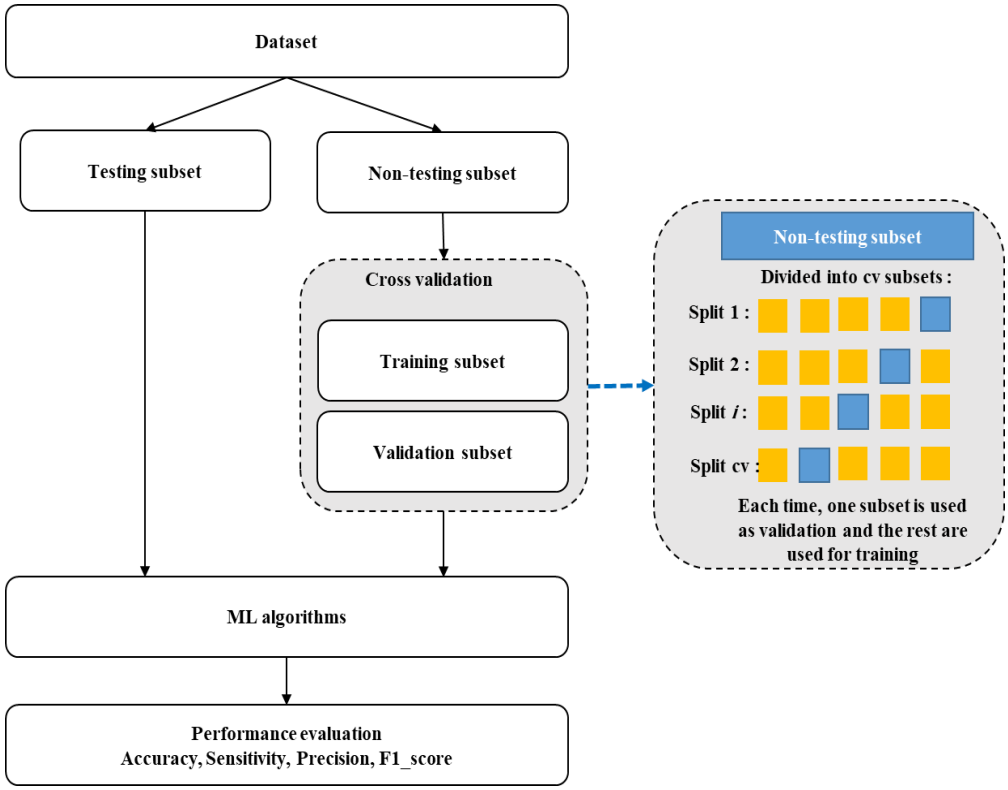


Figure 4.24 Training, validation and testing configurations.

By evaluating the models on this separate and challenging dataset, we could confirm their robustness and their ability to address real-world scenarios.

## c. Supervised classification

Analytical modelling of the wave-to-material interaction is relatively complicated as the MUTs are positioned in the near-field region. In addition, modelling requires knowledge of the

material thicknesses. This highlights the interest of using ML algorithms. In this work we used supervised algorithms to classify the recorded $S_{11}$, i.e. specify the types of materials, based on five well-known supervised ML algorithms: random forest (RF), decision tree classifier (DTC) and support vector machine (SVM) with three kernel functions: linear, polynomial (POL.) and radial basis (RBF). Each kernel can be fitted to the corresponding model by adjusting the corresponding parameters: cost (C) and gamma ( $\gamma$). These parameters were optimized using the grid search method in order to maximize the accuracy rates.

These algorithms are commonly used in the literature and they can provide excellent performance for classification and regression.

### 4.4.6. Results and performance evaluation

In this section, we aim to evaluate the performance of the proposed ML models, considering various feature scenarios and three distinct stand-off distances: 0, 5, and 10 cm. We analyze these performances under both controlled laboratory conditions and more realistic real-world conditions.

The first group of data at 5 cm (161 measurements) is divided using the 5-fold cv technique into training and validation subsets. The training process involved five different scenarios for features selection, (a) using only the recorded magnitude measurements, (b) using only the phase-shift measurements, (c) using both magnitude and phase-shift measurements together, (d) using the six resonance parameters, (e) using PCA components applied to both magnitude and phase-shift measurements. Thereafter, we evaluate the performance of the ML models using the metrics: accuracy, sensitivity, precision, and F1 score.

Table 4.8 illustrates the results of the classification performance at stand-off distance set to 5 cm on two subsets: CV subset (non-testing subset) and unseen subset (second group recorded under noisy conditions).

| | **(a) Magnitude** | | **(b) Phase-shift** | | **(c) Magnitude & Phase-shift** | | **(d) Resonance elements** | | **(e) PCA** | |
|---|---|---|---|---|---|---|---|---|---|---|
| **Data Subset** | CV subset | Unseen subset | CV subset | Unseen subset | CV subset | Unseen subset | CV subset | Unseen subset | CV subset | Unseen subset |
| **Accuracy (%)** | 98 $\pm$0.5 | 91 | 99 $\pm$0.3 | 95 | 99 $\pm$0.3 | 95 | 97 $\pm$0.6 | 33 | 99 $\pm$0.5 | 91 |
| **Sensitivity (%)** | 98 | 92 | 98 | 92 | 98 | 95 | 97 | 29 | 98 | 92 |
| **Precision (%)** | 98 | 91 | 98 | 91 | 98 | 95 | 96 | 33 | 98 | 91 |
| **F1_score (%)** | 98 | 90 | 98 | 90 | 98 | 95 | 96 | 31 | 98 | 90 |
| **Best Classifiers** | SVM RBF | | SVM RBF | | SVM RBF | | RF | | SVM POL (degree=2) SVM RBF | |

Table 4.8 Performance of the best ML classifiers trained with five feature Scenarios. Stand-off distance is set to 5 cm.

As shown, SVM with RBF kernel gives the best performance when using magnitude, phase-shift or both magnitude and phase-shift of $S_{11}$as features. RF gives the highest performance when using the resonance parameters as features. SVM with polynomial and RBF kernels give similar highest performance when using PCA on the measured $S_{11}$(magnitude and phase-shift).

Similar performance is demonstrated across all features combinations within the cross-validation subset. However, an improvement in classifier performance is observed when both magnitude and phase-shift features under noisy conditions (unseen subset) were used, achieving 95% accuracy across all evaluation metrics.

It is worth noting that the introduction of PCA led to a slight decrease in performance (accuracy, sensitivity, precision, and F1 score were respectively 91%, 92%, 91%, and 90%). Nevertheless, the use of PCA contributes to a reduction in computational complexity. It is also noticed that classifiers trained on resonance features show a significant drop in performance when tested on the noisy subset. This can be attributed to the sensitivity of the resonant frequency to the influence of environmental noise.

To further investigate the robustness of the proposed method, further analysis was conducted by examining the impact of varying the stand-off distance between the MUT and the antenna. Table 4.9 presents the classification performance results using SVM with RBF kernel functions (polynomial kernel yielding similar performance) at different stand-off distances: 0 cm, 5 cm, and 15 cm. The SVM model is trained on the first group of data recorded under controlled laboratory conditions and then tested on the second set of data collected under noisy conditions.

| **Stand-off distances** | **0 cm** | | **5 cm** | | **15 cm** | |
|---|---|---|---|---|---|---|
| **Sample size: Training set/ Unseen set** | 158/45 | | 161/49 | | 154/55 | |
| **Features** | Magnitude & Phase-shift | PCA | Magnitude & Phase-shift | PCA | Magnitude & Phase-shift | PCA |
| **Accuracy (%)** | 100 | 95 | 95 | 91 | 86 | 94 |
| **Precision (%)** | 100 | 96 | 95 | 92 | 76 | 95 |
| **Sensitivity (%)** | 100 | 95 | 95 | 91 | 86 | 94 |
| **F1_score (%)** | 100 | 95 | 95 | 90 | 90 | 94 |

Table 4.9 Performance of two classifiers: SVM polynomial (POL.), SVM RBF, evaluated at three different stand-off distances: 0 cm, 5 cm and 15 cm.

The results indicate that the performance is notably better when the objects are in contact (0 cm). However, even at a stand-off distance of 15 cm, the classifiers still have some level of performance, even lower than that observed at closer distances.

## 4.5. ML-based OERW for material characterization

It is proven in the previous section that a monostatic free-space radar with ML classifiers, can provide the characterization of dielectric materials with high accuracy. This setup allows for remote sensing applications where non-contact measurements are essential.

In this section, we propose a novel 'intelligent' MNDT&E technique for materials characterization using **contact setups** with the MUT. This method is based on scanning the dielectric material with the OERW and analyzing its reflections signals using the proposed ML models.

In the following, we describe the material characterization setup using the OERW, starting with the methodology, followed by the experimental setup, the construction of the dataset, the used ML models and concluding with the presentation of results and performance evaluation.

### 4.5.1. Methodology

In this section, the proposed technique basically consists of three steps: (1) data acquisition, (2) data processing, (3) training and evaluating ML classifiers. First, we create a new, original dataset based on the utilization of the OERW. The system measures the$S_{11}$, capturing variations in magnitude and phase-shift across a frequency range varying from 3.95 to 5.85 GHz with a step of 2.2MHz. The same materials featured in Section 1 are employed in this experimental setup, and measurements are conducted in two distinct environmental conditions. The first group is recorded under controlled laboratory conditions, while the second group is obtained in noisy environments to simulate real-world scenarios. These measurements hold significant importance for our application, as the majority of measurements are anticipated to occur in challenging conditions.

The process pipeline of the proposed technique is presented in the figure 4.25. After measuring the $S_{11}$for all materials, a preprocessing step is performed, which includes labeling and feature extraction. This step primarily involves categorizing the data into specific labels: wood, glass, plexiglas, and air. We then proceed with data splitting, where the dataset is divided into two subsets. The first subset, referred to as the 'non-testing subset', consists of the first group of data recorded under controlled laboratory conditions. The second subset, known as the 'testing subset', consists of the second group of data collected under more realistic conditions. To extract the most informative features and reduce dimensionality, PCA is applied to the **non-testing subset** after standardizing the data. Subsequently, the incoming data is divided into training and validation subsets using a 5-fold CV approach. This division serves the purpose of training and validating five ML models: DCT, RF, and SVM with three distinct kernel functions: linear, RBF, and polynomial. The effectiveness of these models is computed using various performance metrics applied to the validation subset. After the training phase, these models are put to the test using the testing subset, allowing for an evaluation of the performance of the proposed classifiers

on new unseen data. The classifier outputs are categorized into four classes: glass, plexiglas, wood, and air.

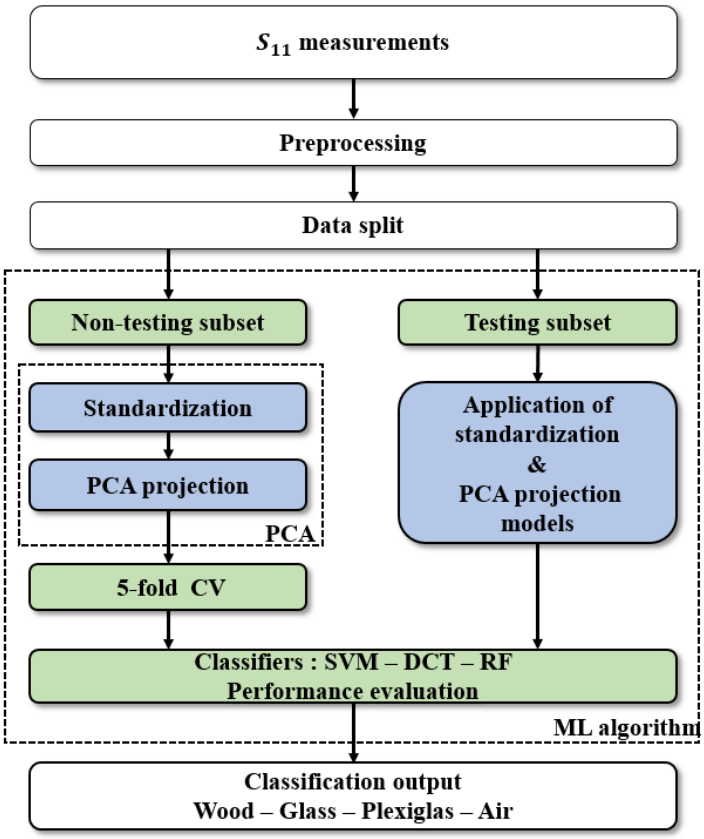


Figure 4.25 Block diagram of the proposed methodology for material characterization using OERW system and ML models.

## 4.5.2. Experimental setup

The microwave system used in this work is built up with an OERW [ATM® P/N 187-251-6] presented in the figure 4.26 with the VNA [Anritsu® MS46121B MS46121B]. The waveguide has a cross section of 50 mm by 25 mm and it is connected to the input port of the VNA using N-to- SMA coaxial transition and SMA-to-waveguide transition. The measurement operates within the frequency covered by the waveguide between 3.95 and 5.85 GHz with a step of 2.2MHz. The measurements configuration is depicted in table 4.10. Before starting the measurement, the VNA is calibrated using the same calibration-kit: OSLN50A-8 from Anritsu®).

(a) Front view (b) Bottom side view (c) Back view

Figure 4.26 Waveguide [ATM® P/N 187-251-6].

| | |
|---|---|
| Frequency range (GHz) | 3.95 – 5.85 |
| IFBW (Hz) | 100 |
| Number of points | 863 |

Table 4.10 $S_{11}$ measurement configuration using the OERW and the VNA.

### 4.5.3. Quantifying measurement uncertainties

Before initiating the measurement campaign, a repeatability study is considered to quantify the overall measurement uncertainty. To that end, the MUT consists of wood in planar structure was positioned in contact with the OERW. $S_{11}$ is measured as a function of frequency 10 consecutive times. Between two consecutive measurements, we remove and put back the OERW. The resulting data are plotted in figure 4.27.

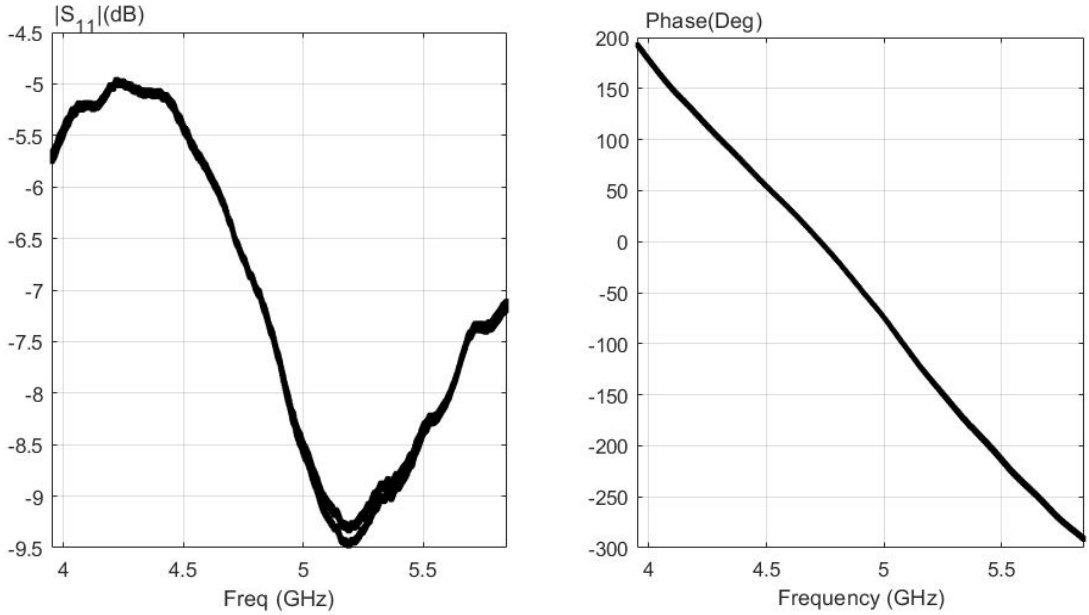


Figure 4.27 Ten measured $S_{11}$ in the frequency range 3.95 – 5.85 GHz. MUT = planar wood sample.

From these data, the maximum standard deviation between all measurements are computed at each test frequency (figure 4.28). Maximum standard deviations of 0.0028 and 0.75 degree, for the linear magnitude and phase-shift of $S_{11}$ respectively, are obtained.

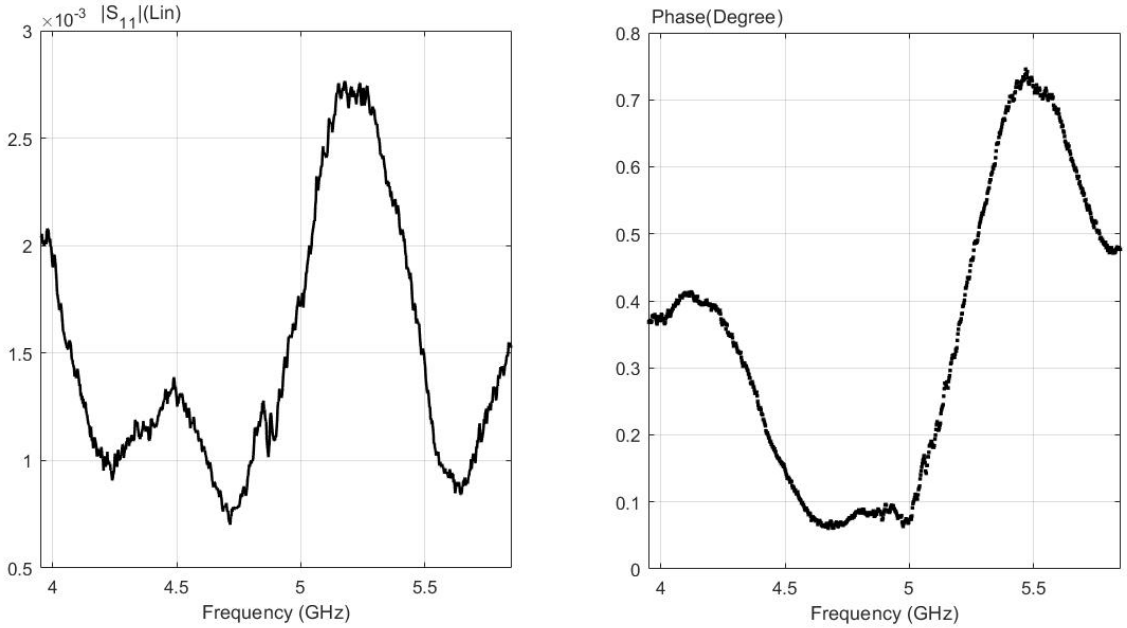


Figure 4.28 Standard deviation calculated on the ten measured $S_{11}$ in the in the frequency range 3.95 – 5.85 GHz. MUT = planar wood sample.

The resulting measurements uncertainty, attributed mainly to displacement error, is informative as it shows the limits of the measurement set-up. The results of this quantification study confirm the precision of the proposed measurement system and provide essential groundwork for the upcoming measurements. As we proceed, we will observe that the highest standard deviation in both magnitude and phase-shift remains smaller than the variations induced by the differences in the MUT's properties. This highlights the system's ability to effectively distinguish and quantify changes in the MUT.

## 4.5.4. Acquisition and Construction of an Original dataset

A new and original dataset is created. Sample featured in Section 1 are used again here for material characterization using the OERW. Table 4.11 presents the used materials and their thicknesses.

| **Material** | **Thickness (cm)** |
|---|---|
| Wood | { 0.6 ; 0.9 ; 1; 1.6; 1.8} |
| Glass | {0.2; 0.4; 0.5} |
| Plexiglas | {0.25; 0.4} |

Table 4.11 Thicknesses of the used samples.

The measurement campaign consists of two steps. First, the$S_{11}$is measured without MUT. Then, $S_{11}$ measurements are performed for all samples. The steps are repeated under the two conditions: controlled laboratory and more challenging realistic conditions.

The $S_{11}$measurements without MUT are performed throughout the experimental days before starting any measurements on the material samples. Figure 4.29 presents the measured $S_{11}$without MUT.

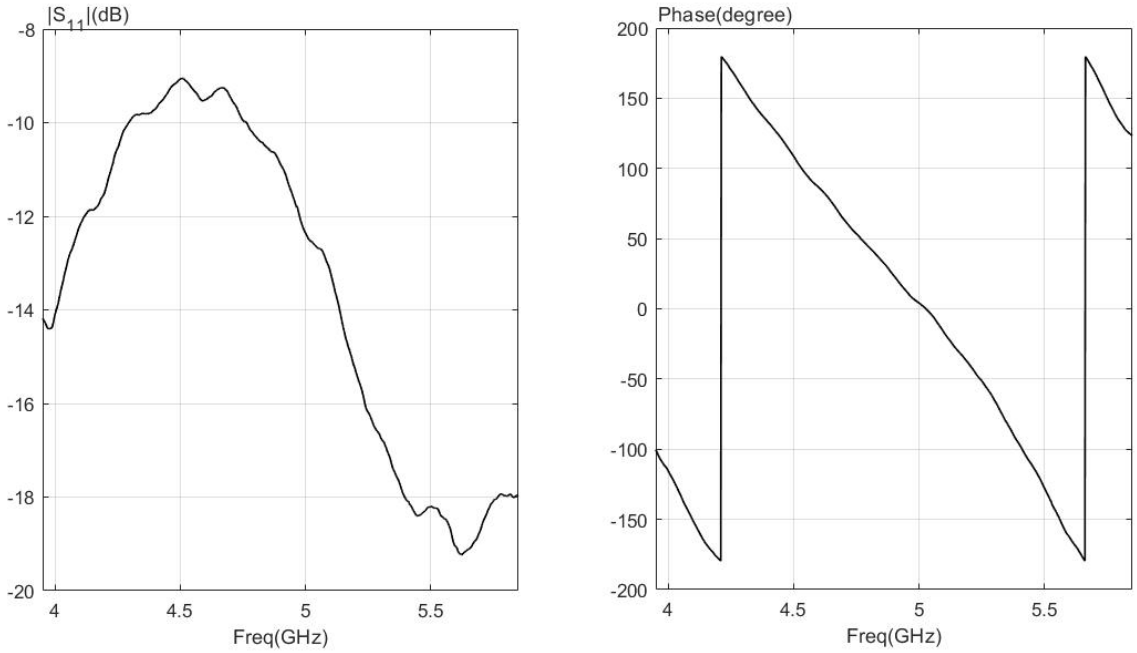


Figure 4.29 Measured $S_{11}$ without MUT.

Furthermore,$S_{11}$ measurements are performed for all samples. The experimental measurement system set up is shown in figure 4.30. In a simplified configuration, the OERW is manually scanning in contact manner with the MUT to measure its $S_{11}$. The data were collected on thirteen different days. On each day, the experiment configuration was rebuilt and multiple free-space measurements were conducted to ensure full repeatability of the experimental findings. Then the data was mixed into one dataset comprising 617 measurements for the first group and 270 measurements for the second group (table 4.12). The dataset consists of measurements of air (without MUT as well as samples of wood, glass, Plexiglas.

| Stand-off distance (cm) | First group | Second group |
|---|---|---|
| 0 | 617 | 270 |

Table 4.12 Dataset of recorded measurements using the OERW.

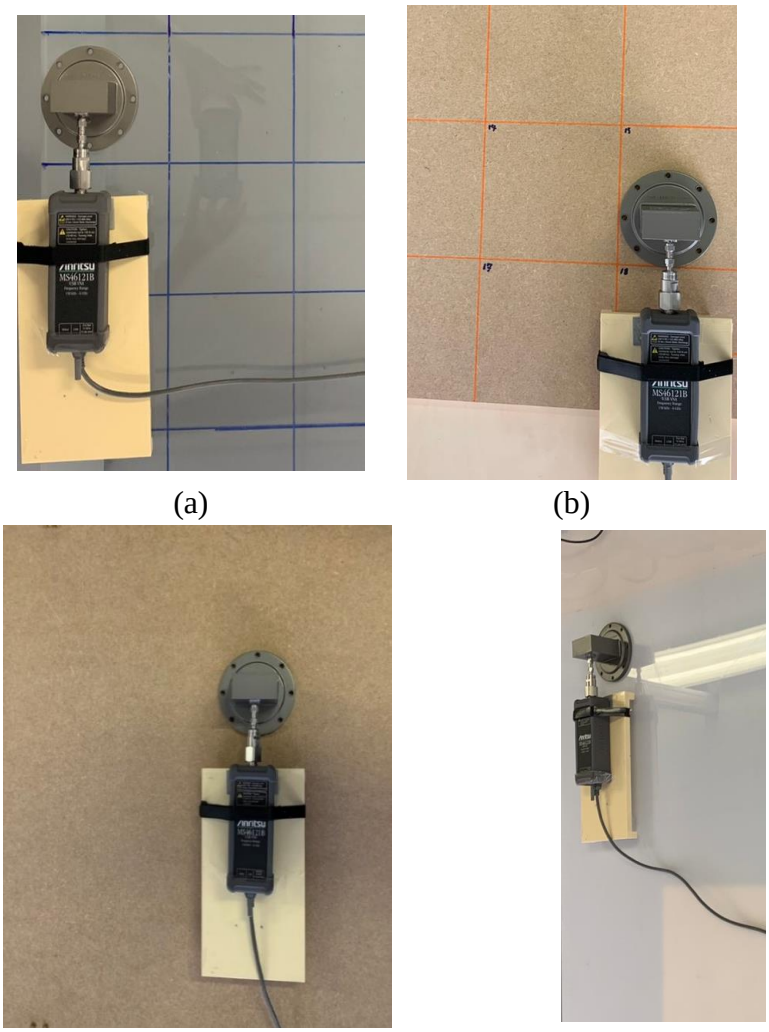


Figure 4.30 Experimental system for contact microwave sensing. Different planar MUT are in contact with the OERW: (a) glass; (b) wood; (c) wood; (d) Plexiglas.

Figure 4.31 illustrates the recorded $S_{11}$magnitude and phase-shift) of some wood samples with different thicknesses. It is worth noting that each wood sample exhibits unique characteristics in terms of magnitude and phase-shift. These differences are mainly related to the varying thicknesses of the wood samples.

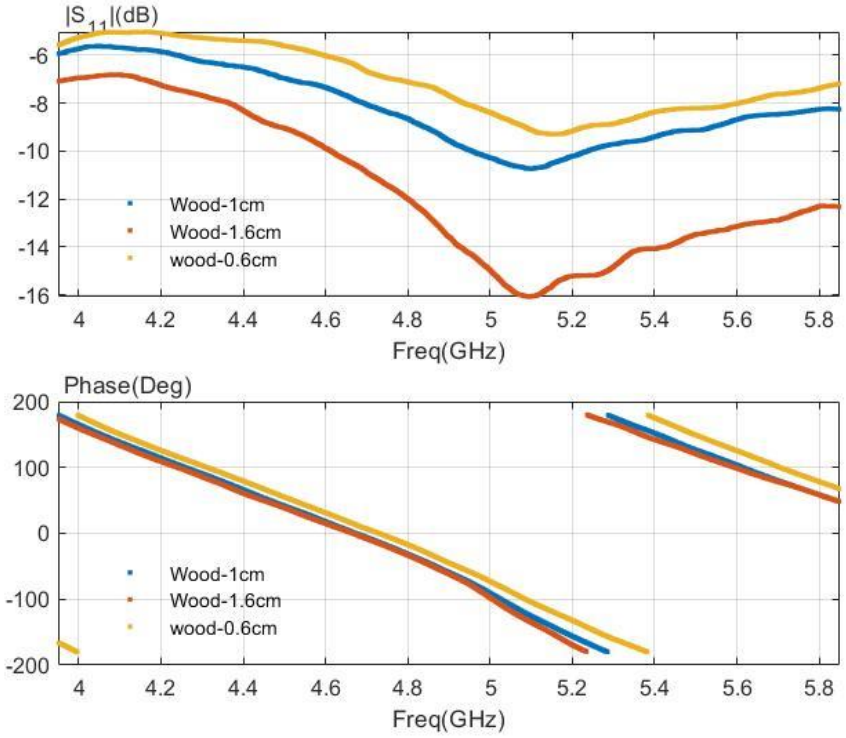


Figure 4.31 Measured $S_{11}$ of wood samples with different thicknesses using the OERW.

Figure 4.32 illustrates the recorded $S_{11}$magnitude and phase-shift) of some plexiglas samples with different thicknesses: 40 mm and 20 mm. The two signals show similarity in their $S_{11}$.

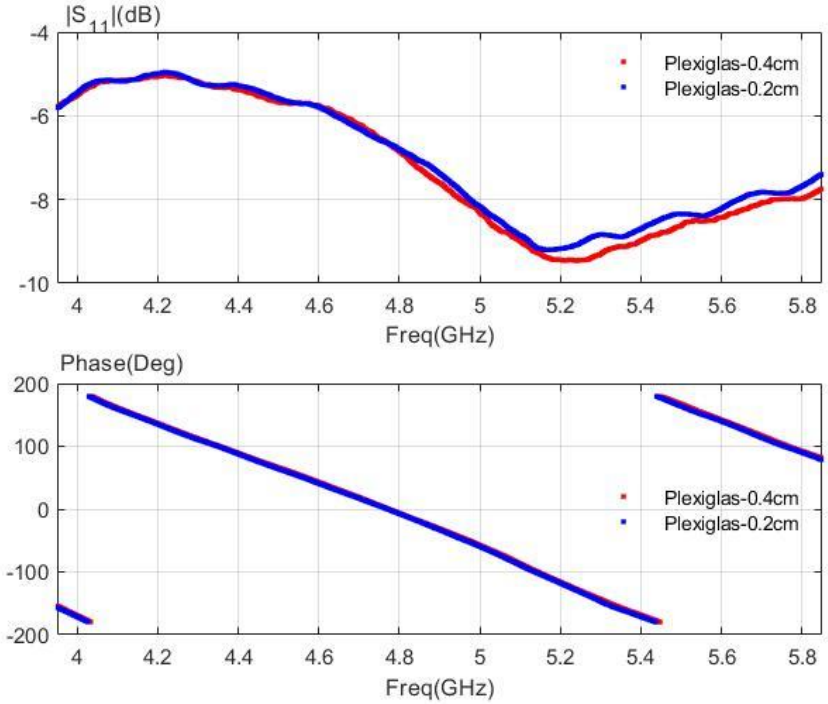


Figure 4.32 Measured $S_{11}$ of some plexiglas samples with different thicknesses using the OERW.

Figure 4.33 illustrates the recorded $S_{11}$magnitude and phase-shift) of some glass samples with different thicknesses: 20, 40, 50 and 90 mm. As the thickness increase the $S_{11}$of glass differs from other glass samples.

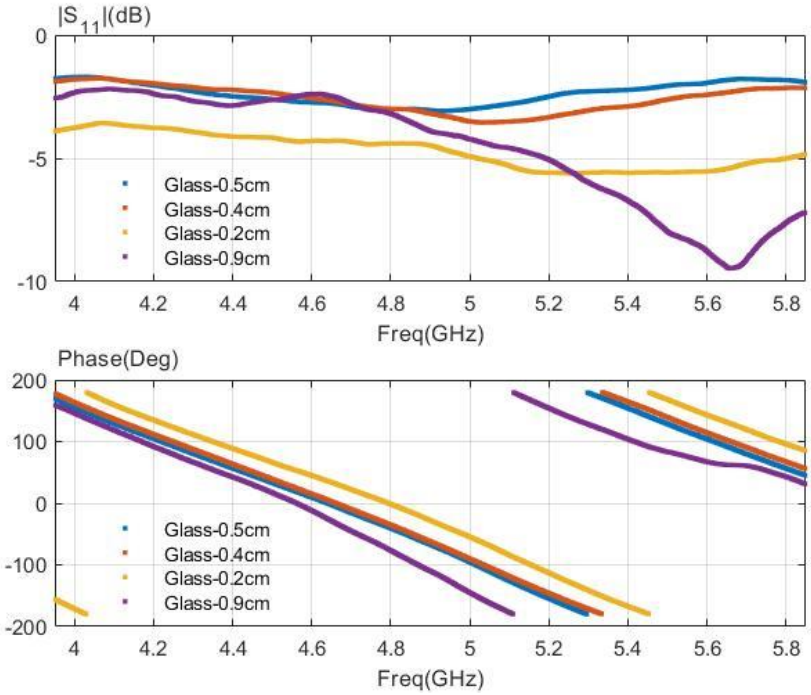


Figure 4.33 Measured $S_{11}$ of some glass samples with different thicknesses using the OERW.

Figure 4.34 illustrates the $S_{11}$of different materials characterized by closely similar thicknesses. Each material presents distinct $S_{11}$ signatures, but even for identical materials, these signatures change as thickness varies, as demonstrated by previous results. Thus, it is challenging to characterize these materials with analytical models. This highlights the importance of using ML models to classify and characterize these materials, regardless their thicknesses; due to the robust capabilities of ML models in handling complex and evolving patterns in the data.

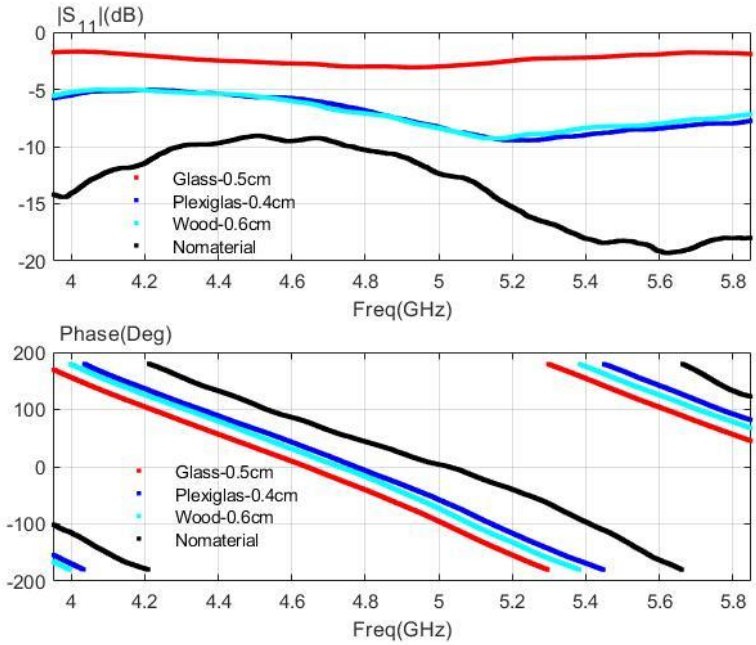


Figure 4.34 Measured $S_{11}$ of some samples types using the OERW.

### 4.5.5. Supervised learning for material classification

Material characterization, involving the classification of various material types, is executed following two distinct scenarios. In the first scenario, we fed the ML algorithms with the magnitude and phase-shift of $S_{11}$. Subsequently, we apply PCA to extract the most representative PCA components, which will be used as the input for the ML models. PCA identifies a set of orthogonal projection vectors. These projected components preserve the most essential information from the original samples, while simultaneously reducing variable correlations and improving the signal-to-noise ratio.

PCA was applied following the standardization of the data. In figure 4.35, the results of the PCA analysis (variance and cumulative variance) for the first 10 principal components on the phase-shift data are presented. It is shown that the first two principal components account for more than 75% of the variance. Furthermore, the first three and first six principal components collectively explain over 90% and 95%, respectively, of the total variance present in the original dataset

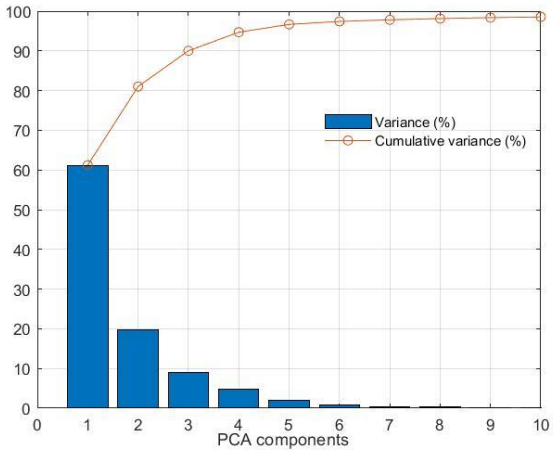


Figure 4.35 Variance and cumulative variance (%) of the first 10 PCA components applied of the phase-shift data.

Specifically, we retain PCA components that contribute to more than 90% of the total variance in the magnitude and phase-shift data. Following the feature extraction, the resultant datasets were delivered to the classification stage. Five well-known supervised ML models are used: RF, DTC and SVM with a three kernel functions: linear, polynomial and RBF. Each kernel can be fitted to the corresponding model by adjusting the corresponding parameters: cost (C) and gamma ($\gamma$). These parameters were optimized using the grid search method in order to maximize the accuracy rates.

## 4.5.6. Results and performance evaluation

The objective is to precisely determine, from the collected data, whether the MUT is wood, glass, plexiglas, or if there is no MUT present. To achieve this, the ML models are first trained and evaluated using 617 measurements drawn from the first group's (CV subset). Subsequently, these trained models are evaluated on unseen data, comprising 270 measurements from the second group.

The table 4.13 offers a comparison of two distinct features representations, namely magnitude and phase-shift of $S_{11}$, and the PCA on magnitude and phase-shift data using different performance evaluation.

| | **Magnitude & Phase-shift** | | **PCA (Magnitude & Phase-shift)** | |
|---|---|---|---|---|
| **Data Subset** | CV subset | Unseen subset | CV subset | Unseen subset |
| **Accuracy (%)** | 100 | 99 .6 | 100 | 97.77 |
| **Sensitivity (%)** | 100 | 99 .6 | 100 | 99.60 |
| **Precision (%)** | 100 | 99 .6 | 100 | 97.77 |
| **F1_score (%)** | 100 | 99 .6 | 100 | 98.6 |
| **Best Classifiers** | DCT – RF | | RF | |

Table 4.13 Performance of the best ML classifiers trained using: magnitude and phase-shift of $S_{11}$ then their PCA components.

The Random Forest (RF) classifier consistently outperforms others, achieving consistently high accuracy scores across different data subsets.

Regarding **accuracy**, both the complete data (magnitude and phase-shift) and PCA (magnitude and phase-shift) representations achieve a perfect score of 100% on the CV subset, demonstrating their effectiveness in accurately classifying the data. However, on the Testing subset (unseen data), there is a slight drop in accuracy compared to the CV subset, with 99.6% and 97.7% accuracy for the magnitude and phase-shift data and PCA features, respectively.
**Sensitivity and precision**, follow a similar pattern. Both the magnitude and phase-shift data and PCA features achieve values of 100% on the CV subset and maintain high scores on the unseen subset.
**F1_score**, which balances precision and sensitivity, further confirmed the robust performance of the magnitude and phase-shift data and PCA features, with near-perfect scores on CV subsets.

In conclusion, this analysis underscores the importance of selecting the right feature representation and classifier for a given task. Employing PCA features for material classification offers the advantage of dimensionality reduction, resulting in faster and less computationally classification, while maintaining high accuracy. Furthermore, it highlights the effectiveness of integrating OERW with ML techniques for material characterization.

## 4.6. DL-based open-ended rectangular waveguide for defects detection

Previous sections have introduced two intelligent MNDT&E techniques for material characterization.

In this section, we shift our focus towards applying the MNDT&E technique to detect defects within the MUT and subsequently monitor its health. The proposed technique relies on using an OERW along with the implementation of a DL model to detect millimeter-sized cracks in the MUT. To accomplish this objective, we measure the $S_{11}$ parameters of both defective and defect-free materials. Subsequently, the collected data further analyzed using 1D convolutional neural network (1D-CNN) model.

In the following sections, we provide detailed explanation on the proposed methodology, the experimental setup, the data acquisition process, the DL model employed, and finally, the presentation of results, along with performance evaluation.

### 4.6.1. Methodology

The proposed methodology integrates the advantages of the OERW and 1D-CNN model. The 1D-CNN serves as a robust data system for automatic feature extraction, enabling the establishment of both linear and non-linear relationships between input and output data. Its capacity to learn these relationships directly from the modeled data allows it to effectively

address multi-parameter challenges, including variations in MUT thickness, defect sizes, and defect depths, all of which influence the $S_{11}$characteristics.

The process consists of three main steps: (1) data acquisition, (2) data preprocessing, (3) training and evaluating the DL classifier. The first step concerns the construction of a new dataset containing labeled data, which should include both defect-free and defective samples. The OERW system provides precise measurement of $S_{11}$across a frequency range varying from 3.95 to 5.85 GHz with a step of 2.2MHz. The data are obtained from various wooden samples, including some defect-free and others intentionally modified to introduce defects.

Following data acquisition, the dataset is divided into training and testing subsets. This division is performed using the 5-fold CV approach. According to this approach, each fold, the data is randomly divided into five separate groups. One of these groups is designated for testing, while the remaining data is used for training. The subsequent step is to design the architecture of the 1D-CNN. This requires decisions regarding:

- the number of convolutional layers,
- the quantity of filters within each layer,
- the size of the filter kernels,
- the number of pooling layer,
- the number of fully connected layer.

The selection of these architectural features is an iterative process and take rounds of experimentation to identify the optimal architecture. Model performance is then evaluated at each CV fold, using five metrics: accuracy, sensitivity, precision, F1_score and computer training time. The averages across all folds are then recorded.

To determine the most effective approach for detecting defects in materials, we employ two distinct input data configurations when training and evaluating our 1D-CNN model. First, we use the magnitude and phase phase-shift data as input for the model. This means that the model receives information regarding the magnitude and phase-shift of the measured $S_{11}$of the MUT. Then, in a separate experiment, we employ the real and imaginary data as inputs for the same 1D-CNN model. Here, the model processes the real and imaginary components of the measured $S_{11}$of the MUT. By comparing the performance of the 1D-CNN model with these two different input data configurations, we can assess which approach is more effective at defects detection in the materials.

### 4.6.2. Materials and samples preparation

In this study, various wooden samples of different thicknesses are used to test and validate the proposed technique. We initially measure the $S_{11}$ parameter for defect free samples and subsequently, we induce defects in selected samples to evaluate their corresponding $S_{11}$values and simulate real-world scenarios. To achieve this, we intentionally introduce a diverse range of surface cracks into certain wooden materials, with depths ranging from 1 mm to 10 mm. These cracks were shaped into three distinct forms: circles, rectangles, and triangles, with their specific dimensions provided in the table 4.14. In total, there are 53 defects resulting from the diverse combinations.

| Defects form | Radius (mm) | Depth (mm) | Length (mm) |
|---|---|---|---|
| **Circle** | {2 ; 6 ; 10 ; 20 ; 30} | {1 ; 3 ; 5 ; 8; 10} | - |
| **Triangle** | - | {1; 3; 5; 8} | {3; 30} |
| **Rectangle** | - | {1; 2; 3; 5} | {60} |

Table 4.14 Dimensions of different cracks intentionally made in the MUT.

Figure 4.36 displays a range of intentionally introduced cracks in wooden material. These defects exclusively present as surface cracks, each distinguished by unique shape, depths and dimensions.

(a) Circular cracks

(b) Triangular cracks

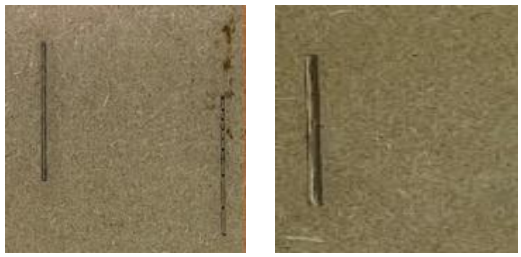

(c) Rectangular cracks

Figure 4.36 Intentionally introduced cracks of varied types and dimensions in wooden material.

Our main aim was to reproduce realistic defects commonly found in materials, encompassing a wide range of shapes. In this study, we initially chose wooden materials to validate the

proposed technique. However, it is important to note that this method can be extended to encompass a wide range of material types and adapt to various crack configurations.

### 4.6.3. Experimental setup

The measurement system is built up with the OERW [ATM® P/N 187-251-6] with the VNA [Anritsu® MS46121B MS46121B]. The waveguide is connected to the input port of the VNA using N-to- SMA coaxial transition and SMA-to-waveguide transition. The measurement operates within the frequency covered by the waveguide between 3.95 and 5.85 GHz with a step of 2.2MHz. The measurements configuration is depicted in table 4.15. Before starting the measurement, the VNA is calibrated using the same calibration kit: TOSLKF50A-43.5 from Anritsu®) presented in the previous sections.

| | |
|---|---|
| **Frequency range (GHz)** | 3.95 – 5.85 |
| **IFBW (Hz)** | 100 |
| **Number of points** | 863 |

Table 4.15 $S_{11}$ measurement configuration using the waveguide and the VNA.

### 4.6.4. Acquisition and Construction of an Original dataset

The data collection process occurred over two days. Each day, we reconstructed the experimental setup and conducted measurements in an empty space to compare $S_{11}$ reflection coefficients, ensuring complete measurement repeatability. In our experimental setup, we began by scanning the MUT without defects, and subsequently, we scanned the MUT containing surface cracks.

The experimental setup involves the direct contact of the system with the MUT as presented in the figure 4.37. The measurement system sends electromagnetic signals, in the frequency range between 3.95 and 5.85 GHz, to the MUT and collects the reflection coefficient $S_{11}$. The information reflected back is valuable since it reveals details about the MUT. Initially, the system is used to inspect wooden materials that are known to be defect-free. Subsequently, the setup involves the scanning of materials that have been intentionally prepared with defects. The OERW is placed directly over the defects, with the assumption that only one defect is scanned at a time. This controlled testing approach enables the evaluation of the system's performance in identifying and characterizing defects in a precise and targeted manner.

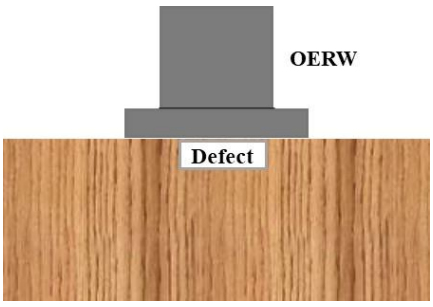


Figure 4.37 Schematic drawing of an OERW scanning a wooden plate with surface defect.

The results indicate a distribution of measurements as follows: 85 measurements without defects and 53 measurements with defects of various shapes. These measurements are randomly mixed on single dataset. Figure 4.38 illustrates the measured $S_{11}$ of a wooden sample with and without defects:

- defect 1 has rectangular shape (depth: 2 mm; length: 60 mm).
- defect 2 has circular shape (depth: 3 mm; radius: 2 mm).
- defect 3 has triangular shape (depth: 3 mm, length: 3mm).

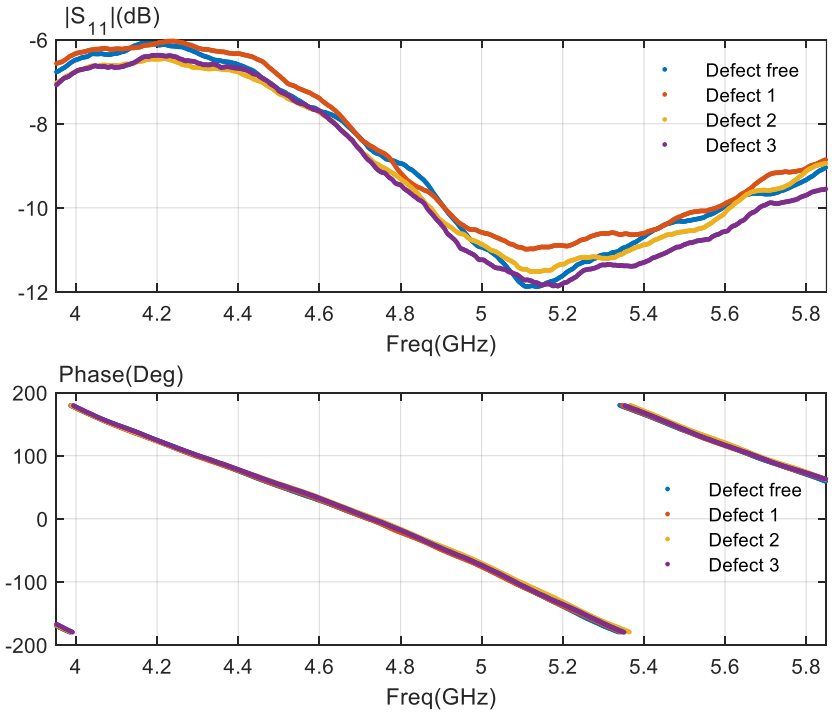


Figure 4.38 Sample 1 : measured $S_{11}$ using the OERW.

Figure 4.39 illustrates the measured $S_{11}$of another wooden sample with and without defects:

- defect 1 has rectangular shape (depth: 2 mm; length: 60 mm).
- defect 2 has triangular shape (depth: 5 mm; length: 3mm).
- defect 3 has circular shape (depth: 3 mm; radius: 2 mm).

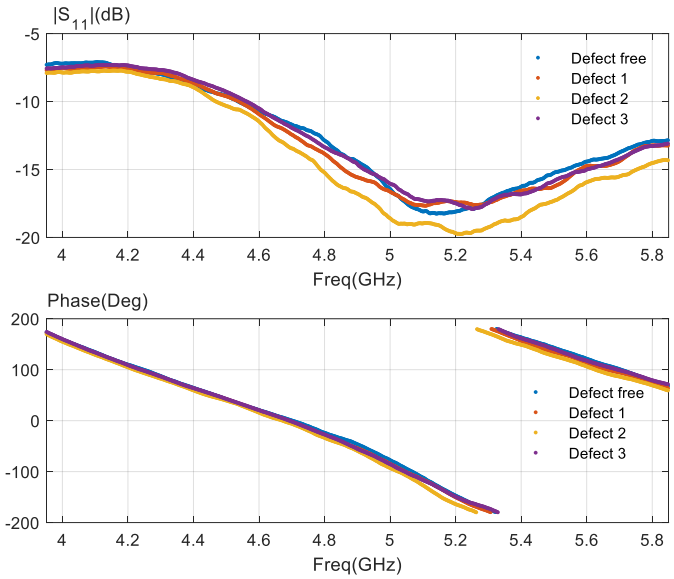


Figure 4.39 Sample 2 : measured $S_{11}$ using the OERW.

Given the large number of measurements, we have chosen to showcase just two samples. The $S_{11}$measurements of the defects and defect-free scenarios display a degree of similarity as presented in the figures 4.40 and 4.41. This similarity presents a significant challenge when attempting to construct analytical models for defect detection. This highlights the usefulness of using DL models, as they can effectively serve as valuable tools for understanding and analyzing these measurements.

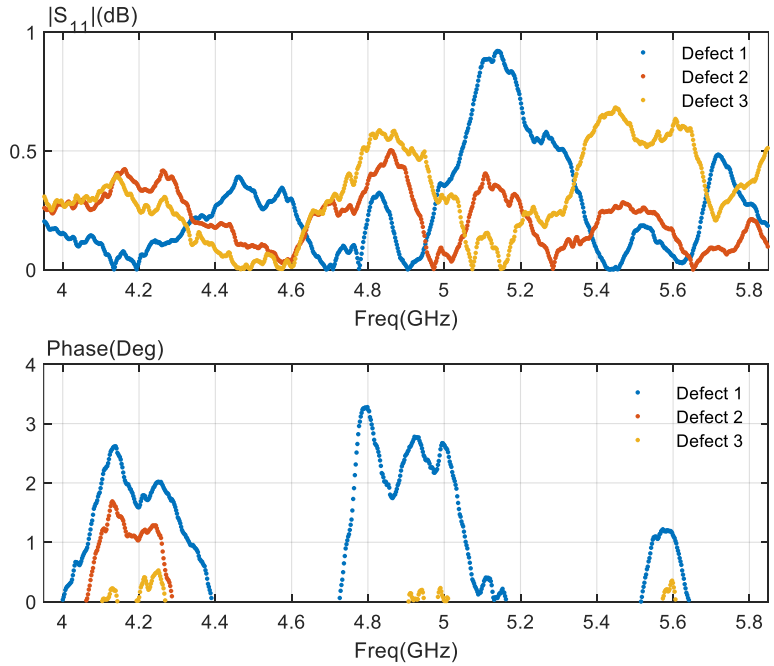


Figure 4.40 Sample 1 - Difference between measured $S_{11}$ of defect-free sample and each defect

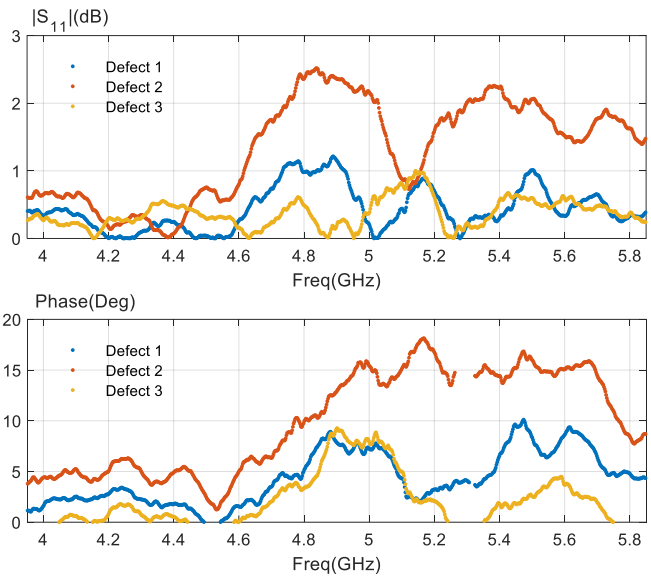


Figure 4.41 Sample 2 - Difference between measured $S_{11}$ of defect-free sample and each defect.

## 4.6.5. 1D-CNN

The 1D-CNN processes one dimensional signals and offers good real-time performance. For the classification targets, the structure of the 1D-CNN is typically divided into the input layer, feature-extraction part and the classification part. The feature extraction part is typically composed of convolutional layers and pooling layers while the classification part consists of fully connected layers.

The 1D-CNN architecture proposed in this study is illustrated in the figure 4.42. This structure comprises several layers, including two one-dimensional convolutional layers (Conv1D), one max-pooling layer (MaxPool1D), and a fully connected multilayer consisting of one hidden layer and a sigmoid output layer. The input and output shapes, along with the details of each layer, are presented in the table 4.16.

The $S_{11}$measurements represented as a matrix with dimensions (863, 2), serve as the input data for the model. The feature extraction process begins with the first conv1D layer. This initial layer operates by applying a set of 32 filters, each having a size of 5. The filters perform convolution on the input data, systematically extracting the most relevant and significant features, which are commonly referred to as feature maps. Subsequently, the second conv1D layer is introduced, further enhancing the complexity and abstraction of the features initially learned from the first layer. In this layer, 64 filters each with a size of 5, are used. This layer's purpose is to capture more complex patterns and relationships within the input data, allowing the model to recognize more detailed characteristics. It's important to note that in CNNs, the weights of these convolutional kernels are learned automatically during the training process. These weight adjustments occur through backpropagation and gradient descent, aiming to minimize the loss function and enhance the network's efficiency in its designated task. This iterative learning process empowers the network to adapt and become effective at feature extraction and pattern recognition.

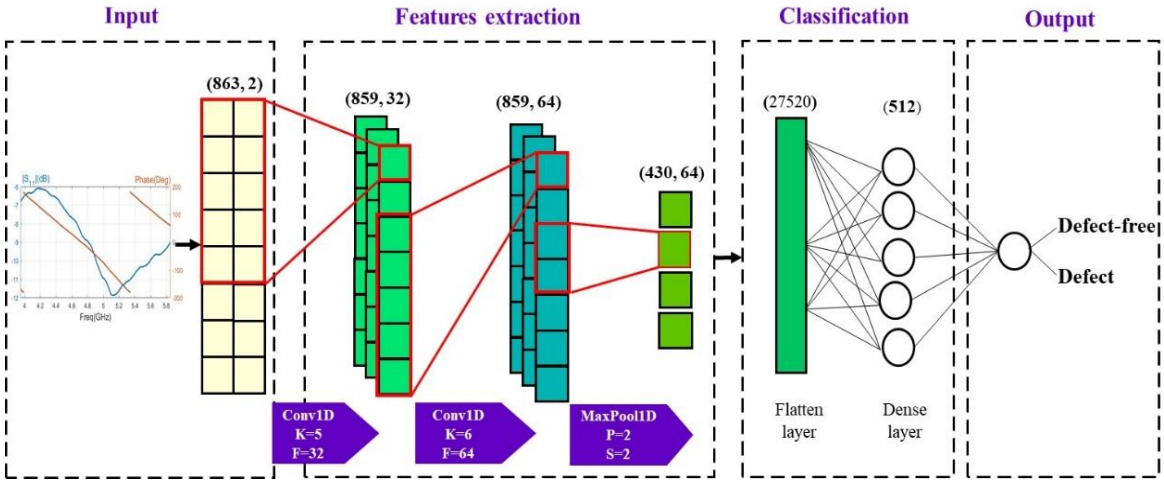


Figure 4.42 Block diagram of the proposed 1D-CNN architecture. K: filter number; F: kernel size; P: pooling size; S: strides.

To enhance the convolutional process, we introduce a maxPool1D layer that selects the maximum value from each 2-unit pool with a stride of 2, moving the selection window two positions at a time across the data to retain the most significant features. This helps to make the model more robust to noise, effectively eliminating overfitting, reducing computation time, and increasing generalization performance. Additionally, a dropout layer is introduced before the maxPool1D layer to randomly deactivate some neurons during training, thus aiding in overfitting prevention.

| Layer | Parameters | Input | Output |
|---|---|---|---|
| **Input** | $S_{11}$ (magnitude & phase-shift) or $S_{11}$ (real & imaginary) | (863 , 2) | (863 , 2) |
| **Conv1D** | F: 32; K:5<br>activation function: RELU | (863 , 2) | (859 , 32) |
| **Conv1D** | F: 64; K:5<br>activation function: RELU | (859 , 32) | (859 , 64) |
| **MaxPool1D** | Dropout = 0.5<br>P: 2; S: 2 | (859 , 32) | (430 , 64) |
| **Flatten** | - | (430 , 64) | (27520) |
| **Fully connected layers** | 512<br>activation function: RELU | (27520) | (512) |
| **Output** | 1<br>activation function: SIGMOID | (512) | (1) |

Table 4.16 Architecture of the proposed 1D-CNN with the shape of the input and output of each layer.

To prepare data to the classification phase, we introduce the flatten layer. It converts the 2D feature map into a 1D vector, a necessary step before feeding the data into the fully connected layer. This helps to simplify the output of the convolutional layer, resulting in reduced computational complexity and overall improvement in the model's performance. The data is then directed to a fully connected layers (dense layers) consisted of two layers. In these layers, each neuron is connected to every neuron in the previous layer. The first dense layer consists of 512 neurons, while the second dense layer contains a single neuron with a sigmoid activation function, specifically chosen for binary classification output. The output of the model is a single value between 0 and 1, if the output is greater than or equal to 0.5, the network predicts class 1 (defective sample); if it's less than 0.5, it predicts class 0 (defect free sample).

### 4.6.6. Results and performance evaluation

In this section, we focus on the evaluation of the performance of the proposed 1D-CNN in defects detection in wooden samples. The results indicate a distribution of measurements as follows: 85 measurements without defects and 53 measurements with defects of various shapes. These measurements are mixed randomly in one dataset and divided following the 5-CV fold approach to train and validate the 1D-CNN model.

Table 4.17 illustrates the results obtained from the 1D-CNN model for classifying the measured $S_{11}$ data into defective and defect-free samples.

| | **Magnitude & Phase** | **Real & Imaginary** |
|---|---|---|
| **Accuracy (%)** | 82.05±2.69 | 98.33± 3.33 |
| **Sensitivity (%)** | 82.04±2.69 | 98.33±3.33 |
| **Precision (%)** | 82.60 ± 3.65 | 98.32 ± 3.35 |
| **F1_score (%)** | 81.84 ± 3.37 | 98.31 ±3.38 |
| **Computational training time (sec)** | 463.34 | 466.61 |

Table 4.17 Results of the performance results of the proposed 1D-CNN using two types of input data.

The evaluation metrics provide an overview of the model's capabilities. In terms of accuracy, the 1D-CNN model achieved 82.05%±2.69 accuracy when considering magnitude and phase data, and an even higher accuracy 98.33%±3.33 when considering real and imaginary components.

Furthermore, the sensitivity, precision and the F1_score metrics demonstrate consistency with accuracy. This metrics achieve around 82% for magnitude and phase data and 98% for real and imaginary data.

Additionally, the computational training time for the 1D-CNN model taking approximately 463.34 seconds for magnitude and phase data and slightly longer at 466.61 seconds for real and imaginary data.

The figure 4.43 illustrates the training and validation accuracy of the proposed 1D-CNN model, which uses the magnitude and phase-shift of measured$S_{11}$as input data. These accuracy results are derived from the final CV fold. In the graphs, a noticeable early convergence is observed, typically occurring around the 40th epoch. The training accuracy rapidly reaches a high value, approximately 98%, indicating that the model fits the training data well. However, the validation accuracy is slightly lower, stabilizing at around 85%. The observed difference between the training and validation accuracy indicates that the model may be overfitting the training data. This is particularly relevant because the dataset in use is relatively small. In such cases, when the model has limited data to learn from, it can memorize the specific details and noise within the training set. This focused learning can limit the model's ability to generalize to new, unseen data, and this limitation becomes evident in the form of lower validation accuracy.

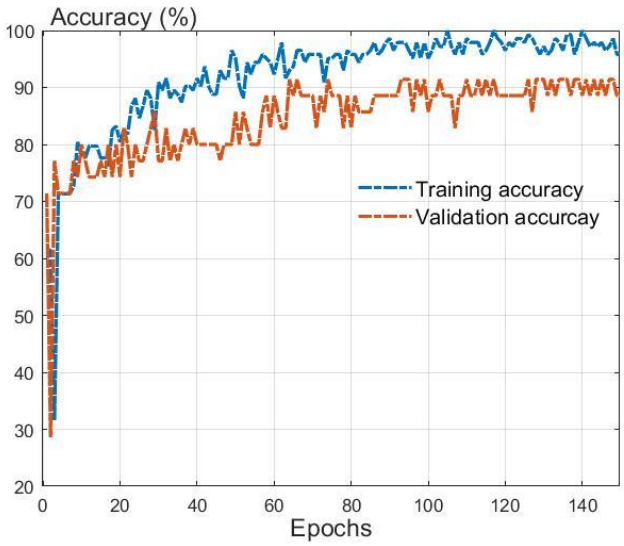


Figure 4.43 Training and validation accuracy for the proposed 1D-CNN model using magnitude and phase components of the measured $S_{11}$.

The figure 4.44 introduces the training and validation accuracy of the 1D-CNN model proposed for processing the complex components (real and imaginary) of the measured $S_{11}$ data. The accuracy results are derived from the final CV fold. The validation accuracy follows the training accuracy and starts to converge after approximately 70 epochs. This convergence results in a notable increase in accuracy, achieving a rate of approximately 98%. The results demonstrate the effectiveness of the proposed technique, suggesting that the complex components are more adaptable than the magnitude and phase-shift components in capturing and representing the characteristics that distinguish between defect and defect-free samples.

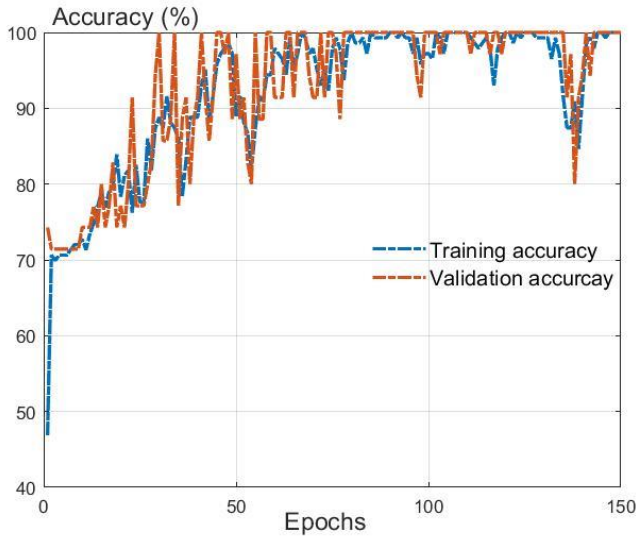


Figure 4.44 Training and validation accuracy for the proposed 1D-CNN model using the complex components of the measured $S_{11}$.

These results highlight the efficiency of the 1D-CNN model, particularly when classifying $S_{11}$ data using real and imaginary components. The metrics show that the real and imaginary data present a stronger representation of both defective and defect-free samples, resulting in superior performance. However, our study was limited by the available number of samples and in controlled laboratory conditions.

In order to enhance the robustness and versatility of this model, a broader range of measurements is essential. This can be achieved by introducing various samples and various types of cracks. These enhancements will further play a key role in improving the model's classification capabilities, enabling it to effectively handle complex scenarios. This includes the detection of subsurface defects and its applicability to different types of materials.

## 4.7. Free space radar vs. OERW: A Comparative study

This study proposed two MNDT&E microwave techniques for non-destructive material characterization and defect detection based on: free space radar using a horn antenna and open-ended rectangular waveguide in monostatic setup. Each technique has its own advantages and drawbacks in terms of spatial resolution and stand-off distance (radar-MUT).

The main advantage of free-space radar technique is its ability to operate without the need for physical contact. In fact, the radar system inserted perpendicularly to the MUT, transmits electromagnetic waves and receives reflected signals through open space. The flexibility in the stand-off distance is one of the advantages of monostatic free-space radar. However, it presents challenges when the MUT is in the near-field, where the radar response becomes complex due to multiple reflections and interference patterns, making interpretation more challenging. Conversely, in the far field, diffraction effects caused by the radar's surroundings lead to a reduction in spatial resolution.

On the other hand, the OERW offers a significant advantage through its high measurement precision, due to its metallic guide designed to transmit and receive electromagnetic waves. This attribute makes it particularly well-suited for applications requiring high-resolution inspections. It excels in detecting small defects and providing fine details about the tested material. However, it is important to note that the effectiveness of the OERW is limited to contact setup. For optimal high-resolution performance, the OERW must be positioned very close to the MUT.

In summary, free space radar and open-ended rectangular waveguide are both effective techniques for material characterization and defect detection. Each method will depend on the specific requirements of the application. For example, if high spatial resolution is required then an open-ended rectangular waveguide may be the best option. Otherwise, if the material to be characterized is at a distance, then free space radar may be the best option.

In a future work, the aim is to integrate the microwave instrumentations into an automated system designed to regulate and adapt the distance. This automation allows to take the benefits of integrating the two techniques. In the initial phase-shift of our setup, we employ a monostatic free space radar to characterize the MUT from a predefined distance. This initial distance allows to conduct a fast and non-destructive inspection of the MUT. In cases where we identify any anomalies or areas of interest, we then reduce the distance between the radar system and the MUT. This brings the radar system in close proximity to the MUT. Subsequently, we transition to use a waveguide system for the purpose of conducting highly precise and accurate inspections. This dual-stage approach enables to first perform a quick and non-invasive assessment using the free space radar, and then, when necessary, employ the waveguide system for detailed inspection of the MUT.

## 4.8. Conclusion

This chapter presented three intelligent MNDT&E techniques: two focused on materials characterization, and one dedicated to defects detection in this material. These approaches combine the strengths of microwave technology to capture the reflection coefficient of the MUT, with DL and ML models to efficiently characterize materials and identify defects within them. The proposed techniques offer many advantages: they enable nondestructive and fast inspections, while also being compact, having a low error rate, offering contactless and easy-to-work operation, demonstrating versatility across various applications, and effectively handling complex materials, regardless of their thicknesses.

In each technique, a new and original dataset is constructed, resulting in the creation of three new datasets within this study. The first technique relied on a monostatic free-space radar operating at frequencies ranging between 3.95 and 5.85 GHz, using five ML models (DCT, RF, SVM with three different kernels: linear, RBF and polynomial) to characterize materials from a distance. It achieved a 99% accuracy in controlled laboratory settings and maintained a 95% accuracy even in more challenging and realistic conditions. The second technique relied on using an OERW operating at frequencies ranging between 3.95 and 5.85 GHz, applying the same five ML models to characterize materials in direct contact to the system. This technique provided higher accuracy, achieving 100% accuracy under controlled laboratory conditions and maintaining 99.6% accuracy level in more challenging and realistic scenarios. The third

technique was specifically designed for detecting defects within materials. It relied on using the OERW with frequencies ranging from 3.95 to 5.85 GHz and with a DL model (1D-CNN). The accuracy reached 82% when using both the magnitude and phase-shift of the measured $S_{11}$ for training the DL model, and it increased to 98% when employing the complex components (real and imaginary part) of the measured $S_{11}$.

The research has achieved significant findings, demonstrating the effectiveness of the proposed techniques. However, in the next chapter, we present a feasibility study using a six-port reflectometer designed for operation in the millimeter-wave range. This addition aims to further strengthen the robustness and versatility of high frequency characterization techniques.

# Chapter 5. Feasibility study of a millimeter radar based on six-port technology

**Chapter outlines**

## 5.1. Introduction

Microwave sensing based on VNA tools has become an essential tool for non-destructive testing and evaluation in a wide range of industrial and scientific fields. In the previous chapters, we presented promising results in the field of microwave-based material characterization and defect detection. These techniques combined with ML and DL algorithms, have proven effective in assessing the properties of various materials and identifying potential defects. Nevertheless, the application of the VNA also presents a series of challenges, particularly when faced with harsh environmental conditions. These challenges include factors such as extreme temperature variations and high levels of electromagnetic interference.

Six-port technology is a promising alternative to VNAs (conventional heterodyne architecture) for microwave sensing in harsh environments [219], offering the power to enhance microwave sensing capabilities [220-224]. The various advantages it provides include:

- Immunity to noise and interference: Six-port technology is designed to be immune to noise and interference from other sources. This is because they use a differential measurement technique that cancels out common noise and interference signals.
- Versatility in temperature and environment: This technique operates in a wide range of temperatures and environmental conditions.
- Compact, lightweight, and simple design: The simple design of six-port systems makes them ideally suited to monolithic implementation. As well, by integrating all essential components on a single substrate, interconnection issues are minimized, resulting in a reduction in the size and weight of the system as a whole, making them easier to use in a variety of applications.
- High accuracy: This technology provides high precision, enabling the measurement of distances down to micrometers and velocities down to millimeters per second.
- Ultra-low power consumption and cost efficiency
- Industrial automation: Six-port technology can be used to measure the position of objects on conveyor belts, to detect the presence of objects, and to monitor the condition of machinery.
- Millimeter-wave operation: As the size is directly related to the operation wavelength, millimeter-wave frequency operation is preferred to reduce the circuit size.

Six-port technology was first introduced by Engen and Hoer in 1977 [225]. Significant progress has been achieved in recent years in the field of six-port technology, marked by advancements including novel circuit designs and the development of new signal processing algorithms. As a result, the technology has been widely adopted in a diverse range of applications [226-228], covering telecommunications, medical diagnostics [229], metrology [230], remote sensing and materials characterization [231-239].

In this context, we introduce a metallic waveguide six-port reflectometer designed for operation at 60 GHz. The metallic waveguide technology provides isolation between nearby signals and presents immunity to environmental variations [238]-[240]. The purpose is to evaluate the accuracy and efficiency of the system in two specific applications: sub-millimeter distance measurements and its use as an IQ demodulator. In the first application, we integrate the

proposed six-port reflectometer with a horn antenna to create a non-contact free-space measurement technique, designed for precise sub-millimeter distance measurements. In the second scenario, we introduce an IQ demodulator architecture for accurate phase-shift measurements.

The remaining chapter is organized as follows. The first section describes the fundamental principle of the six-port reflectometer and provides a detailed mathematical analysis of its behavior. Following this, we introduce the proposed metallic six-port reflectometry and discuss our various applications along with experimental results demonstrating the performance of the proposed system.

## 5.2. Six-port principle

### 5.2.1. Definition

The six-port is a passive structure based on the interferometric principle used in microwave and millimeter wave applications for the precise measurement of reflection coefficients of the MUT, at a given frequency. The term six-port directly corresponds to the structure itself, which consists of two input ports and four output ports. The reference signal is fed into the six-port network through port 1, while the MUT, for which we aim to determine the reflection coefficient, is connected to port 2. The remaining four ports are connected to power detectors (figure 5.1). Power measurements followed by mathematical data processing enable the measurement of the reflection coefficient.

Therefore, the performance of the six-port reflectometer is closely related to both its hardware characteristics and calibration modeling adopted. For effective penetration of this technology in industrial applications, and a full understanding of its capabilities and limitations, dedicated test set-ups are essential.

### 5.2.2. Equations of the six-port reflectometer

The six-port reflectometer is a device based only on power measurements followed by mathematical processing of the data to obtain measurements of the reflection coefficients. In this section, we present the general architecture of a six-port system along with the equations controlling its behavior. The schematic diagram is illustrated the graph given in figure 5.1.

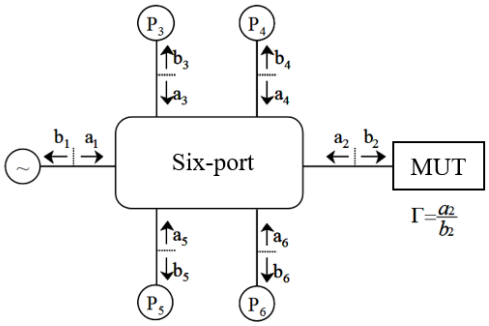


Figure 5.1 Block diagram of six-port reflectometer [95].

The reference microwave signal feeds the six-port network on port 1. The MUT with reflection coefficient $\Gamma$, to be determined, is connected to port 2. The remaining four channels are connected to power detectors $D_3$to $D_6$. After calibrating the device with fully or partially known loads, it is possible to determine the value of the $\Gamma$ coefficient from the four measured powers $P_3$ to $P_6$.

The state of the six-port is determined by twelve pseudo-waves incident $a_i$ and emerging $b_i$ (i = 1,...6). These pseudo-waves are coupled to the S-parameters of the six-port network by the following six equations:

$$b_i = \sum_{j=1}^{6} S_{ij} a_j \text{ with} i = 1, \dots, 6 \tag{5.1}$$

Since, the ports 3 to 6 are connected to detectors $D_3$to $D_6$, we can add four additional constraints whose equations are given by:

$$a_i = b_i \Gamma_i \tag{5.2}$$

where $\Gamma_i$ represents the reflection coefficient of the detector connected to port i (i = 3,...,6)

The powers measured at the $D_i$ detectors considered to be perfectly matched to the six-port junction are given by the equations:

$$P_i = |b_i|^2 = |A_i a_2 + B_i b_2|^2 \text{ with } i = 3,4,5,6 \tag{5.3}$$

where $A_i$ and $B_i$ are complex quantities characteristic of the reflectometer and dependent only on S-parameters of the six-port network and the reflection coefficients of the detectors.

By introducing the reflection coefficient of the MUT to be measured $= \frac{a_2}{b_2}$ ; we can write the equation (5.3) as follows:

$$P_i = |A_i|^2 |b_2|^2 \left| \Gamma + \frac{B_i}{A_i} \right|^2 \text{ with } i = 3, \dots, 6 \tag{5.4}$$

Six-port reflectometers are often designed in such a way that one of the detectors called reference detector (here denoted as $D_3$), depends only on the $b_2$ wave incident on the MUT. So, it is possible to write the equation (5.4) as follows:

$$P_3 = |B_3|^2 |b_2|^2 |d\Gamma + 1|^2 \text{ with } d = \frac{A_3}{B_3} \tag{5.5}$$

For ideal system, the directivity $d = 0$.

By normalizing the power detected at ports 4, 5 and 6 to that detected at port 3, the measurements become independent of the power delivered by the generator. This results in the following system of equations:

$$P_i = \frac{P_i}{P_3} = C_i \left| \frac{\Gamma - q_i}{d\Gamma + 1} \right|^2 \text{ with } i = 4,5,6 \tag{5.6}$$

with $C_i = \left| \frac{A_i}{A_3} \right|^2$ and $q_i = \frac{-B_i}{A_i}$ .

To establish the relationship between the measured power and the reflection coefficient $\Gamma$ of the MUT, a calibration step using known load is required [100-101]-[241]-[242]. This step involves the calculation of two sets of parameters: $C_i$ and $q_i$, these parameters are named calibration constants. Once these parameters have been determined, the subsequent phase of the process consists of measuring the power at each detector. We must then solve a system of three simultaneous nonlinear equations (5.6) to extract the unknown reflection coefficient $\Gamma$. This calibration and measurement procedure is essential for precisely determining the reflection coefficient and, by extension, characterizing the behavior of the MUT.

The calibration constants of the six-port reflectometer can be expressed in terms of S-parameters using the equation given by Wiedmann, for more details [243]:

$$q_i = \frac{-S_{i1}}{S_{22}S_{i1} - S_{21}S_{i2}} \tag{5.7}$$

## 5.3. Proposed six-port reflectometer system

In this study, we use the metallic WR15 waveguide six-port system operating within the frequency range of 55-75 GHz. The metallic waveguide technology provides isolation between nearby signals and presents immunity to environmental variations. Figure 5.2 depicts both the schematic and an image of the used system.

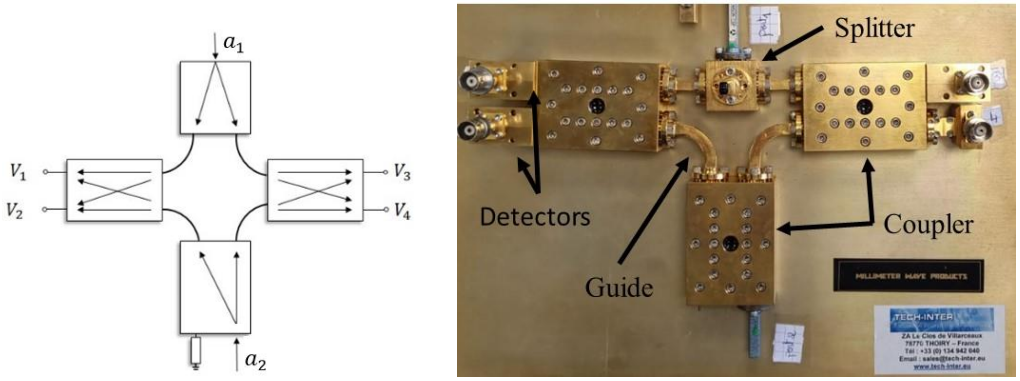


(a) (b)

Figure 5.2 (a) Structure of the six-port; (b) Photograph of the WR15 waveguide six-port.

The circuit is implemented using power divider (splitter), three $90^0$hybrid couplers and four power detectors with typical video sensitivity of 500 $mV/mW$ and tangential sensitivity of -50$dBm$. The splitter efficiently splits the incoming signal from the port 1 into multiple equal parts, allowing for simultaneous signal processing. The couplers are used to combine and divide signals with phase differences, ensuring that the signals are distributed appropriately in the circuit. The power detectors are used for accurate measurement of the power levels of signals at various points in the circuit. To connect these components, metallic straight and bended waveguides are employed.

In contrast with previous works, no reference detector is used as a stable and high performance 60 GHz RF power source is used. In addition, we model directly the detected voltage as a function of the unknown quantities, i.e. amplitude and phase-shift of the signal $a_2$. The reference microwave signal $a_1$ feeds the six-port network through the port 1. The signal $a_2$ (to be determined) is applied to the port 2. Assuming that the two millimeter-wave signals $a_1$and $a_2$with phase$\varphi_1$and phase$\varphi_2$ respectively. Let$\Delta\varphi = \varphi_2 - \varphi_1$ is the phase shift between the two signals. The following equations describe the detected voltages at the output ports:

$$V_1 = \frac{\gamma}{4}[{a_1}^2 + {a_2}^2 - 2a_1a_2cos(\Delta\varphi)] \quad (5.8)$$

$$V_2 = \frac{\gamma}{4}[{a_1}^2 + {a_2}^2 + 2a_1a_2cos(\Delta\varphi)] \quad (5.9)$$

$$V_3 = \frac{\gamma}{4}[{a_1}^2 + {a_2}^2 - 2a_1a_2sin(\Delta\varphi)] \quad (5.10)$$

$$V_4 = \frac{\gamma}{4}[{a_1}^2 + {a_2}^2 + 2a_1a_2sin(\Delta\varphi)] \quad (5.11)$$

## 5.4. Detector characterization

Prior to initiating any measurements, the initial step involves characterizing the four power detectors within the six-port reflectometer, in order to model the distortions inherent in their electrical responses. The primary objective of this process is to ensure that the system's output accurately reflects the input signal, without undesired distortions that could introduce inaccuracies into the measurements.

For this experiment, the port 1 is connected to a frequency synthesizer Keysight TM E8257D with the power varying between 10 $\mu$W and 2mW and frequency fixed at 60 GHz. The second port of the six-port reflectometer is connected to a match termination to make the electrical response depending only of the source signal (figure 5.3). A digital scope is used to measure the detected voltages: $V_1, V_2, V_3, V_4$.

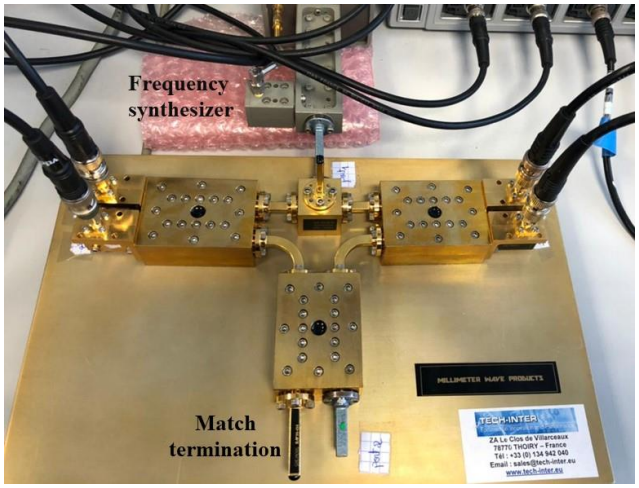


Figure 5.3 Proposed six-port reflectometer platform for detector linearization testing.

Figure 5.4 presents the input reference power as a function of the measured DC voltage for the four detectors.

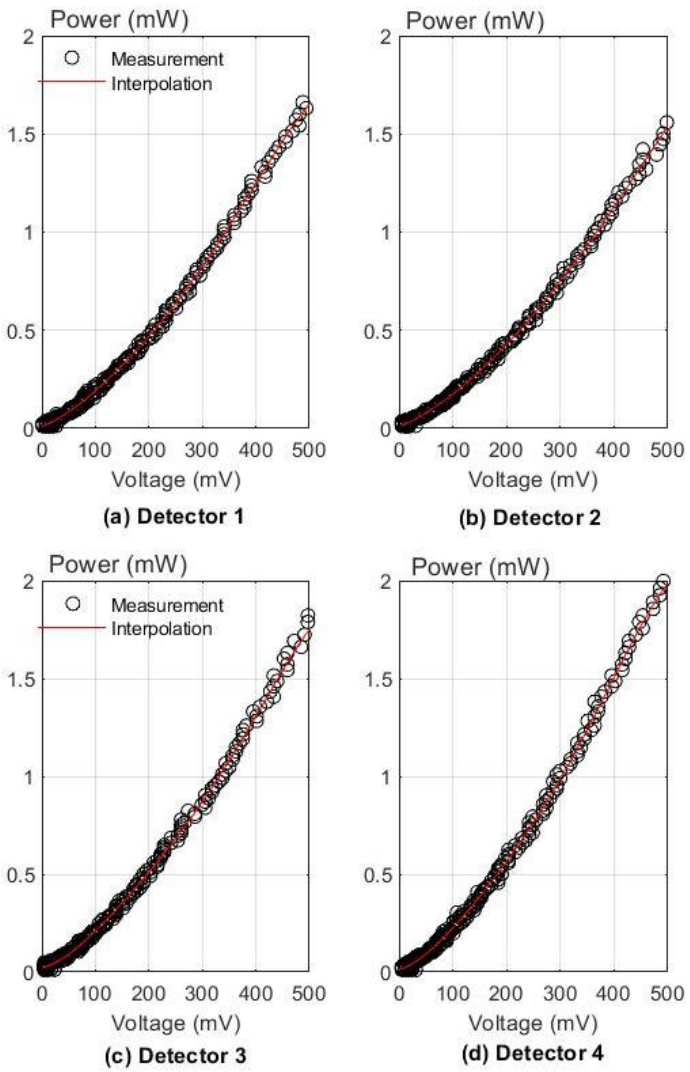


Figure 5.4 Input reference power as a function of the measured voltage and polynomial interpolation.

We can notice that the four detectors show distinct responses to incoming signals, indicating differences in their sensitivity levels. To characterize these responses, we use an interpolation technique aimed at creating a standardized representation of the detectors responses, thus reducing the effects of non-linear effects. This interpolation involves fitting the measured data with a polynomial function, and in this study, we specifically use a 5th order polynomial. The interpolation models for the powers $P_1, P_2, P_3, P_4$ are given by:

$$P_1 = -7.6631 \times 10^{-14} V_1^5 + 8.1006 \times 10^{-11} V_1^4 - 3.2462 \times 10^{-8} V_1^3 + 9.964410^{-6} V_1^2 + 1.0829 \times 10^{-3} V_1 + 0.927 \times 10^{-2} \quad (5.12)$$

$$P_2 = -2.1079 \times 10^{-14} V_1^5 + 2.4364 \times 10^{-11} V_1^4 - 1.2361 \times 10^{-8} V_1^3 + 6.6551 \times 10^{-6} V_1^2 + 1.0986 \times 10^{-3} V_1 + 0.8386 \times 10^{-2} \quad (5.13)$$

$$P_3 = -1.3183 \times 10^{-13} V_1^5 + 1.6147 \times 10^{-10} V_1^4 - 7.2808 \times 10^{-8} V_1^3 + 1.8125 \times 10^{-5} V_1^2 + 6.5545 \times 10^{-4} V_1 + 0.2072 \times 10^{-1} \quad (5.14)$$

$$P_3 = -1.5935 \times 10^{-13} V_1^5 + 1.8046 \times 10^{-10} V_1^4 - 7.5459 \times 10^{-8} V_1^3 + 1.872 \times 10^{-5} V_1^2 + 8.5338 \times 10^{-4} V_1 + 0.1058 \times 10^{-1} \quad (5.15)$$

Therefore, we have derived four equations based on the detected voltages that characterize the power detectors of the six-port system.

## 5.5. IQ demodulator

The flexibility of the six-port reflectometer goes well beyond its traditional uses, serving as a valuable IQ demodulator for millimeter-wave signals and allowing for highly accurate phase-shift measurements. The proposed system is presented in figure 5.5.

The port 1 is connected to the frequency synthesizer. The port 2 is adjusted with an attenuator (MI-WAVE 510 V/385) and phase- shifter (MI-WAVE 528 V/385). A digital scope is used to measure the detected voltages. The attenuator allows for precise adjustment of signal power, enabling controlled variations in signal intensity for experiments and calibration. Simultaneously, the phase-shifter grants precise control over the phase of the signal, making it possible to measure and manipulate phase differences, which is essential for experiments involving phase-shift.

The source power is set to 0 dBm and the test frequency is set to 60 GHz. The attenuation is varied from 0to $-24dBm$ with steps of 3 dBm. we measure the voltages at the four detectors function of the phase-shift ($\Delta\phi$) varied from 0 to 360° with steps of 10°.

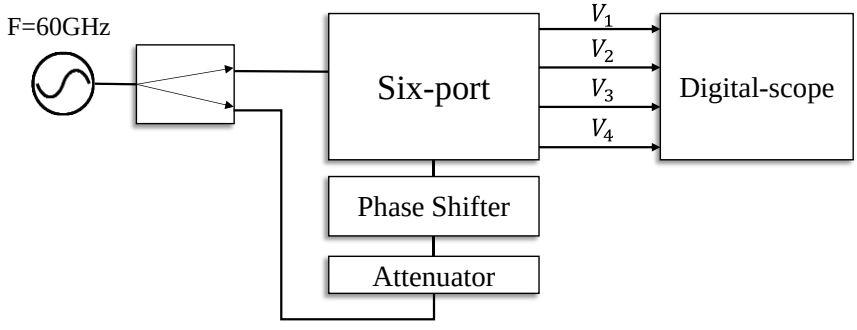


(a)

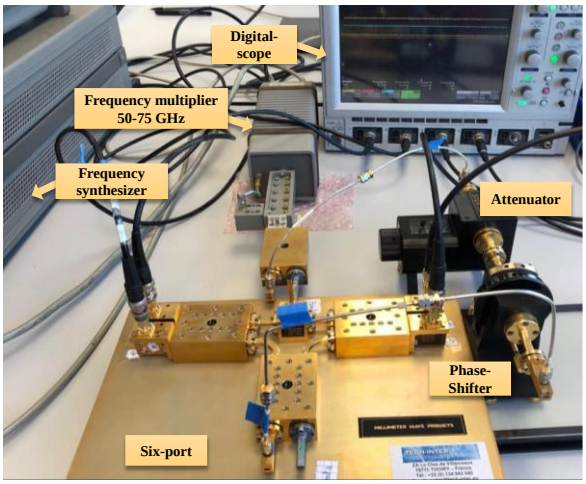


(b)

Figure 5.5 The IQ demodulator platform: (a) schematic; (b) photograph.

Figure 5.6 presents the detected voltages $V_1$ and $V_3$ as a function of the phase-shift$\Delta\phi$ at different attenuation. The detected signatures of $V_1$ and $V_3$ have nearly sinusoidal behaviors with a relative phase-shift of 90°. And the same results will be observed for $V_2$ and $V_4$. We notice that the greater the attenuation level, the lower the amplitude of the detected voltages.

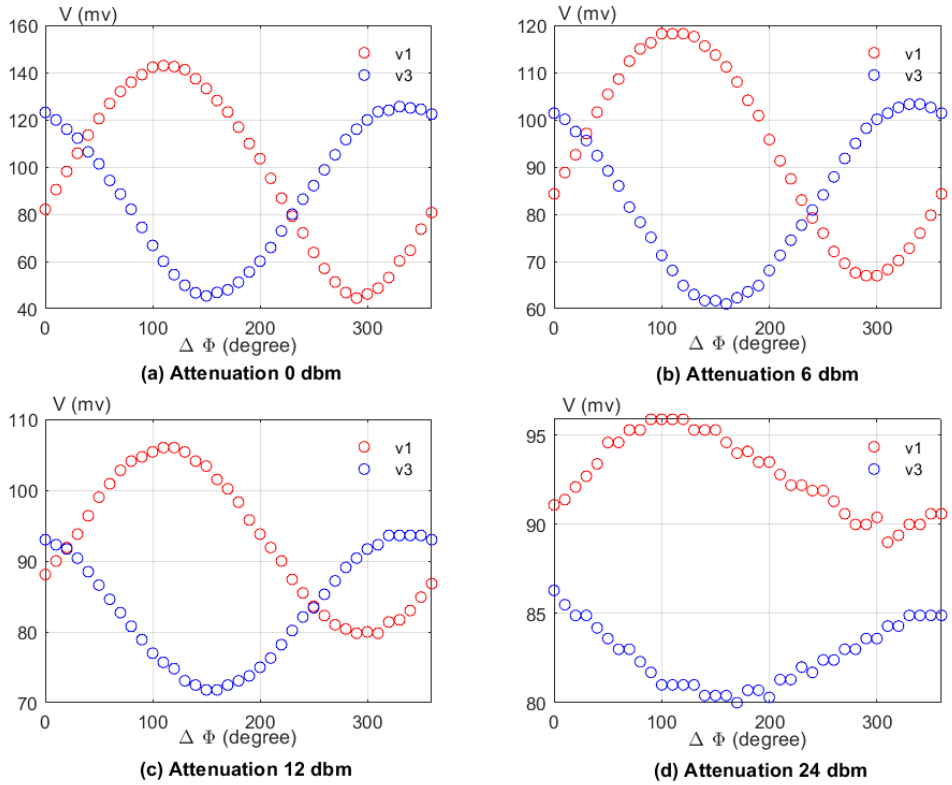


Figure 5.6 The detected voltages $V_1$ and $V_3$(mV) as function of the phase-shift $\Delta\phi$ (degree) at different attenuations.

To take into account all the imperfections and gain the ability to demodulate millimeter-wave signals, we determine the phase-shift from the detected voltages by applying a dedicated calibration modelling. We consider a linear calibration model introducing calibration coefficients taking into account millimeter-wave losses and detectors sensitivities [226]. The calibration process includes the following steps:

(1) Calculate the real IQ components at fixed attenuation function of $\Delta\phi$ varied from 0 to 360° with steps of 10°, using the equations:

$$I = Att.cos(\Delta\phi) \tag{5.16}$$

$$Q = Att.sin(\Delta\phi) \tag{5.17}$$

where $Att$ and $\Delta\phi$ are the attenuation and the phase-shift between the two input signals.

(2) Determine the calibration coefficients ($\alpha_i$, $\alpha_i{}'$) by fitting the measured voltages $V_1$ and $V_3$to the linear calibration model:

$$V_1 = \alpha_0 + \alpha_1 I + \alpha_2 Q \tag{5.18}$$

$$V_3 = \alpha'_0 + \alpha'_1 I + \alpha'_2 Q \tag{5.19}$$

In this study, we use iterative functions using MATLAB, which are based on minimizing the sum of the squared differences between the measured data and the values predicted by our calibration model. By iteratively refining the calibration coefficients, these functions enable to find the optimal parameter values that provide precise and accurate calibration for our measurements. Once we calculate the calibration coefficient, we determine the detected voltages $V_1$ and $V_3$. Figure 5.7 presents the detected voltages $V_1$ and $V_3$(mV) and their fitting curves.

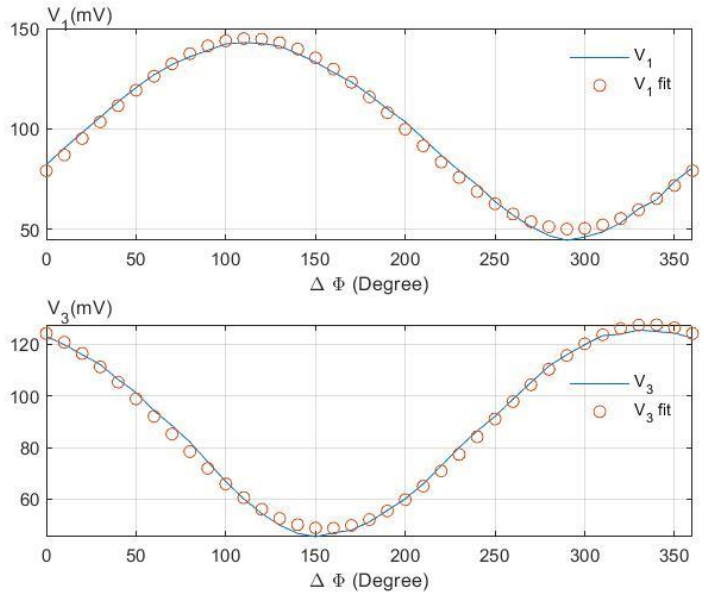


Figure 5.7 the detected voltages $V_1$ and $V_3$(mV) and their fitted curves after calibration as function of the phase-shift $\Delta\phi$ (degree).

(3) Calculate the measured IQ components by the inversion of the calibration model, equations (5.18 - 5.19).
(4) Conclude the measured phase-shift $\Delta\Phi$:

$$\Delta\phi = atan\left(\frac{Q}{I}\right) \tag{5.20}$$

Following these steps, we compare the phase-shift measurements before and after detector linearization. We used the equations (5.12 to 5.15) to deduce the powers from the measured voltages, then we apply the calibration method using these powers. Figure 5.8 presents the powers $P_1$and $P_3$ and there fitted curve after calibration. We find that the average error decreases significantly from 6.01 degrees to 2.2 degrees after the detector linearization step.

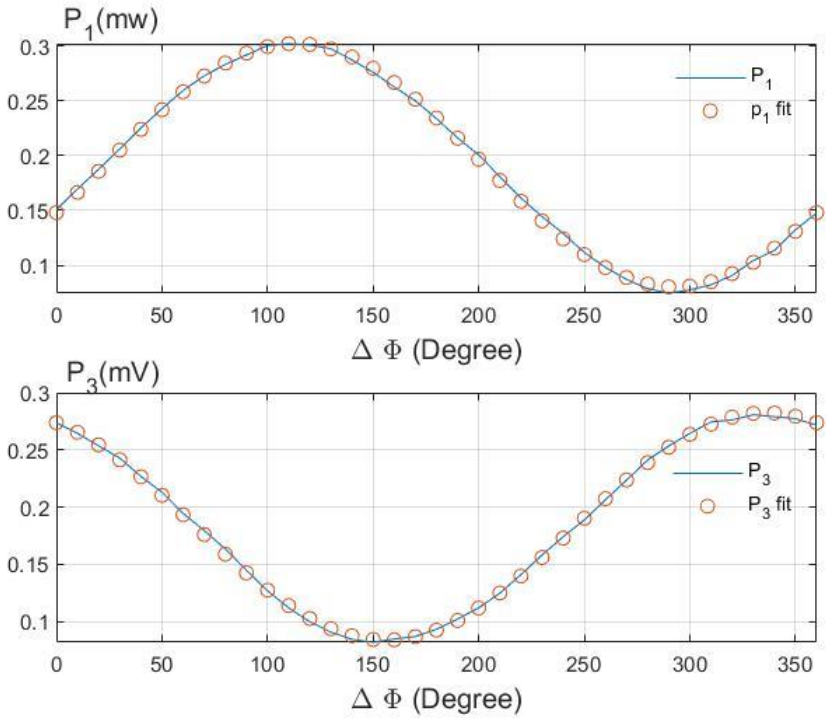


Figure 5.8 The powers $P_1$and $P_3$ and their fitted curves after calibration the powers $P_1$and $P_3$ and there fitted curve after calibration.

The calibration system described in this work is linear, and we made certain assumptions. However, it is important to acknowledge that an alternative nonlinear calibration system could be employed, resulting in enhanced accuracy. More detailes in [101].

## 5.6. Free-space measurement

In this section, we present a six-port based measurement system designed for free-space applications, enabling extremely accurate sub-millimeter distance measurements. A schematic diagram and photo of the system are shown in the figure 5.9. The system includes the key components: a frequency synthesizer, low noise amplifier, circulator and horn antenna working as transmitter and receiver and a piezo-based nano-positioning stage that holds a metallic target

(dimensions = 3 .2 × 4.2 $cm^2$). The radar operates at the single frequency 60 GHz in relative proximity to the target.

The port 1 of the six-port is directly connected to the frequency synthesizer, acting as its reference source. The port 2 is connected to the antenna via an amplifier and the circulator. The input signal is directed to the horn antenna, which emits the signal toward the target. Subsequently, the metallic plate reflects the signal back to the antenna, effectively receiving the signal and transmitting it back to the second port of the six-port radar. The circulator efficiently guides the received signal to the second input port of the six-port in a unidirectional manner, ensuring strong isolation and minimizing interference. The low noise amplifier is used to enhance the signal-to-noise ratio at the signal reception.

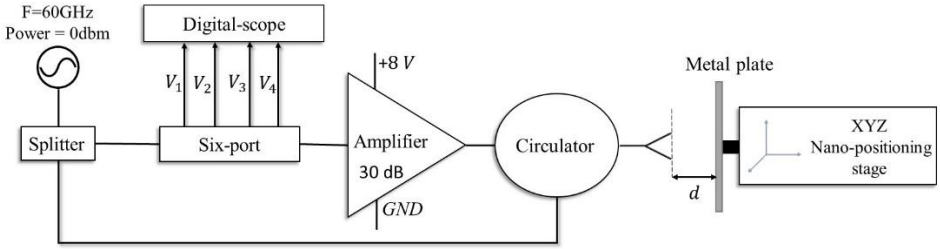


(a)

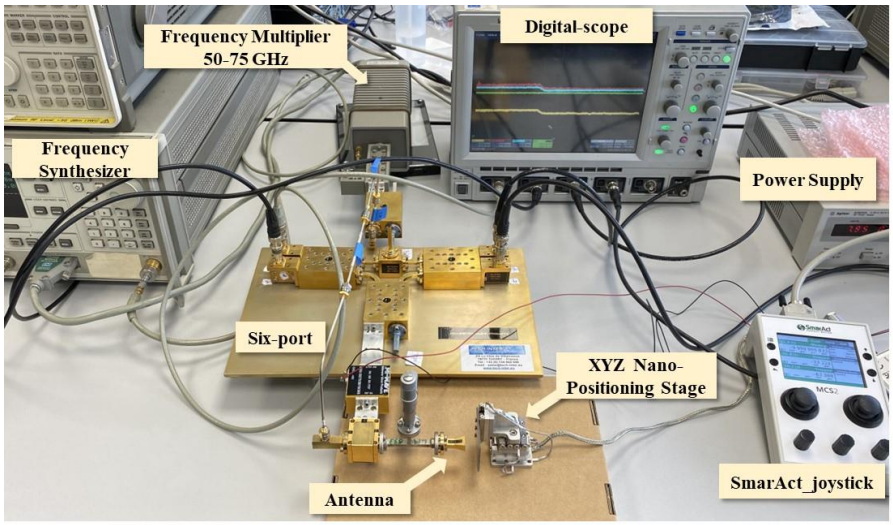


(b)

Figure 5.9 Proposed test platform for mm-wave free-space distance measurement: (a) schematic; (b) photograph.

The test platform proposed has been fully automated under Labview® environment to set the measurement parameters (reference power, frequency, distance range and step) and to provide detected voltages under different measurement configurations.

First, we perform a repeatability study to evaluate the accuracy of the measurements. We repeatedly measure the four voltages, $V_1$, $V_2$, $V_3$, and $V_4$, while adjusting the distance between the metallic target and the antenna, ranging from 5 to 6 mm with step of 500nm (figure 5.10). This process is repeated over ten consecutive trials and then the standard deviation between these

measurements is calculated. The percentage of maximum standard deviation on $V_1$, $V_2$, $V_3$, and $V_4$are 2.0120% and 0.8794%, 1.3089%, 1.1637% respectively.

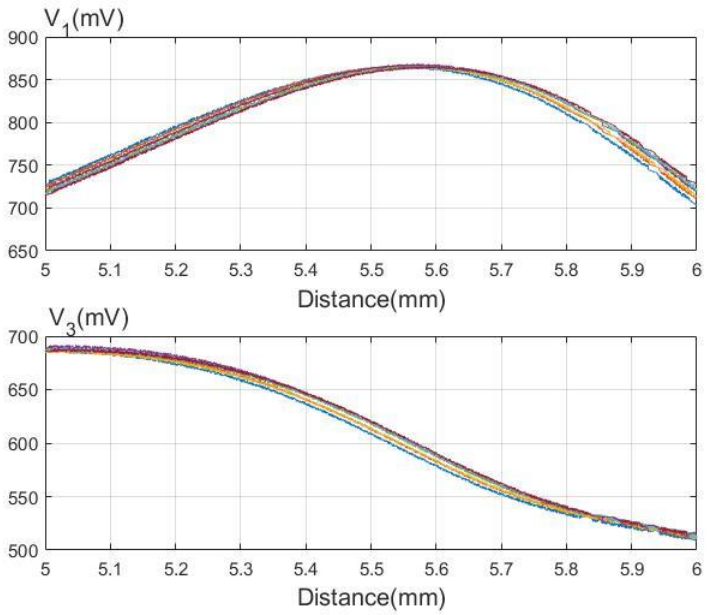


Figure 5.10 Ten consecutive measurements of $V_1$(mV) and $V_3$ (mV) function of distance (mm).

Then, as a demonstration, experiments are considered for near field distance measurement from contact to stand-off set to 5 mm (2 free-space wavelengths). The target is moved along one linear stage in steps of 500 nm over the full range. The four detected voltages as a function of the distance are given in figure 5.11.

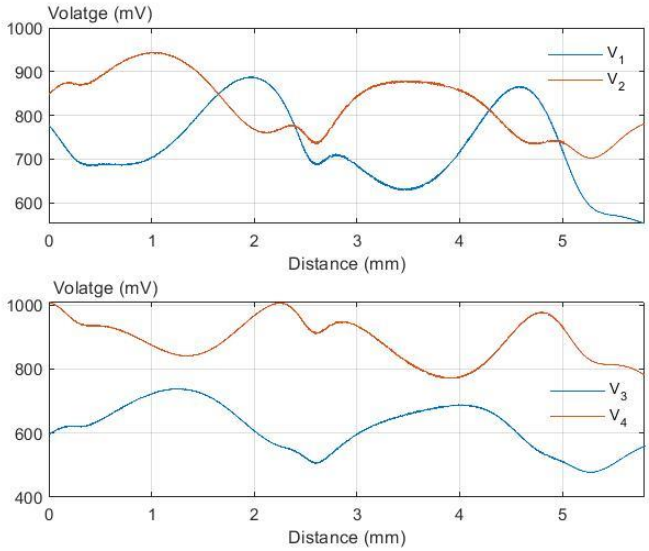


Figure 5.11 Ten consecutive measurements of voltages function of distance (mm).

Qualitatively, a good measurement sensitivity to the distance is noticed. The measured voltages are sensitive to the distance variations in sub-millimeter range. However, the shapes of

the curves are not sinusoidal as the target is located in the near-field of the antenna. In addition, free-space multiple reflections between the antenna aperture and the target yield to signal distortion. The detected voltage as a function of the distance shows the spread propagation losses that increase with distance. Furthermore, resonances are related to wave recombination between the reflected wave by that target, the guided reflected wave at the antenna input (mismatch) and the free-space source match term (reflection of the received wave by the antenna).

Figure 5.12 presents $V_3 - V_4$ as a function of $V_1 - V_2$ that should exhibit graphically a circle centered on 0 for an ideal configuration. An elliptical behavior related to the system imperfections is noticed.

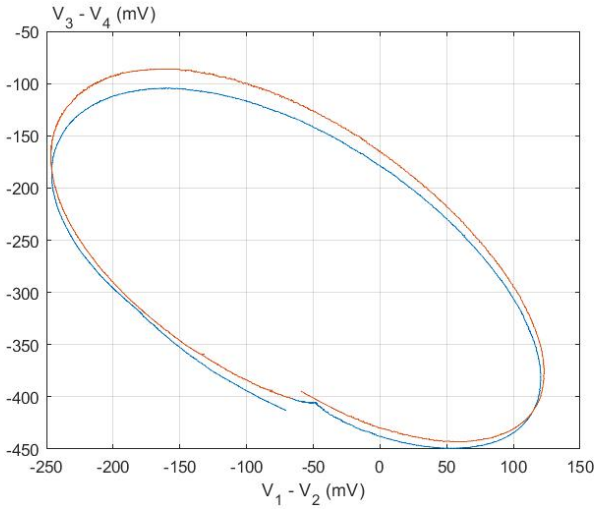


Figure 5.12 $V_3 - V_4$ as a function of $V_1 - V_2$.

We derive equations (5.21) and (5.22) from the expressions provided in equations (5.8 to 5.11). In ideal conditions, the equations show that $V_1$ and $V_2$ should exhibit the same amplitude and a 90 degree phase difference, as should $V_3$ and $V_4$. This results in a circular pattern when plotted in a graph, centered at the origin. Any deviations from this ideal behavior result in elliptical patterns, which can be indicative of imperfections or variations in the six-port network or the system's components.

$$V_1 - V_2 = -\gamma a_1 a_2 cos(\Delta\varphi) \tag{5.21}$$

$$V_3 - V_4 = -\gamma a_1 a_2 sin(\Delta\varphi) \tag{5.22}$$

As a conclusion, a dedicated free-space calibration method that takes into account these effects can be implemented to derive the distance as a function of the measured voltages [228].

## 5.7. Conclusion

Six-port technology was emerged as a significant alternative to the conventional heterodyne architecture for microwave sensing in harsh environments. This technology demonstrates increased resilience to environmental impacts, providing higher levels of accuracy and resolution. Additionally, six-port technology tends to be simpler and less expensive to manufacture. Recent

advances in six-port circuit design, signal processing algorithms, and integrated devices have made six-port technology more attractive for a wide range of applications.

In this chapter, we started by presenting an overview of the general definition, architecture, and principles underlying the six-port reflectometer. Subsequently, we introduced a metallic six-port reflectometer operating at frequency around 60 GHz and we conducted an evaluation of its performance in two distinct applications: as an IQ demodulator for phase-shift measurements, and in free-space measurements, with a specific focus on sub-millimeter distance measurements. A dedicated method for characterizing power detectors has been used to improve the performance of the proposed six-port system.

The validation of this system highlights its capacity to measure the reflection coefficient of the MUT with high accuracy. This allows for applying the ML and DL models proposed in the previous chapter to the measurements conducted using the six-port system. As a result, we expect an enhancement in the performance of these algorithms, promising more precise and effective characterization and evaluation of materials. Moreover, the six-port reflectometer's capability to measure distance with high accuracy contributes additional advantages to the system. This functionality allows for precise material characterization and for accurate positioning of materials with respect to the measurement system.

# Conclusion

In summary, the thesis objectives were centered on two main parts:

(1) The first objective was to propose an approach for ensuring accurate robots localization, using multi-sensors fusion. In addition, an entropy-based diagnostic phase was designed in order to make the robots work even in the presence of sensors faults.
(2) The second objective was to introduce three innovative intelligent MNDT&E techniques for material characterization. Based on generating three different databases derived from the microwave measurements, ML and DL models was applied and discussed.

After introducing the general context in chapter 1, we introduced in chapter 2 a robust localization method for mobile robots, employing a fault-tolerant multi-sensors fusion. The Extended Kalman filter was used to estimate the position of the robot by fusing information from sensors integrated on the robot. Recognizing the possibility of sensor failures and their influence on performance, we incorporated a sensor diagnostic phase to identify and exclude malfunctioning sensors. Specifically, control charts based on CUSUM and EWMA statistics were applied to generated residual signals and an adaptive threshold was proposed using an entropy-based criterion. To validate the effectiveness of our approach, we conducted a comparative analysis with existing literature, using the key metric ARL. It's worth noting that this statistical technique has broader applicability beyond robotic systems, as it can be employed in various domains to detect changes and malfunctions in any residual signal.

In this study, the mission of the mobile robots is to inspect and analyze materials in the surrounding environment. To achieve this goal, our focus was directed towards the development of NDT&E technique based on microwave technology. This latter relies on a concept to use microwave electromagnetic waves in the frequency range of 300 MHz to 300 GHz to inspect, analyze, and assess the properties, and quality of the MUT without causing any damage to the material being examined. The potential of MNDT&E lies in its ability to inspect dielectric materials with a high level of precision and efficiency.

In chapter 3, the first part presented a theoretical background relevant to microwave characterization. Starting with definition of the electromagnetic properties of materials, highlighting the interaction between microwaves and materials. We presented further, the microwave measurement systems, and the microwave characterization techniques. In a second part, we presented two conventional MNDT&E techniques tailored for material characterization, employing two distinct antennas: corrugated antenna in a first setup, compact horn antenna in a second setup. These antennas, coupled with a VNA, played a central role in measuring the amplitude and phase-shift of the complex reflection$S_{11}$ of the MUT. Furthermore, we provided a detailed description of a free-space calibration procedure specifically used to establish the relationship between the materials' permittivity and the measured $S_{11}$. To validate the efficiency of these methodologies, we conducted practical experiments using two wooden MUT samples, and subsequently, we compared our findings with previously documented results in the literature.

However, analytical modeling for the calculation of complex permittivity often encounters limitations due to various factors, such as the material thickness, frequency dependency, distance between the material and the antenna and the simplifying assumptions, etc. In this regard, ML and DL models were proposed in chapter 4 to offer a promising solution to overcome these limitations.

In chapter 4, we presented the theoretical fundamentals of the ML and DL models applied in this thesis. Following this, a comprehensive literature review was presented, focusing on various microwave techniques, their integration with ML and DL models for material characterization. In a second part, we proposed the design and the implementation of three intelligent MNDT&E techniques which included two distinct phases, measuring the $S_{11}$ of the MUT using the microwave instruments and applying ML and DL models on the generated databases.

The first technique relies on a free-space setup, operating at frequencies ranging between 3.95 and 5.85 GHz, and was tested and validated in both laboratory and realistic conditions. Five ML models (DCT, RF, SVM with three different kernels: linear, RBF and polynomial) was used to classify materials into: wood, glass, Plexiglas, and either if no materials. We achieved a 99% accuracy in controlled laboratory settings and maintained a 95% accuracy even in more challenging and realistic conditions. The second technique relied on using an OERW operating at frequencies ranging between 3.95 and 5.85 GHz for contact material characterization and was tested and validated in laboratory conditions and realistic conditions. Applying the same five ML models, this technique provided higher accuracy, achieving 100% under controlled laboratory conditions and maintaining 99.6% accuracy level in more challenging and realistic scenarios. The third technique was specifically designed for detecting defects within materials. It relied on using OERW with frequencies ranging from 3.95 to 5.85 GHz. Applying the 1D-CNN model, the accuracy reached 82% when the model was trained using both the magnitude and phase-shift of the measured $S_{11}$, and it increased to 98% when incorporating the complex components (real and imaginary parts) of the measured $S_{11}$.

In chapter 5, we discussed a feasibility study to enhance the effectiveness and simplify the shift of microwave instruments from laboratory conditions to real-world scenarios. The key topic discussed was using a six-port reflectometer operating within the millimeter frequency range (i.e. around 60 GHz). This approach is highlighted for its potential to offer enhanced accuracy in the characterization of materials as well as in the detection of defects.

# Perspectives

To advance this study and unlock further potential, several perspectives can be mentioned.

1. In chapter 2, the proposed robust localization approach aimed at eliminating the faulty sensor(s). Future work should focus on three aspects:
   - **Evaluation under varying faults scenarios:** in-depth investigation into the diverse types of failures that may impact sensors, ranging from weather-related influences to calibration failures and temporal misalignments. This part entails the simulation of these failures, followed by a comprehensive testing and evaluation of the proposed approach under varying faults scenarios. This exploration could significantly contribute to enhancing the resilience and reliability of sensor systems in real-world applications.

   - **Fault identification**: building upon the benchmarking of failures, an additional phase could be introduced to identify, in real-time, the specific types of failures impacting sensors. A promising solution involves integrating machine learning classifiers into the diagnostic process. This approach aims to enable effective repairs when feasible and, in certain situations, support continued sensor usage. For example, in cases of calibration faults, automatic extrinsic calibration process could be considered. The objective is to establish a framework that detects faulty sensors and classifies the faults based on their types. To validate the effectiveness, a comparative study should be conducted, comparing the proposed statistical approach with the machine learning models. This research direction holds the potential to advance the field of fault identification in sensor systems.
   - **Residual generation:** our approach defines the residual signal as the disparity between the sensor measurement and the value predicted by the fusion model. A prospective avenue for future research involves exploring optimization techniques for this residual signal, with a focus on criteria such as robustness and sensitivity. One potential criterion worth investigating is the α-divergences criterion, seeking to enhance the performance of the residual signal in a manner that aligns with these specified criteria. This inquiry aims to contribute to the refinement of residual generation methods in the context of sensor fault detection.
   - **The prior probability $P_0$ :** Regarding the prior probability $P_0$ (the prior probability of $H_0$ representing the fault-free case) in the entropy-based criterion, our current assumption is that $P_0$ is calculated iteratively. A promising direction for future research involves a detailed study of this parameter and the development of quantitative methods tailored to each case study. This investigation seeks to provide a more nuanced and case-specific approach to determining the prior probability, enhancing the adaptability and accuracy of the entropy-based criterion in real-world applications.

2. In chapter 4, ML and DL were employed for material classification and defects detection. To enhance the accuracy of these models enabling them to address real-world applications, future research should focus on two critical aspects.

   - **Additional measurements and scenarios:** it is imperative to enrich the databases used in training the ML and DL models through real measurements. This process requires real measurements covers diversity of materials. In addition, scan and measure additional

scenarios consisting of various types of defects, to enhance the system's capacity for detecting subsurface defects within materials.

- **Microwave simulation:** extending databases requires employing simulations to bridge the gap between controlled laboratory conditions and the complexities of real-world scenarios that may not be easily reproducible. The two commonly used simulators for microwave simulation, are computer simulation technology microwave studio (CST) and Ansys high-frequency structure simulator (HFSS).

3. In addition to enhancement in both domains, the aim of the global project is to integrate the MNDT&E techniques on the mobile robots, and control it to inspect the surroundings autonomously. This integration requires implementing the proposed microwave measurement systems onto a mobile robot, subsequently subjecting it to comprehensive evaluation and testing in both laboratory and real-world conditions. Such integration and testing offers numerous advantages:
   - Enhance robot localization, using microwave technology for precise distance measurements, providing high-quality data for the proposed fusion approach. The use of microwave-based distance measurements contributes to improved localization accuracy, particularly in scenarios where other sensor modalities may face challenges, such as in low-visibility conditions or environments noise.
   - Enhance the performance of the MNDT&E techniques for material characterization. Automating these techniques ensures higher accuracy and enables real-time inspection of the MUT. This automation eliminates the potential for human intervention errors, enhancing the accuracy of the entire system.
   - Increase efficiency, adaptability, and accuracy of the system. Autonomous inspections by mobile robots equipped with MNDT&E capabilities hold promise for enhanced accessibility, faster response times, and the ability to navigate diverse and dynamic environments, making the technology more versatile and applicable across a wide range of applications such as in industrial applications and in challenging and harsh environments where human intervention may be impractical or dangerous.

# Bibliography


[1] M. A. Abou-Khousa *et al.*, “Detection of Surface Cracks in Metals Using Microwave and Millimeter-Wave Nondestructive Testing Techniques - A Review”, *IEEE Trans. Instrum. Meas.*, vol. 72, pp. 1–18, 2023.

[2] S. Sambath, P. Nagaraj, and N. Selvakumar, “Automatic Defect Classification in Ultrasonic NDT Using Artificial Intelligence”, *J Nondestruct Eval*, vol. 30, no. 1, pp. 20–28, 2011.

[3] A. Yassin *et al.*, “Recent Advances in Indoor Localization: A Survey on Theoretical Approaches and Applications”, *IEEE Commun. Surv. Tutorials*, vol. 19, no. 2, pp. 1327–1346, 2017.

[4] W. Wei *et al.*, “A Survey of UAV Visual Navigation Based on Monocular Slam”. In: *IEEE 4th Information Technology and Mechatronics Engineering Conference (ITOEC)*, IEEE, pp. 1849-1853, 2018.

[5] S. Ferdous, K. Vyas, and F. Makedon, “A Survey on Multi Person Identification and Localization”. In: *Proceedings of the 5th International Conference on PErvasive Technologies Related to Assistive Environments*, Heraklion Crete Greece: ACM, pp. 1–3, 2012.

[6] B. Johann, H. R. Everett, and F. Liqiang, “Navigating Mobile Robots: Systems and techniques”, *A K Peters*, 1996.

[7] D. Di Paola *et al.*, “An Autonomous Mobile Robotic System for Surveillance of Indoor Environments”, *International Journal of Advanced Robotic Systems*, vol. 7, no. 1, pp. 8, 2010.

[8] T. Meng *et al.*, “A Survey on Machine Learning for Data Fusion”, *Information Fusion*, vol. 57, pp. 115–129, 2020.

[9] G. Stienne *et al.*, “A Multi-Temporal Multi-Sensor Circular Fusion Filter”, *Information Fusion*, vol. 18, pp. 86–100, 2014.

[10] A. A. R. Broer, R. Benedictus, and D. Zarouchas, “The Need for Multi-Sensor Data Fusion in Structural Health Monitoring of Composite Aircraft Structures”, *Aerospace*, vol. 9, no. 4, pp. 183, 2022.

[11] F. Alam *et al.*, “Data Fusion and IoT for Smart Ubiquitous Environments: A Survey”, *IEEE Access*, vol. 5, pp. 9533–9554, 2017.

[12] W. Li *et al*, “A Survey on Multisensor Fusion and Consensus Filtering for Sensor Networks”, *Discrete Dynamics in Nature and Society*, vol. 2015, pp. 1–12, 2015.

[13] G. Welch, “An Introduction to the Kalman Filter”, 1997.

[14] A. Gasparri and F. Pascucci, “An Interlaced Extended Information Filter for Self-Localization in Sensor Networks”, *IEEE Trans. on Mobile Comput.*, vol. 9, no. 10, pp. 1491–1504, 2010.

[15] A. Charroud *et al.*, “Rapid Localization and Mapping Method Based on Adaptive Particle Filters”, *Sensors*, vol. 22, no. 23, pp. 9439, 2022.

[16] D. C. Montgomery, “Statistical Quality Control”, *Wiley*, vol. 7, 2009.

[17] B. Daass, « Approches Informationnelles pour une Navigation Autonome Collaborative de Robots d'Exploration de Zones à Risques », Thèse de doctorat, Université de Lille, 2020.

[18] A. Censi, “An ICP variant using a point-to-line metric”, In: *2008 IEEE International Conference on Robotics and Automation*, Pasadena, CA, USA: IEEE, 2008, pp. 19–25.

[19] D. Laurent, « Agrégation d'Information pour la Localisation d'un Robot Mobile sur une Carte Imparfaite », Thèse de doctorat, Université Clermont Auvergne, 2018.
[20] D. Smith and S. Singh, "Approaches to Multisensor Data Fusion in Target Tracking: A Survey", *IEEE Trans. Knowl. Data Eng.*, vol. 18, no. 12, pp. 1696–1710, 2006.
[21] H. Jeong *et al.*, "Fault Detection and Identification Method Using Observer-Based Residuals", *Reliability Engineering & System Safety*, vol. 184, pp. 27–40, 2019.
[22] A. K. A. Karim, D. Virginie, and C. Vincent, "Sensitivity Analysis of Residuals for Soft Fault Monitoring in Y-shaped Networks", In: *2022 International Conference on Control, Automation and Diagnosis (ICCAD)*, Lisbon, Portugal, IEEE, pp. 1–6, 2022.
[23] D. Yang, H. R. Karimi, and L. Gelman, "A Fuzzy Fusion Rotating Machinery Fault Diagnosis Framework Based on the Enhancement Deep Convolutional Neural Networks", *Sensors*, vol. 22, no. 2, pp. 671, 2022.
[24] E. Khalastchi and M. Kalech, "On Fault Detection and Diagnosis in Robotic Systems", *ACM Comput. Surv.*, vol. 51, no. 1, pp. 1–24, 2019.
[25] J. S. Oakland, "Statistical Process Control", 5. ed. Oxford: Butterworth-Heinemann, 2003.
[26] D. Pomorski and C. Desrousseaux, « Optimisation Entropique des Systèmes de Détection Distribuée Parallèle », *Traitement du Signal*, vol. 17, no. 4, pp. 341–351, 2000.
[27] Z. J. Viharos and R. Jakab, "Reinforcement Learning for Statistical Process Control in Manufacturing", *Measurement*, vol. 182, pp. 109616, 2021.
[28] M. Ebadi and A. Ahmadi-Javid, "Socio-Economic Design of Control Charts for Monitoring Service Processes: A Case Study of a Restaurant System", *Quality Technology & Quantitative Management*, vol. 16, no. 6, pp. 726–735, 2019.
[29] K. Bisiotis, S. Psarakis, and A. N. Yannacopoulos, "Control Charts in Financial Applications: An Overview", *Quality & Reliability Eng*, vol. 38, no. 3, pp. 1441–1462, 2022.
[30] H. Sounni, N. Elkamoun, and F. Lakrami, "SPC-Based Approach for DDoS Attack Detection Using X-MR Control Chart", *International Journal on Information Technologies & Security* vol. 13, no. 2, 2021.
[31] J. Hu *et al.*, "Adaptive Resources Allocation CUSUM for Binomial Count Data Monitoring with Application to COVID-19 Hotspot Detection", *Journal of Applied Statistics*, vol. 50, no. 14, pp. 2889–2913, 2023.
[32] A. De Vries and J. K. Reneau, "Application of Statistical Process Control Charts to Monitor Changes in Animal Production Systems", *Journal of Animal Science*, vol. 88, no. suppl_13, pp. E11–E24. 2010.
[33] G. Suman and D. Prajapati, "Control Chart Applications in Healthcare: A Literature Review", *Int. J. Metrol. Qual. Eng.*, vol. 9, pp. 5, 2018.
[34] Shewhart, W. A, "Economic Control of Quality of Manufactured Product", 1929.
[35] E. S. PAGE, "Continuous Inspection Schemes". *Biometrika*, vol. 41, no. 1/2, pp. 100-115, 1954.
[36] S. W. Roberts, "Control Chart Tests Based on Geometric Moving Averages", *Technometrics*, vol. 42, no. 1, p. 97-101, 2000.
[37] S. S. Prabhu, G. C. Runger, and J. B Keats, "An Adaptive Sample Size *X* Chart", *Int J Prod Res*, vol. 31, no. 12, pp. 2895-2909,1993.
[38] M. R. Reynolds *et al.*, "Charts with Variable Sampling Intervals", *Technometrics*, vol. 30, no. 2, pp.181-192, 1988.
[39] A. F. Costa, "X Charts with Variable Sample Size", *Journal of quality technology*, vol. 26, no. 3, pp. 155–163, 1994.

[40] L. S. Zimmer, D. C. Montgomery, and G. C. Runger, “Guidelines for the Application of Adaptive Control Charting Schemes”, *International Journal of Production Research*, vol. 38, no. 9, pp. 1977–1992, 2000.
[41] G. Tagaras, “A Survey of Recent Developments in the Design of Adaptive Control Charts”, *Journal of quality technology*, vol. 30, no. 3, pp. 212–231, 1998.
[42] S. Psarakis, “Adaptive Control Charts: Recent Developments and Extensions”, *Quality & Reliability Eng*, vol. 31, no. 7, pp. 1265–1280, 2015.
[43] Z. Wu *et al.*, “An Enhanced Adaptive CUSUM Control Chart”, *IIE transactions*, vol. 41, pp. 642–653, 2009.
[44] A. Saba and A. Haq, “New Adaptive CUSUM Charts for Process Mean”, *Communications in Statistics - Simulation and Computation*, vol. 49, no. 11, pp. 2944-2962, 2020.
[45] R. B Crosier, “A New Two-Sided Cumulative Sum Quality Control Scheme”, *Technometrics*, vol. 28, no. 3, pp. 187-194, 1986.
[46] J. Li, “Adaptive CUSUM Chart with Cautious Parameter Learning”, *Quality & Reliability Eng*, vol. 38, no. 6, pp. 3135–3156, 2022.
[47] M. Noor-ul-Amin, A. Arshad, and M. Hanif, “A Function Based Adaptive EWMA Mean Monitoring Control Chart”, *Quality & Reliability Eng*, vol. 38, no. 1, pp. 248–263, 2022.
[48] A. Haq, R. Gulzar, and B. C. Michael, “An Efficient Adaptive EWMA Control Chart for Monitoring the Process Mean”, *Qual Reliab Engng Int*, vol. 34, pp. 563–571, 2018.
[49] M. A. Sarwar and M. Noor-ul-Amin, “Design of a New Adaptive EWMA Control Chart”, *Quality & Reliability Eng*, vol. 38, no. 7, pp. 3422–3436, 2022.
[50] J. Kim *et al.*, “Adaptive Cumulative Sum Charts with the Adaptive Runs Rule”, *International Journal of Production Research*, vol. 51, no. 15, pp. 4556–4569, 2013.
[51] N. Abbas, M. Riaz, and R. J. M. M. Does, “Mixed Exponentially Weighted Moving Average–Cumulative Sum Charts for Process Monitoring”, *Quality & Reliability Eng*, vol. 29, no. 3, pp. 345–356, 2013
[52] A. Kouadri *et al.*, “An Adaptive Threshold Estimation Scheme for Abrupt Changes Detection Algorithm in a Cement Rotary Kiln”, *Journal of Computational and Applied Mathematics*, vol. 259, pp. 835–842, 2014.
[53] S. Dey *et al.*, “Model-Based Real-Time Thermal Fault Diagnosis of Lithium-Ion Batteries”, *Control Engineering Practice*, vol. 56, pp. 37–48, 2016.
[54] A. Bakdi, A. Kouadri, and A. Bensmail, “Fault Detection and Diagnosis in a Cement Rotary Kiln Using PCA with EWMA-based Adaptive Threshold Monitoring Scheme”, *Control Engineering Practice*, vol. 66, pp. 64–75, 2017.
[55] A. Haq and M. Awais, “New Shewhart-EWMA and Shewhart-CUSUM Control Charts for Monitoring Process Mean”, *Scientia Iranica*, vol. 26, no. 6, pp. 3796-3818, 2019.
[56] A. Haq, S. Akhtar, and M. Boon Chong Khoo, “Adaptive CUSUM and EWMA Charts with Auxiliary Information and Variable Sampling Intervals for Monitoring the Process Mean”, *Quality & Reliability Eng*, vol. 37, no. 1, pp. 47–59, 2021.
[57] A. Haq and F. Razzaq, “New Weighted Adaptive CUSUM Dispersion Charts”, *Quality & Reliability Eng*, vol. 38, no. 1, pp. 110–133, 2022.
[58] J. Zhang, Z. Li, and Z. Wang, “A New Adaptive Control Chart for Monitoring Process Mean and Variability”, *Int J Adv Manuf Technol*, vol. 60, no. 9–12, pp. 1031–1038, 2012.
[59] S. Haridy *et al.*, “An Improved Design of Exponentially Weighted Moving Average Scheme for Monitoring Attributes”, *International Journal of Production Research*, vol. 58, no. 3, pp. 931–946, 2020.

[60] M. Aslam *et al.*, "A Mixed Control Chart to Monitor the Process", *International Journal of Production Research*, vol. 53, no. 15, pp. 4684–4693, 2015.
[61] C. Shannon and W. Weaver, "The Mathematical Theory of Communication", *The Bell system technical journal*, vol. 27, no. 3, p. 379-423, 1948.
[62] S. Verdu, "Fifty Years of Shannon Theory", *IEEE Trans. Info. Theory*, vol. 44, no. 6, 1998.
[63] I. Y. Hoballah and P. K. Varshney, "An Information Theoretic Approach to the Distributed Detection Problem", *IEEE Trans. Inform. Theory*, vol. 35, no. 5, pp. 988–994,1989.
[64] B. Daass, D. Pomorski, and K. Haddadi, "Using an Adaptive Entropy-based Threshold for Change Detection Methods – Application to Fault-tolerant Fusion in Collaborative Mobile Robotics", In: *2019 6th International Conference on Control, Decision and Information Technologies (CoDIT)*, Paris, France: IEEE, pp. 1173–1178, 2019.
[65] D. Pomorski and C. Desrousseaux, "Improving Performance of Distributed Detection Networks: An Entropy-based Optimization", *Signal Processing*, vol. 81, no. 12, p. 2479-2491, 2001.
[66] D. A. E. D. Brook, and D. Evans, "An Approach to the Probability Distribution of CUSUM Run Length", *Biometrika*, vol. 59, no. 3, pp. 539-549, 1972.
[67] S. V. Crowder, "A Simple Method for Studying Run-Length Distributions of Exponentially Weighted Moving Average Charts", *Technometrics*, vol. 29, pp. 401-407, 1987.
[68] RS. Sparks, "CUSUM Charts for Signalling varying location shifts", *Journal of Quality Technology*, vol. 32, no. 2, pp. 157-171, 2000.
[69] J. M. Lucas and M. S. Saccucci, "Exponentially Weighted Moving Average Control Schemes: Properties and Enhancements", vol. 32, no. 1, pp. 1-12, 1990.
[70] J. Dumont-Fillon. « Contrôle non destructif (CND) », *Ed. Techniques Ingénieur*, 1996.
[71] S. K. Dwivedi, M. Vishwakarma, and A. Soni, "Advances and Researches on Non Destructive Testing: A Review", *Materials Today: Proceedings*, vol. 5, no. 2, pp. 3690-3698, 2018.
[72] K. Haddadi and T. Lasri, "CW Radar for Monitoring Water-to-cellular Concrete", In: *2014 44th European Microwave Conference*, Rome: IEEE, pp. 1832–1835, 2014.
[73] S. Kumar, and D. G. Mahto, "Recent Trends in Industrial and Other Engineering Applications of Non Destructive Testing: A Review", *International Journal of Scientific & Engineering Research*, vol. 4, no. 9, 2013.
[74] K. Haddadi *et al.*, "Contactless Microwave Technique Based on a Spread-Loss Model for Dielectric Materials Characterization", *IEEE Microw. Wireless Compon. Lett.*, vol. 19, no. 1, pp. 33-35, 2009.
[75] S. Gu, K. Haddadi, and T. Lasri, "Near-field Microwave Microscopy for Liquid Characterization", In: *2014 44th European Microwave Conference*, Rome, IEEE, pp. 628-631, 2014.
[76] R. Suganya and P. Myvizhi, "Theoretical Study on NDT". *International Journal of Pure and Applied Mathematics*, vol. 119, no. 12, pp. 4709-4716, 2018.
[77] S. Gholizadeh, "A Review of Non-Destructive Testing Methods of Composite Materials", *Procedia Structural Integrity*, vol. 1, pp. 50-57, 2016.
[78] P. J. Shull, "Nondestructive Evaluation: Theory, Techniques, and Applications", *CRC press*, 2002.

[79] Y. Y. Hung *et al.,* "Review and Comparison of Shearography and Active Thermography for Nondestructive Evaluation", *Materials Science and Engineering: R: Reports*, vol. 64, no. 5-6, pp. 73-112, 2009.
[80] K. Brumbaugh *et al.,* "Material Classification using Convolution Neural Network (CNN) for X-ray Based Coded Aperture Diffraction System", In: *Anomaly Detection and Imaging with X-rays (ADIX) IV*, SPIE, pp. 63-71, 2019.
[81] J. S. Popovics and J. L. Rose, "A Survey of Developments in Ultrasonic NDE of Concrete", *IEEE Trans. Ultrason., Ferroelect., Freq. Contr.*, vol. 41, no. 1, pp. 140–143, 1994.
[82] A. Sophian *et al.,* "Electromagnetic and Eddy Current NDT: A Review", *Insight*, vol. 43, no. 5, pp. 302-306, 2001.
[83] K. Brinker *et al.,* "Review of Advances in Microwave and Millimeter-Wave NDT&E: Principles and Applications", *Phil. Trans. R. Soc. A.*, vol. 378, no. 2182, pp. 20190585, 2020.
[84] M. C. Decreton and F. E. Gardiol, "Simple Nondestructive Method for the Measurement of Complex Permittivity", *IEEE Trans. Instrum. Meas.*, vol. 23, no. 4, pp. 434–438, 1974,
[85] Chin-Yung Yeh and Reza Zoughi, "A Novel Microwave Method for Detection of Long Surface Cracks in Metals", *IEEE Trans. Instrum. Meas.*, vol. 43, no. 5, pp. 719–725, 1994.
[86] D. A. Tonga *et al.,* "Nondestructive Evaluation of Fiber-Reinforced Polymer Using Microwave Techniques: A Review", *Coatings*, vol. 13, no. 3, pp. 590, 2023.
[87] M. A. Gacem *et al.,* "Measurement of Construction Materials Properties Using Wi-Fi and Convolutional Neural Networks", *IEEE Access*, vol. 10, pp. 126100–126116, 2022.
[88] M. Bahrouni *et al.*, "Modeling of a Compact, Implantable, Dual-Band Antenna for Biomedical Applications", *Electronics*, vol. 12, no. 6, pp. 1475, 2023.
[89] M. Lu *et al.*, "Detection and Localization of Breast Cancer Using UWB Microwave Technology and CNN-LSTM Framework", *IEEE Trans. Microwave Theory Techn.*, vol. 70, no. 11, pp. 5085–5094, 2022.
[90] D. Covarrubias-Martínez *et al.*, "Classification of Plastic Materials Using Machine-Learning Algorithms and Microwave Resonant Sensor", *Journal of Electromagnetic Waves and Applications*, vol. 36, no. 12, pp. 1760–1775, 2022.
[91] J. G. D. Oliveira *et al.*, "A New Planar Microwave Sensor for Building Materials Complex Permittivity Characterization", *Sensors*, vol. 20, no. 21, pp. 6328, 2020.
[92] P.T. Hien and I.P. Hong, "Material Thickness Classification Using Scattering Parameters, Dielectric Constants, and Machine Learning", *Applied Sciences*, vol. 11, no. 22, pp. 10682, 2021.
[93] B. Qian *et al.*, "A Direction-Sensitive Microwave Sensor for Metal Crack Detection", *Applied Sciences*, vol. 12, no. 18, pp. 9045, 2022.
[94] K. Haddadi, « Mesure Hyperfréquence des Propriétés Electromagnétiques de Matériaux : 300 MHz à 300 GHz », *Techniques de l'Ingénieur, TI Sciences et Techniques*, 2016.
[95] K. Haddadi, « Systèmes à Base de Six-Port en Gammes Micro-Ondes et Millimétrique et Techniques de Calibrage Associées : Application à l'Analyse de Réseaux, Aux Télécommunications et Contrôle Non Destructif », Thèse de doctorat, Université de Lille, 2007.
[96] S. Planar, "Best Practice Guide for Planar S-Parameter Measurements using Vector Network Analysers", 2018.

[97] K. Haddadi and T. Lasri, “Forward V-band vector network analyzer based on a modified six-port technique”, In: *2015 IEEE Topical Conference on Wireless Sensors and Sensor Networks (WiSNet)*, San Diego, CA, USA: IEEE, 2015.
[98] A. Koelpin *et al*., “The Six-Port in Modern Society”, *IEEE Microwave*, vol. 11, no. 7, pp. 35–43, 2010.
[99] G. F. Engen and C. A. Hoer, “The Application of “Thru-Short-Delay” to the Calibration of the Dual Six-Port”, In: *MTT-S International Microwave Symposium Digest*, N/A: MTT005, pp. 184–185, 1978.
[100] K. Haddadi *et al*., “Calibration and Performance of Two New Ultra-Wideband Four-Port-Based Systems”, *IEEE Trans. Microwave Theory Techn.*, vol. 56, no. 12, pp. 3137–3142, 2008.
[101] K. Haddadi and T. Lasri, “Formulation for Complete and Accurate Calibration of Six-Port Reflectometer”, *IEEE Trans. Microwave Theory Techn.*, vol. 60, no. 3, pp. 574–581, 2012.
[102] P. I. Somlo and J. D. Hunter, “A Six-Port Reflectometer and its Complete Characterization by Convenient Calibration Procedures”, *IEEE Trans. Microwave Theory Techn.*, vol. 30, no. 2, pp. 186–192, 1982.
[103] K. Haddadi *et al*., “A 60 GHz Six-Port Distance Measurement System with Sub-Millimeter Accuracy”, *IEEE Microw. Wireless Compon. Lett.*, vol. 19, no. 10, pp. 644–646, 2009.
[104] K. Haddadi *et al*., “Six-Port Reflectometer in WR15 Metallic Waveguide for Free-Space Sensing Applications”, In: *2018 IEEE Topical Conference on Wireless Sensors and Sensor Networks (WiSNet)*, Anaheim, CA: IEEE, pp. 80–83, 2018.
[105] A. Koelpin *et al.*, “Six-Port Technology for Precise Geometrical Measurement Applications - An Overview” In: *2013 European Microwave Conference*. IEEE, pp. 1587-1590, 2013.
[106] S. Benchikh *et al*., “Millimeter Wave Six-Port Radar Sensor for Precise Displacement Measurements and Gesture Sensing Applications”, In: *2019 IEEE Topical Conference on Wireless Sensors and Sensor Networks (WiSNet)*, Orlando, FL, USA: IEEE, pp. 1–3, 2019.
[107] K. Haddadi and T. Lasri, “Six-port Technology for Millimeter-Wave Radar and Imaging Applications”, In: *2014 IEEE Topical Conference on Wireless Sensors and Sensor Networks (WiSNet)*, Newport Beach, CA, USA: IEEE, pp. 1–3, 2014.
[108] A. Koelpin *et al*., “Six-Port Based Interferometry for Precise Radar and Sensing Applications”, *Sensors*, vol. 16, no. 10, pp. 1556, 2016.
[109] S. Linz *et al.*, “I/Q Imbalance Compensation for Six-Port Interferometers in Radar Applications”, In: *2014 44th European Microwave Conference*, Rome: IEEE, pp. 746–749, 2014.
[110] S. Linz *et al.*, “A Compact, Versatile Six-Port Radar Module for Industrial and Medical Applications”, *Journal of Electrical and Computer Engineering*, vol. 2013, pp. 1–10, 2013.
[111] K. Haddadi and T. Lasri, “60-GHz Near-Field Six-Port Microscope Using a Scanning Slit Probe for Subsurface Sensing”, *IEEE Sensors J.*, vol. 12, no. 8, pp. 2575–2576, 2012.
[112] K. Haddadi, D. Glay, and T. Lasri, “A 60 Ghz Scanning Near-Field Microscope with High Spatial Resolution Sub-Surface Imaging”, *IEEE Microw. Wireless Compon. Lett.*, vol. 21, no. 11, pp. 625–627, 2011.
[113] M. Voelkel *et al*., “A High Precision Reconfigureable Bistatic Interferometric Radar with Integrated Six-port Receiver at 60 GHz”, In: *2019 12th German Microwave Conference (GeMiC)*, Stuttgart, Germany: IEEE, pp. 48–50, 2019.

[114] C. Joseph and K. Shant, “Microwave NDT: An Inspection Method”. *Materials Evaluation*, vol. 75, no. 3, pp. 339-346, 2017.
[115] H. HSU, “Electromagnetic Mixing Formulas and Applications”. *IEEE Circuits and Devices Magazine*, vol. 18, no. 1, pp. 27-28, 2002.
[116] J. Baker-Jarvis, M. D. Janezic, and D. C. Degroot, “High-Frequency Dielectric Measurements”, *IEEE Instrum. Meas. Mag.*, vol. 13, no. 2, pp. 24–31, 2010.
[117] S. Kharkovsky and R. Zoughi, “Microwave and Millimeter Wave Nondestructive Testing and Evaluation - Overview and Recent Advances”, *IEEE Instrum. Meas. Mag.*, vol. 10, no. 2, pp. 26–38, 2007.
[118] T. D. Carrigan *et al.*, “Nondestructive Testing of Nonmetallic Pipelines Using Microwave Reflectometry on an In-Line Inspection Robot”, *IEEE Trans. Instrum. Meas.*, vol. 68, no. 2, pp. 586–594, 2019.
[119] S, Hassan, “Microwave Techniques and Methods for the Characterization of Dielectric Materials”, Phd Thesis, American University of Beirut, 2022.
[120] S. Linz *et al.*, “I/Q Imbalance Compensation for Six-Port Interferometers in Radar Applications”, In: *2014 44th European Microwave Conference*, Rome: IEEE, pp. 746–749, 2014.
[121] K. P. Murphy, “Machine Learning: A Probabilistic Perspective”. In: *Adaptive Computation and Machine Learning Series*. Cambridge, MA: MIT Press, 2012.
[122] K. Y. You, F. B. Esa, and Z. Abbas, “Macroscopic Characterization of Materials Using Microwave Measurement Methods — A Survey”, In: *2017 Progress in Electromagnetics Research Symposium - Fall (PIERS - FALL)*, Singapore: IEEE, pp. 194–204, 2017.
[123] M. T. Jilani, M. T. Khan, and S. M. Ali, “A Brief Review of Measuring Techniques for Characterization of Dielectric Materials” *International Journal of Information Technology and Electrical Engineering*, vol. 1, no. 1, pp. 1-5, 2012.
[124] O. V. Tereshchenko, F. J. K. Buesink, and F. B. J. Leferink, “An Overview of the Techniques for Measuring the Dielectric Properties of Materials”, In: *2011 XXXth URSI General Assembly and Scientific Symposium*, Istanbul: IEEE, pp. 1–4, 2011.
[125] Y. Gao, M. T. Ghasr, and R. Zoughi, “Spatial Mapping of Complex Permittivity from Synthetic Aperture Radar (SAR) Images”, In: *2019 IEEE International Instrumentation and Measurement Technology Conference (I2MTC)*, Auckland, New Zealand: IEEE, pp. 1–6, 2019.
[126] M. D. Janezic and J. Baker-Jarvis, “Full-Wave Analysis of a Split-Cylinder Resonator for Nondestructive Permittivity Measurements”, *IEEE Trans. Microwave Theory Techn.*, vol. 47, no. 10, pp. 2014-2020, 1999.
[127] L. Harrsion *et al.*, “Material Identification Using a Microwave Sensor Array and Machine Learning”, *Electronics*, vol. 9, no. 2, pp. 288, 2020.
[128] J. Baker-Jarvis *et al.*, “Analysis of an Open-Ended Coaxial Probe with Lift-off for Nondestructive Testing”, *IEEE Trans. Instrum. Meas.*, vol. 43, no. 5, pp. 711–718, 1994.
[129] D. K. Ghodgaonkar, V. V. Varadan, and V. K. Varadan, “A Free-Space Method for Measurement of Dielectric Constants and Loss Tangents at Microwave Frequencies”, *IEEE Trans. Instrum. Meas.*, vol. 38, no. 3, pp. 789–793, 1989.
[130] A. M. Nicolson and G. F. Ross, “Measurement of the Intrinsic Properties of Materials by Time-Domain Techniques”, *IEEE Trans. Instrum. Meas.*, vol. 19, no. 4, pp. 377–382, 1970.
[131] K. Y. You, “Materials Characterization Using Microwave Waveguide System”, In: *Microwave Systems and Applications*, S. K. Goudos, Ed., InTech, 2017.

[132] S. Trabelsi and S. O. Nelson, “Free-Space Measurement of Dielectric Properties of Cereal Grain and Oilseed at Microwave Frequencies”, *Meas. Sci. Technol.*, vol. 14, no. 5, pp. 589–600, 2003.
[133] R. Sivakumar *et al.*, “A Free Space Material Measurement System”, Engineering preprint, 2023.
[134] K. Haddadi and T. Lasri, “Geometrical Optics-Based Model for Dielectric Constant and Loss Tangent Free-Space Measurement”, *IEEE Trans. Instrum. Meas.*, vol. 63, no. 7, pp. 1818–1823, 2014.
[135] T.-W. Kang, J.-H. Kim, D.-J. Lee, and N.-W. Kang, “Free-Space Measurement of the Complex Permittivity of Liquid Materials at Millimeter-Wave Region”, In: *2016 Conference on Precision Electromagnetic Measurements (CPEM 2016)*, Ottawa, ON, Canada: IEEE, pp. 1–2, 2016.
[136] E. Hajisaeid, A. F. Dericioglu, and A. Akyurtlu, “All 3-D Printed Free-Space Setup for Microwave Dielectric Characterization of Materials”, *IEEE Trans. Instrum. Meas.*, vol. 67, no. 8, pp. 1877–1886, 2018.
[137] H. Arab *et al.*, “Machine Learning Based Object Classification and Identification Scheme Using an Embedded Millimeter-Wave Radar Sensor”, *Sensors*, vol. 21, no. 13, pp. 4291, 2021.
[138] M. T. Ghasr, D. Simms, and R. Zoughi, “Multimodal Solution for a Waveguide Radiating into Multilayered Structures-Dielectric Property and Thickness Evaluation”, *IEEE Trans. Instrum. Meas.*, vol. 58, no. 5, pp. 1505–1513, 2009.
[139] R. Zoughi, “*Microwave Non-Destructive Testing and Evaluation*”, In: *Non-Destructive Evaluation Series*, Dordrecht: Springer Netherlands, vol. 4, 2000.
[140] A. Foudazi and K. M. Donnell, “Effect of Sample Preparation on Microwave Material Characterization by Loaded Waveguide Technique”, *IEEE Trans. Instrum. Meas.*, vol. 65, no. 7, pp. 1669–1677, 2016.
[141] A. Bogle *et al.*, “Electromagnetic Material Characterization using a Partially-Filled Rectangular Waveguide”, *Journal of Electromagnetic Waves and Applications*, vol. 19, no. 10, pp. 1291–1306, 2005.
[142] M. Kiani, A. Abdolali, and M. Tayarani, “A Novel Waveguide Approach for Electromagnetic Characterization of Inhomogeneous Materials”, *IEEE Trans. Microwave Theory Techn.*, vol. 66, no. 10, pp. 4658–4665, 2018.
[143] D. Munalli, M. T. A. Qaseer, and R. Zoughi, “Modified Waveguide-Based Method for Microwave Characterization of High-Loss Materials”, *IEEE Trans. Instrum. Meas.*, vol. 71, pp. 1–10, 2022.
[144] R. Zoughi, J. R. Gallion, and M. T. Ghasr, “Accurate Microwave Measurement of Coating Thickness on Carbon Composite Substrates”, *IEEE Trans. Instrum. Meas.*, vol. 65, no. 4, pp. 951–953, 2016.
[145] A. Ali, B. Hu, and O. Ramahi, “Intelligent Detection of Cracks in Metallic Surfaces Using a Waveguide Sensor Loaded with Metamaterial Elements”, *Sensors*, vol. 15, no. 5, pp. 11402–11416, 2015.
[146] X. Wang and S. A. Tretyakov, “Fast and Robust Characterization of Lossy Dielectric Slabs Using Rectangular Waveguides”, *IEEE Trans. Microwave Theory Techn.*, vol. 70, no. 4, pp. 2341–2350, 2022.
[147] S. Guorong *et al.*, “Detection of Surface Crack on the Substrate under Thermal Barrier Coatings Using Microwave Non-Destructive Evaluation”, *Journal of Microwave Power and Electromagnetic Energy*, vol. 49, no. 2, pp. 69–75, 2015.

[148] R. Sutthaweekul *et al.*, "Microwave Open-Ended Waveguide for Detection and Characterisation of FBHs in Coated GFRP Pipes", *Composite Structures*, vol. 225, pp. 111080, 2019.
[149] O. V. Tereshchenko, F. J. K. Buesink, and F. B. J. Leferink, "An Overview of the Techniques for Measuring the Dielectric Properties of Materials", In: *2011 XXXth URSI General Assembly and Scientific Symposium*, Istanbul: IEEE, pp. 1–4, 2011.
[150] G. Koutsoukis *et al.*, "Roll-to-Roll In-Line Implementation of Microwave Free-Space Non-Destructive Evaluation of Conductive Composite Thin Layer Materials", *Applied Sciences*, vol. 11, no. 1, pp. 378, 2021.
[151] S. S. Zhekov, O. Franek, and G. F. Pedersen, "Dielectric Properties of Common Building Materials for Ultrawideband Propagation Studies [Measurements Corner]", *IEEE Antennas Propag. Mag.*, vol. 62, no. 1, pp. 72–81, 2020.
[152] S. Razafindratsima, Z. M. Sbartaï, and F. Demontoux, "Permittivity Measurement of Wood Material Over a Wide Range of Moisture Content", *Wood Sci Technol*, vol. 51, no. 6, pp. 1421–1431, 2017.
[153] S. Stavrou, "Review of Constitutive Parameters of Building Materials", In: *Twelfth International Conference on Antennas and Propagation (ICAP 2003)*, Exeter, UK: IEE, pp. 211–215, 2003.
[154] W. Ertel, "Introduction to Artificial Intelligence", In: *Undergraduate Topics in Computer Science*. Cham: Springer International Publishing, 2017.
[155] S. B. Kotsiantis *et al.*, "Supervised Machine Learning: A Review of Classification Techniques", *Emerging artificial intelligence applications in computer engineering*, vol. 160, no. 1, pp. 3-24, 2007.
[156] M. Emms and S. Luz, "Machine Learning for Natural Language Processing", *ESSLLI Course Reader*, 2007.
[157] M. Pak and S. Kim, "A Review of Deep Learning in Image Recognition", In: *2017 4th International Conference on Computer Applications and Information Processing Technology (CAIPT):* IEEE, pp. 1-3, 2017.
[158] I. Alnazer, "Imaging and textural analysis for kidney evaluation", Phd Thesis, Univerity of Poitier, 2021.
[159] M. B. Aayesha *et al.*, "Machine Learning-Based EEG Signals Classification Model for Epileptic Seizure Detection", *Multimed Tools Appl*, vol. 80, no. 12, pp. 17849–17877, 2021.
[160] J. Sacristan, B. L. Oliveira, and S. Pistorius, "Classification of Electromagnetic Signals Obtained from Microwave Scattering Over Healthy and Tumorous Breast Models", In: *2016 IEEE Canadian Conference on Electrical and Computer Engineering (CCECE)*, Vancouver, BC, Canada: IEEE, pp. 1–5, 2016.
[161] B. B. Traore, B. Kamsu-Foguem, and F. Tangara, "Deep convolution Neural Network for Image Recognition", *Ecological Informatics*, vol. 48, pp. 257–268, 2018.
[162] Y. Cao *et al.*, "Two-Stream Convolutional Neural Network for Non-Destructive Subsurface Defect Detection via Similarity Comparison of Lock-in Thermography Signals", *NDT & E International*, vol. 112, pp. 102246, 2020.
[163] M. Meng *et al.*, "Ultrasonic Signal Slassification and Imaging System for Composite Materials via Deep Convolutional Neural Networks", *Neurocomputing*, vol. 257, pp. 128–135, 2017.

[164] N. H. M. M. Shrifan *et al.*, "Microwave Nondestructive Testing for Defect Detection in Composites Based on K-Means Clustering Algorithm", *IEEE Access,* vol. 9, pp. 4820–4828, 2021.
[165] Y. Lu and R. Lu, "Detection of Surface and Subsurface Defects of Apples Using Structured-Illumination Reflectance Imaging with Machine Learning Algorithms" *Transactions of the ASABE,* vol. 61, no. 6, pp. 1831-1842, 2018.
[166] I. Mitiche *et al.*, "Entropy-Based Feature Extraction for Electromagnetic Discharges Classification in High-Voltage Power Generation", *Entropy,* vol. 20, no. 8, pp. 549, 2018.
[167] P. P. Shinde and S. Shah, "A Review of Machine Learning and Deep Learning Applications", In: *2018 Fourth International Conference on Computing Communication Control and Automation (ICCUBEA)*, Pune, India: IEEE, pp. 1–6, 2018.
[168] S. Coulibaly *et al.*, "Deep Learning for Precision Agriculture: A Bibliometric Analysis", *Intelligent Systems with Applications,* vol. 16, pp. 200102, 2022.
[169] A. Moomen, A. Ali, and O. Ramahi, "Reducing Sweeping Frequencies in Microwave NDT Employing Machine Learning Feature Selection", *Sensors,* vol. 16, no. 4, pp. 559, 2016.
[170] V. Shirmohammadli and B. Bahreyni, "Machine Learning for Sensing Applications: A Tutorial", *IEEE Sensors J.*, vol. 22, no. 11, pp. 10183–10195, 2022.
[171] K. Guo *et al.*, "Artificial Intelligence and Machine Learning in Design of Mechanical Materials", *Mater. Horiz.*, vol. 8, no. 4, pp. 1153–1172, 2021.
[172] L. P. Kaelbling, M. L. Littman, and A. W. Moore, "Reinforcement Learning: A Survey", *Journal of artificial intelligence research,* vol. 4, pp. 237-285, 1996.
[173] A. Pradhan, "Support Vector Machine-A Survey", *IJETAE,* vol. 2, no. 8, pp. 82-85, 2012.
[174] W. Tang *et al.*, "Characterisation of Composite Materials for Wind Turbines Using Frequency Modulated Continuous Wave Sensing", *J. Compos. Sci.,* vol. 7, no. 2, pp. 75, 2023.
[175] G. Mountrakis, J. Im, and C. Ogole, "Support Vector Machines in Remote Sensing: A Review", *ISPRS Journal of Photogrammetry and Remote Sensing,* vol. 66, no. 3, pp. 247-259,2011.
[176] B. Richhariya and M. Tanveer, "EEG Signal Classification using Universum Support Vector Machine", *Expert Systems with Applications,* vol. 106, pp. 169–182, 2018.
[177] C. J. C. Burges, "A Tutorial on Support Vector Machines for Pattern Recognition", *Data mining and knowledge discovery,* vol. 2, no. 2, pp. 121-167, 1998.
[178] V. Hlaváč, "Nonlinear Classifiers, Kernel Methods and SVM", *Czech Technical University in Prague,* 2022.
[179] V. Y. Kulkarni and D. P. K. Sinha, "Random Forest Classifiers: A Survey and Future Research Directions", *Int. J. Adv. Comput,* vol. 36, no. 1, pp. 1144-1153, 2013.
[180] I. T. Jolliffe and J. Cadima, "Principal Component Analysis: A Review and Recent Developments", *Phil. Trans. R. Soc. A.*, vol. 374, no. 2065, pp. 20150202, 2016.
[181] K. G. Kim, "Book Review: Deep Learning", *Healthc Inform Res,* vol. 22, no. 4, pp. 351, 2016.
[182] "Introducing Deep Learning with MATLAB", Ebook, doi: https://nl.mathworks.com/campaigns/offers/next/deep-learning-ebook.html.
[183] F. Rosenblatt, "The perceptron: A Probabilistic Model for Information Storage and Organization in the Brain", *Psychological review,* vol. 65, no. 6, pp. 386, 1958.
[184] A. Shrestha and A. Mahmood, "Review of Deep Learning Algorithms and Architectures", *IEEE Access,* vol. 7, pp. 53040-53065, 2019.

[185] S. Kiranyaz *et al.*, "1D Convolutional Neural Networks and Applications: A Survey", *Mechanical Systems and Signal Processing*, vol. 151, pp. 107398, 2021.
[186] O. Avci *et al.*, "Wireless and Real-Time Structural Damage Detection: A Novel Decentralized Method for Wireless Sensor Networks", *Journal of Sound and Vibration*, vol. 424, pp. 158-172, 2018.
[187] C. Li *et al.*, "Intelligent Recognition of Composite Material Damage Based on Deep Learning and Infrared Testing", *Opt. Express*, vol. 29, no. 20, pp. 31739, 2021.
[188] S. Kiranyaz *et al.*, "Convolutional Neural Networks for patient-specific ECG classification", In: *2015 37th Annual International Conference of the IEEE Engineering in Medicine and Biology Society (EMBC)*, Milan: IEEE, pp. 2608–2611,2015.
[189] S. Kiranyaz *et al.*, "Real-Time Phonocardiogram Anomaly Detection by Adaptive 1D Convolutional Neural Networks", *Neurocomputing*, vol. 411, pp. 291-301, 2020.
[190] Q. Shen *et al.*, "Multiscale Deep Neural Network for Obstructive Sleep Apnea Detection Using RR Interval from Single-Lead ECG Signal", *IEEE Trans. Instrum. Meas.*, vol. 70, pp. 1-13, 2021.
[191] S. Thompson *et al.*, "Detection of Obstructive Sleep Apnoea Using Features Extracted from Segmented Time-Series ECG Signals Using a One Dimensional Convolutional Neural Network", In: *2020 International Joint Conference on Neural Networks (IJCNN)*, Glasgow, United Kingdom: IEEE, pp. 1–8, 2020.
[192] O. Avci *et al.*, "Structural Damage Detection in Real Time: Implementation of 1D Convolutional Neural Networks for SHM Applications", In: *Structural Health Monitoring & Damage Detection, Volume 7: Proceedings of the 35th IMAC, A Conference and Exposition on Structural Dynamics 2017*, Springer International Publishing, pp. 49-54, 2017.
[193] O. Abdeljaber *et al.*, "1-D CNNs for Structural Damage Detection: Verification on a Structural Health Monitoring Benchmark Data", *Neurocomputing*, vol. 275, pp. 1308-1317, 2018.
[194] C. Jiang *et al.*, "A Two-Stage Structural Damage Detection Method Based on 1D-CNN and SVM", *Applied Sciences*, vol. 12, no. 20, pp. 10394, 2022.
[195] S. Kiranyaz, T. Ince, and M. Gabbouj, "Real-Time Patient-Specific ECG Classification by 1-D Convolutional Neural Networks", *IEEE Trans. Biomed. Eng.*, vol. 63, no. 3, pp. 664-675, 2016.
[196] L. Eren, "Bearing Fault Detection by One-Dimensional Convolutional Neural Networks", *Mathematical Problems in Engineering*, vol. 2017, pp. 1-9, 2017.
[197] S. Kiranyaz *et al.*, "Real-Time Fault Detection and Identification for MMC Using 1-D Convolutional Neural Networks", *IEEE Trans. Ind. Electron.*, vol. 66, no. 11, pp. 8760-8771, 2019.
[198] A. R. Kim *et al.*, "The Design of the 1D CNN–GRU Network Based on the RCS for Classification of Multiclass Missiles", *Remote Sensing*, vol. 15, no. 3, pp. 577, 2023.
[199] A. Vabalas *et al.*, "Machine Learning Algorithm Validation with a Limited Sample Size", *PLoS ONE*, vol. 14, no. 11, pp. e0224365, 2019.
[200] M. Kuhn and K. Johnson, "Applied Predictive Modeling", *NY: Springer*, vol. 26, pp. 13, 2013.
[201] F. Sohil, M. U. Sohali, and J. Shabbir, "An Introduction to Statistical Learning", *Statistical Theory and Related Fields*, vol. 6, no. 1, pp. 87-87, 2022.
[202] N. Munir *et al.*, "Investigation of Deep Neural Network with Drop out for Ultrasonic Flaw Classification in Weldments", *J Mech Sci Technol*, vol. 32, no. 7, pp. 3073-3080, 2018.

[203] M. S. M. Naqiuddin *et al.*, "Ultrasonic Signal Processing Techniques for Pipeline: A Review", *MATEC Web Conf.*, vol. 255, pp. 06006, 2019.
[204] R. D. Tipones and J. C. Dela Cruz, "Design and Development of a Material Impact Tester using Neural Network for Concrete Ratio Classification", In: *2017 IEEE 13th International Colloquium on Signal Processing & its Applications (CSPA)*, Penang, Malaysia: IEEE, pp. 106-111, 2017.
[205] W. Tang *et al.* "Machine Learning Analysis of Non-Destructive Evaluation Data from Radar Inspection of Wind Turbine Blades", In: *2021 IEEE International Conference on Sensing, Diagnostics, Prognostics, and Control (SDPC)*. IEEE, pp. 122-128, 2021.
[206] S. Julrat and S. Trabelsi, "Determination of Foreign-Material Content in Uncleaned Peanuts by Microwave Measurements and Machine Learning Techniques", *Journal of Microwave Power and Electromagnetic Energy*, vol. 56, no. 1, pp. 3-17, 2022.
[207] T. Mosavirik *et al.*, "Accuracy-Improved and Low-Cost Material Characterization Using Power Measurement and Artificial Neural Network", *IEEE Trans. Instrum. Meas.*, vol. 70, pp. 1–9, 2021.
[208] R. TEMPKE *et al.,* "Machine Learning Approach to Transform Scattering Parameters to Complex Permittivities", *Journal of Microwave Power and Electromagnetic Energy*, vol. 55, no. 4, pp. 287-302, 2021.
[209] A. Ali, B. Hu, and O. Ramahi, "Intelligent Detection of Cracks in Metallic Surfaces Using a Waveguide Sensor Loaded with Metamaterial Element", *Sensors*, vol. 15, no. 5, pp. 11402-11416, 2015.
[210] Y. Xie *et al.*, "A Microwave Time Domain Reflectometry Technique Combining the Wavelet Decomposition Analysis and Artificial Neural Network for Detection of Defects in Dielectric Structures", *IEEE Trans. Instrum. Meas.*, vol. 71, pp. 1-11, 2022.
[211] S. ABOUZAID *et al.*, "Deep Learning-Based Material Characterization Using FMCW Radar with Open-Set Recognition Technique", *IEEE Transactions on Microwave Theory and Techniques*, 2023.
[212] N. H. M. M. Shrifan, M. F. Akbar, and N. A. M. Isa, "Prospect of Using Artificial Intelligence for Microwave Nondestructive Testing Technique: A Review", *IEEE Access*, vol. 7, pp. 110628–110650, 2019.
[213] M. A. Aldhaeebi *et al.*, "Electrically Small Magnetic Probe with PCA for Near-Field Microwave Breast Tumors Detection", *PIER M*, vol. 84, pp. 177–186, 2019.
[214] B. Richhariya and M. Tanveer, "EEG Signal Classification using Universum Support Vector Machine", *Expert Systems with Applications*, vol. 106, pp. 169–182, 2018.
[215] A. Abid, M. T. Khan, and J. Iqbal, "A Review on Fault Detection and Diagnosis Techniques: Basics and Beyond", *Artif Intell Rev*, vol. 54, no. 5, pp. 3639-3664, 2021.
[216] I. T. Jolliffe and J. Cadima, "Principal Component Analysis: A Review and Recent Developments", *Phil. Trans. R. Soc. A.*, vol. 374, no. 2065, pp. 20150202, 2016.
[217] S. Karamizadeh *et al.,* "An Overview of Principal Component Analysis", *JSIP*, vol. 04, no. 03, pp. 173-175, 2013.
[218] S. Tangirala, "Evaluating the Impact of GINI Index and Information Gain on Classification using Decision Tree Classifier Algorithm", *IJACSA*, vol. 11, no. 2, 2020.
[219] K. Haddadi *et al.*, "A 60 GHz Six-Port Distance Measurement System with Sub-Millimeter Accuracy", *IEEE Microw. Wireless Compon. Lett.*, vol. 19, no. 10, pp. 644-646, 2009.
[220] M. Voelkel *et al.*, "A High Precision Reconfigureable Bistatic Interferometric Radar with Integrated Six-port Receiver at 60 GHz", In: *2019 12th German Microwave Conference (GeMiC)*, Stuttgart, Germany: IEEE, pp. 48-50, 2019.

[221] A. Koelpin *et al.*, "The Six-Port in Modern Society", *IEEE Microwave*, vol. 11, no. 7, pp. 35–43, 2010.
[222] K. Staszek, S. Gruszczynski, and K. Wincza, "Theoretical Limits and Accuracy Improvement of Reflection-Coefficient Measurements in Six-Port Reflectometers", *IEEE Trans. Microwave Theory Techn.*, vol. 61, no. 8, pp. 2966-2974, 2013.
[223] V. Bilik, "Six-Port Measurment Technique: Principles, Impact, Applications", In: *Invited paper at the International Conference RADIOELEKTRONIKA*, 2002.
[224] S. Lallemand, K. Haddadi, and C. Loyez, "A Review of the Six-Port Technique for Metrology Applications", In: *2018 22nd International Microwave and Radar Conference (MIKON)*, Poznan: IEEE, pp. 77–79, 2018.
[225] G. F. Engen and C. A. Hoer, "The Application of Thru-Short-Delay to the Calibration of the Dual Six-Port", In: *MTT-S International Microwave Symposium Digest*, N/A: MTT005, pp. 184–185, 1978.
[226] K. Haddadi and T. Lasri, "60-GHz Near-Field Six-Port Microscope Using a Scanning Slit Probe for Subsurface Sensing", *IEEE Sensors J.*, vol. 12, no. 8, pp. 2575-2576, 2012.
[227] K. Haddadi, D. Glay, and T. Lasri, "A 60 Ghz Scanning Near-Field Microscope with High Spatial Resolution Sub-Surface Imaging", *IEEE Microw. Wireless Compon. Lett.*, vol. 21, no. 11, pp. 625-627, 2011.
[228] S. O. Tatu and K. Wu, "Six-port Technology and Applications", In: *2013 11th International Conference on Telecommunications in Modern Satellite, Cable and Broadcasting Services (TELSIKS)*, IEEE, pp. 239-248, 2013.
[229] S. Linz *et al.*, "A Compact, Versatile Six-Port Radar Module for Industrial and Medical Applications", *Journal of Electrical and Computer Engineering*, vol. 2013, pp. 1-10, 2013.
[230] S. Heining *et al.*, "An Ultra Broadband Multi-Tone Six-Port Radar for Distance Measurements in K-Band Waveguides", In: *2020 IEEE Radio and Wireless Symposium (RWS)*, San Antonio, TX, USA: IEEE, pp. 279-282, 2020.
[231] G. Vinci and A. Koelpin, "Progress of Six-Port Technology for Industrial Radar Applications", In: *2016 IEEE Topical Conference on Wireless Sensors and Sensor Networks (WiSNet)*, Austin, TX, USA: IEEE, pp. 48–51, 2016.
[232] S. Linz *et al.*, "I/Q Imbalance Compensation for Six-Port Interferometers in Radar Applications", In: *2014 44th European Microwave Conference*, Rome: IEEE, pp. 746-749, 2014.
[233] S. Lindner *et al.*, "Mixer Assisted Interferometric Six-Port System for Accurate Distance Measurements", In: *2017 European Radar Conference (EURAD)*, Nuremberg: IEEE, pp. 291–294, 2017.
[234] A. Koelpin *et al.*, "Six-Port Technology for Precise Geometrical Measurement Applications - An Overview", In: *2013 European Microwave Conference*. IEEE, pp. 1587-1590, 2013.
[235] A. Koelpin *et al.*, "Six-Port Based Interferometry for Precise Radar and Sensing Applications", *Sensors*, vol. 16, no. 10, pp. 1556, 2016.
[236] S. Julrat, and S. Trabelsi, "Free-Space Transmission Dielectric Properties Measurement Based on Six-port Technology", *IEEE Transactions on Instrumentation and Measurement*, vol. 70, pp. 1-7, 2021.
[237] S. Benchikh *et al.*, "Millimeter Wave Six-Port Radar Sensor for Precise Displacement Measurements and Gesture Sensing Applications", In: *2019 IEEE Topical Conference on Wireless Sensors and Sensor Networks (WiSNet)*, Orlando, FL, USA: IEEE, pp. 1-3, 2019.

[238] N. Alsaleh *et al.*, “Nano-Positioning Test platform for Free-Space Six-Port Interferometric Distance Measurements”, In: *2021 IEEE Conference on Antenna Measurements & Applications (CAMA)*, Antibes Juan-les-Pins, France: IEEE, pp. 562–564, 2021.
[239] N. Alsaleh *et al.*, “WR15 Six-Port Interferometric Set-up for Millimeter-wave Characterization for Harsh Environments”, In: *2022 Photonics & Electromagnetics Research Symposium (PIERS)*, Hangzhou, China: IEEE, pp. 414-419; 2022.
[240] K. Haddadi *et al.*, “Six-Port Reflectometer in WR15 Metallic Waveguide for Free-Space Sensing Applications”, In: *2018 IEEE Topical Conference on Wireless Sensors and Sensor Networks (WiSNet)*, Anaheim, CA: IEEE, pp. 80–83, 2018.
[241] S. Linz, “Impairment Analysis and Their Calibration Techniques for Six-Port Based Displacement Sensors”, Phd Thesis, Friedrich-Alexander-Universität Erlangen-Nürnberg (FAU), 2020.
[242] P. I. Somlo and J. D. Hunter, “A Six-Port Reflectometer and its Complete Characterization by Convenient Calibration Procedures”, *IEEE Trans. Microwave Theory Techn.*, vol. 30, no. 2, pp. 186–192,1982.
[243] F. Wiedmann, « Développements pour des Applications Grand Public du Réflectomètre Six-Portes : Algorithme de Calibrage Robuste, Réflectomètre à très Large Bande et Réflectomètre Intégré MMIC », Thèse de doctorat, Télécom ParisTech, 1997.

# APPENDIX A. Markov Chain approach for the ARL calculation

The Markov chain approach is an efficient technique to estimate the ARL. According to this approach, the control limit interval is divided into N+1 sub-intervals of width $\omega$. The control chart is considered to be in a transient state $(i)$ at the iteration $k$ if$I_i - \frac{\omega}{2} < S_k < I_i + \frac{\omega}{2}$, where Ii represents the midpoint of the$i^{th}$ interval. The control statistic is in the absorbing state if $S_k$falls outside the control limits.

The process is assumed to be in control when $S_k$ is in a transient state. It is however assumed to be out of control when $S_k$ is in the absorption state.

The term$p_{ij}$ refers to the transition probability defined as the probability that the transition from state $i$ to state $j$ occurs.

$$p_{ij} = p\{S_{k+1} \in I_j \vee S_k \in I_i\}, i, j = 0,1, \dots, N-1 \quad \text{(A1)}$$

The initial probability vector can be represented by:

$$p_0^T = (p_0, p_1, \dots, p_{N-1} \vee 0) \quad \text{(A2)}$$

Where $p_j$ represents the probability that $S_k$ starts I n state$(j)$.

The ARL is then determined by its initial probability vector and transition probability matrix. Generally, the initial probability vector will contain a single element equal to 1, representing the initial state. The ARL is therefore given by the following equation:

$$ARL = P_0^T (I - R).1 \quad \text{(A3)}$$

Where R is the matrix contains the transition probabilities. I is the identity matrix, and 1 is a column vector of ones.

The transition probabilities are then as follows:

For the CUSUM control chart:

$$\begin{cases} p_{i0} = P\{S_k \in I_0 \vee S_{k-1} = i\omega\} = P\left\{X_k \le K - i\omega + \frac{\omega}{2}\right\}, \\ p_{ij} = P\{S_k \in I_j \vee S_{k-1} = i\omega\} = P\left\{(j-i)\omega - \frac{\omega}{2} < X_k - K \le (j-i)\omega + \frac{\omega}{2}\right\}, \\ 1 \le j \le t-1. \end{cases} \quad \text{(A4)}$$

It should be noted that we need to estimate the overall ARL of a two-sided CUSUM chart. Thus, it can be derived from those of two one-sided schemes, using this formula:

$$\frac{1}{ARL} = \frac{1}{ARL^{\frac{++1}{ARL^{-}}}} \quad \text{(A5)}$$

For the EWMA control chart:

$$p_{ij} = P\{S_k \in I_j \vee S_{k-1} = i\omega\} = P\left\{j\omega - \frac{\omega}{2} < (1-\lambda)i\omega + \lambda X_k \leq j\omega + \frac{\omega}{2}\right\} \quad \text{(A6)}$$

The ARL is then determined based on the initial probability vector and the calculated transition probability matrix according to the equation (A6).

# APPENDIX B. OSLN50A-8 calibration kit specifications

This calibration kit has been designed to provide superior measurement results when used with precision instruments. It is designed for use in both field and lab environments. It is a high precision component and should be handled with proper care. Excessive shock, torque, or power should be avoided to prevent permanent damage.

Specifications for units within recommended calibration cycle are guaranteed under the following conditions:

1. Unit is operated within specified temperature range.
2. Unit has not been subjected to damage from mishandling.

Length, capacitance, and inductance are nominal values. Open and Short Phase and DC Resistance specifications are typical. Phase is measured as a deviation from the model defined by offset length and inductance or capacitance.

| | |
|---|---|
| **Operating Temperature Range** | –10 °C to +55 °C (MIL-PRF-28800F, Class 2) |
| **Storage Temperature Range** | –51 °C to +71 °C (MIL-PRF-28800F, Class 2) |
| **Recommended Calibration Interval** | 1 year |

Table B.1 OSLN50A-8 Calibration Kit Specifications – Temperature.

| Open | Spec |
|---|---|
| Length | 17.83 mm |
| C0 (1E-15) F | 4.000 |
| C1 (1E-27) F/Hz | 200.000 |
| C2 (1E-36) F/Hz$^2$ | 0.000 |
| C3 (1E-45) F/Hz$^3$ | 1.100 |
| Phase (DC to 6 GHz) | ≤ ± 2.0° |
| Phase (6 to 8 GHz) | ≤ ± 3.0° |

Table B.2 OSLN50A-8 Calibration Kit Specifications – Open.

| Short | Spec |
|---|---|
| Length | 17.83 mm |
| L0 (1E-12) H | 0.000 |
| L1 (1E-24) H/Hz | 0.000 |
| L2 (1E-33) $H/Hz^2$ | 0.000 |
| L3 (1E-42) $H/Hz^3$ | 0.000 |
| Phase (DC to 6 GHz) | ≤ ± 1.5° |
| Phase (6 to 8 GHz) | ≤ ± 2.5° |

Table B.3 OSLN50A-8 Calibration Kit Specifications – Short.

| Load | Spec |
|---|---|
| DC Resistance | 50 Ω ± 0.25 Ω |
| Return Loss (DC to 6 GHz) | ≥ 42 dB |
| Return Loss (6 to 8 GHz) | ≥ 37 dB |
| Max Power | 1.0 W |

Table B.4 OSLN50A-8 Calibration Kit Specifications – Load.